

ABSTRACT

Title of dissertation: Phase Transitions of
High-Temperature Superconductors

Su Li
Doctor of Philosophy, 2007

Dissertation directed by: Professor Christopher J. Lobb
Department of Physics
Center for Superconductivity Research

In this thesis phase transitions of the high temperature superconductor $\text{YBa}_2\text{Cu}_3\text{O}_{7-\delta}$ (YBCO) have been investigated in both zero and non-zero magnetic field. Current-Voltage characteristics of thin films and single crystals have been studied to determine the transition temperature and critical exponents. We optimized our film samples to ensure that they are of single phase, c -axis oriented and homogeneous. High-quality crystal samples were provided by Dr. Kouji Segawa and Dr. Yoichi Ando.

In the zero-field transition, finite-size effects, which can obscure the phase transition by introducing ohmic tails below the transition temperature, are observed in the current-voltage curves of even the thickest film (2400 Å) at low currents. The data at high currents are not affected by finite-size effects so that we can use derivative plots to determine T_c and the dynamic critical exponent z . The current-voltage curves of crystals' data, however, are not affected by finite-size effects even in the lowest current measured as expected. z determined from YBCO crystals are

consistent with the one determined from YBCO films: $z = 1.5 \pm 0.2$. This is a strong evidence that the dynamic universality class of high-temperature superconductors belongs to model-E dynamics in zero field. The static critical exponent ν determined from the melting line $(T_c - T_{g(m)}) \sim H^{1/2\nu_0}$ is 0.68 ± 0.1 for crystal and 0.62 ± 0.1 for thin films.

The phase transitions in the mixed state (non-zero field) are more complicated. In the phase transition of YBCO thin films in field, finite-size effects are again observed. The presence of magnetic field leads to anisotropic vortex loops so that finite-size effects are enhanced. We observe a magnetic field H dependence of the crossover current density J_{min} as well as the exponent z . At $H > 1$ T, J_{min} and z stay relatively constant. $z \simeq 2$ at high field implies a crossover from model-E dynamics to model-A dynamics. Finally, we will discuss $E - J$ characteristics of the first-order melting transition of untwinned YBCO single crystals.

Phase Transitions of High Temperature Superconductors

by

Su Li

Dissertation submitted to the Faculty of the Graduate School of the
University of Maryland, College Park in partial fulfillment
of the requirements for the degree of
Doctor of Philosophy
2007

Advisory Committee:

Professor Christopher J. Lobb, Chair/Advisor

Professor Steven M. Anlage, Co-Advisor

Professor Richard Greene

Professor James Robert Anderson

Professor Lourdes G. Salamanca-Riba

© Copyright by
Su Li
2007

Dedication

To my parents.

ACKNOWLEDGMENTS

This dissertation would not have been possible without the support of many people.

Firstly, I would like to express my deep and sincere gratitude to my advisor, Professor Christopher J. Lobb. Professor Lobb led me into the field of superconductivity in 2003. Ever since then, I am impressed by his wisdom and wide knowledge. I am thankful for his considerable patience and confidence on me, and his guidance and encouragement during the last four years of research.

I am deeply grateful to my co-advisor, Professor Steven M. Anlage. He was always there when I had questions and helped me going through many difficulties.

Dr. Matthew C. Sullivan and Dr. Douglas Strachan taught me many things about my project including the film making, transport measurement and data analysis. I owe a lot to their expertise and valuable experiences since my work is based on their previous research.

It is a pleasure to work with my lab mate, Hua Xu. He has done an excellent work on the other side of the project: microwave measurement. His discussions with me had lead to many interesting findings. I would also like to thank Monica Lilly for her hard work and good suggestions when she was in the critical group.

Professor Richard L. Greene provided many helps when I was attempting to measure heat capacity. He is a generous person for letting me to use the blue magnet

exclusively for two years in his lab.

I am grateful to Dr. Kouji Segawa and Dr. Yoichi Ando from Japan for their valuable YBCO single crystals. Without their samples, this work could not be as good as now it is. I also would like to thank Professor Alan Dorsey for his discussion with us and Professor Jack Lidmar for his email correspondence with me about experimental results.

I want to thank other people in the center including Dr. Pengcheng Li, Dr. Weiqiang Yu, Hanhee Paik, David Tobias, Dr. Sudeep Dutta, Dr. Dragos Mircea, Shixiong Zhang, Dr. Joshua Higgins, Dr. R. D. Vispute, Dr. Rupert Lewis, Dr. John Matthews, Dr. Costel R. Rotundu and Paul Bach for their help and useful suggestions. I also would like to thank Luyan Sun in LPS for patterning some of my samples and Hui Wang for some knowledge on the observation of vortices using STM.

I am thankful to the wonderful group of people who have provided technical and administrative support: Douglas Bensen, Brian Straughn, Belta Pollard, Grace Sewlall, Brian Barnaby, Cleopatra White, Jane Hensing, Linda Ohara and Pauline Rirksopa.

On the personal side, I am deeply grateful to my wife Janzhu (Jiarun) Li her support. I appreciate everything she has been doing. I also would like to thank my daughter Yifan A. Li for bringing joy to my life. Their love have give me strengthen to accomplish the graduate study after going through many years of work.

Table of Contents

List of Tables	vii
List of Figures	viii
List of Abbreviations	xi
1 Introduction	1
1.1 Phase Transitions	1
1.1.1 First-order and Continuous Phase Transitions	3
1.2 Superconductivity	3
1.2.1 Phase Diagrams of Type-I and Type-II Superconductor	6
1.2.2 $\text{YBa}_2\text{Cu}_3\text{O}_{7-\delta}$	9
1.3 Critical Phenomena and Critical Exponents	12
1.3.1 Mean-Field Theory	14
1.3.2 Thermal Fluctuations and the Critical Regime	17
1.3.3 Universality and the 3D-XY Theory	18
2 Experiment	20
2.1 Overview	20
2.2 YBCO Films	21
2.3 YBCO Crystals	34
2.4 DC Measurements in Zero Magnetic Field	34
2.5 DC Measurements in Magnetic Field	44
3 The Superconducting Phase Transition of YBCO in Zero Field	46
3.1 The Zero-Field Transition	47
3.1.1 Scaling Theory	48
3.1.2 Vortex-Loop Unbinding	50
3.1.3 Finite-Size Effects	53
3.2 Data and Analysis	56
3.2.1 Crystal Data	61
3.2.2 Film Data	67
3.2.3 Discussion	72
4 The Superconducting Phase Transition of YBCO in Magnetic Field	89
4.1 Vortex-Glass Phase Transition	89
4.2 Experimental Results of YBCO Films	94
4.2.1 Conventional Method	94
4.2.2 Derivative Plot	99
4.3 Discussion	102
4.3.1 Finite-size Effects in Fields	102
4.3.2 Dynamical Critical Exponent z in Field	109
4.4 Experimental Results of YBCO Crystals	111

5	Summary and future works	122
5.1	Summary	122
5.2	Future Work	124
A	Currents and Lengths in Superconductors (Lobb's note)	126
A.1	Initial considerations	126
A.2	More realistic model for $\varepsilon(r)$	130
B	Literature Review	134
	Bibliography	137

List of Tables

2.1	Lattice mismatches of several substrates used for deposition of YBCO.	24
A.1	Translation table for the physical quantities between Circuits and Vortices.	131
B.1	Zero-field critical exponents from theoretical predictions, numerical simulations and experimental results.	135
B.2	Vortex-glass critical exponents from theoretical predictions, numerical simulations and experimental results.	136

List of Figures

1.1	Phase Diagram for a solid-liquid-gas system.	2
1.2	Schematics of free energy and entropy as functions of temperature for first-order and second-order phase transitions.	4
1.3	Phase diagram of a type I superconductor.	6
1.4	Phase diagram of a type II superconductor.	8
1.5	Schematic phase diagram of a 3-D type II superconductor.	10
1.6	Schematic of unit cell of YBCO.	11
1.7	Examples of the various types of behavior near $t = 0$	13
1.8	Ginzburg-Landau free-energy functions for $T > T_c$ ($\alpha > 0$) and for $T < T_c$ ($\alpha < 0$)	15
2.1	Schematic of pulsed laser deposition setup.	22
2.2	Resistivities of YBCO thin films grown on STO and NGO substrates vs. temperature.	25
2.3	Schematic diagram of ac susceptibility measurement.	27
2.4	AC susceptibility of a YBCO film (sample 126).	29
2.5	Schematic of a X-ray setup.	30
2.6	Typical x-ray diffraction pattern	32
2.7	Photograph of a YBCO film's bridge pattern.	33
2.8	Photograph of a YBCO crystal sample with contacts.	35
2.9	Resistivity vs. temperature of an untwinned YBCO optimally-doped single crystal.	36
2.10	Photograph of the setup of the zero-field measurement.	38
2.11	Photograph of the probe	39
2.12	$I - V$ curves for sample su058.	41
2.13	Schematic of low frequency measurement setup.	43

2.14	Schematic of the “Blue” magnet.	45
3.1	Schematic of the potential barrier for vortex-loop.	52
3.2	Schematic of the critical size of vortex loops with respect to the film thickness.	57
3.3	Schematic of expected $E - J$ isotherms.	58
3.4	Schematic of the expected $d \log(E)/d \log(J)$ vs. J plot.	60
3.5	$E - J$ isotherms for a YBCO single untwinned crystal in zero field. . .	63
3.6	Derivative plot of the $E - J$ isotherms in Fig. 3.5	64
3.7	A fitting of the ohmic tails R_L above T_c	65
3.8	$T_c - T_m$ vs. $\mu_0 H$ of an untwinned YBCO single crystal.	66
3.9	$E - J$ isotherms for a 1500 Å YBCO film in zero magnetic field.	68
3.10	Derivative plot for a 1500 Å YBCO film in zero magnetic field.	69
3.11	Derivative plot at high-current regime.	71
3.12	$T_c - T_g$ vs. H in double-log scale of a YBCO thin film	73
3.13	Predicted conductivity with Gaussian fluctuations.	74
3.14	Schematic of the two-channel model.	75
3.15	Extrapolating the normal background from ρ vs. T of YBCO crystal.	76
3.16	E vs. J (solid curves) and E vs. ΔJ (dotted curves) of a YBCO film (sample su113) on the same plot. The separation of each isotherm is 0.50 K	78
3.17	E vs. J and E vs. ΔJ of of the isotherm 91.775 K on the same plot.	79
3.18	E vs. J (solid curves) and E vs. ΔJ (dotted curves) of YBCO crystal (sample C1).	81
3.19	Comparison of the derivative plots of two different bridges in the same YBCO film.	85
3.20	Comparison of the E vs. J between the data from a YBCO crystal with and without exchange gas.	87

4.1	Resistivity vs. Temperature of a YBCO film (su113) at various magnetic fields.	95
4.2	$E - J$ curves for sample su113 at 5 T magnetic field.	97
4.3	Conventional data collapse for sample su113 at 5 T field.	98
4.4	$\partial \log(E)/\partial \log(J)$ vs. J for su113 at 5 T field.	100
4.5	A schematic of a fluctuation of a single vortex line.	102
4.6	J_{min} vs. H of sample su113.	106
4.7	J_{min} vs. thickness for three different films.	108
4.8	z vs. H of sample su113, su114 and su120.	110
4.9	Resistivity as a function of temperature of an untwinned YBCO single crystal at magnetic field.	113
4.10	Hysteresis of the resistivity of a untwinned YBCO single crystal at 5 T.	114
4.11	ρ_{kink} as a function of magnetic field.	116
4.12	$E - J$ curves of a untwinned YBCO single crystal at $H = 4$ T.	118
4.13	Derivative plot of the same curves from Fig. 4.12.	119
4.14	Crossover current density J_{min} as a function of sample thickness d in zero magnetic field and high magnetic field.	121

List of Abbreviations

CSR	Center for Superconductivity Research
OFHC	Oxygen free high conductivity copper
XRD	X-ray diffraction
PLD	Pulsed laser deposition
YBCO	$\text{YBa}_2\text{Cu}_3\text{O}_{7-\delta}$
PCCO	$\text{Pr}_{2-x}\text{Ce}_x\text{CuO}_4$
BSCCO	$\text{Bi}_2\text{Sr}_2\text{CaCu}_2\text{O}_{8+\delta}$

Chapter 1

Introduction

High temperature superconductivity was discovered by Johannes Georg Bednorz and Karl Alexander Müller in 1986 [1], for which they won the Nobel Prize in physics the following year. Compared to conventional superconductors [2], which were first discovered at Kammerlingh-Onnes' laboratory in 1911, the high temperature superconductors have higher transition temperatures (T_c), longer penetration depths (λ) and shorter coherence lengths (ξ). The phase transition of bulk conventional superconductor is well explained by the Ginzburg-Landau theory. However, the phase transition of high-temperature superconductor is still not understood in both the zero magnetic field and non-zero magnetic field.

1.1 Phase Transitions

A phase transition [3] is the transformation of a thermodynamic system from one state of matter to another. At the transition point, two phases or more can coexist in equilibrium with each other.

One of the most common examples of a phase transition occurs in fluid systems, as shown in Fig. 1.1 [4]. The solid and gas phases are in equilibrium along the sublimation curve, the solid and liquid phases are in equilibrium along the fusion curve and the liquid and gas phases are in equilibrium along the vapor pressure curve.

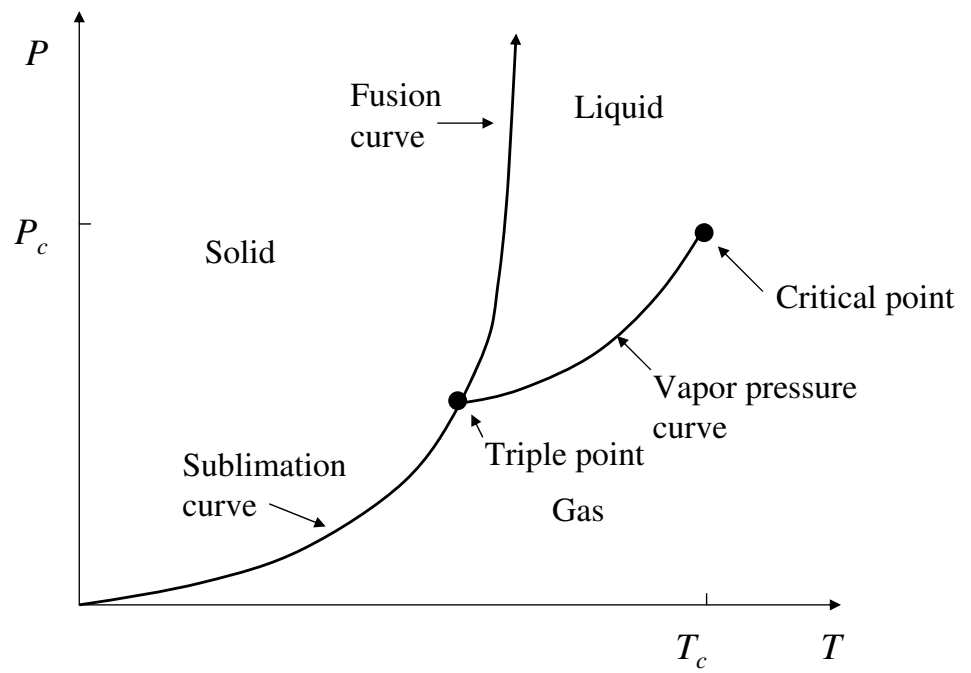


Figure 1.1: Phase diagram for a solid-liquid-gas system.

1.1.1 First-order and Continuous Phase Transitions

When a phase transition occurs, the Gibbs free energy must change continuously. However, the derivative of the free energy may not be continuous at the transition point. Phase transitions can be labelled by the lowest derivative of the free energy that is discontinuous at the transition.

Phase transition which are accompanied by a discontinuity in the first derivative of the free energy with respect to a thermodynamic variable (such as temperature or volume) are called first-order phase transitions as shown in Fig. 1.2(a). Phase transitions that have a continuous first derivative of the free energy (but are discontinuous in the higher-order derivatives) are called continuous phase transitions as shown in Fig. 1.2(b).

Typical first-order phase transitions include the vapor-liquid, vapor-solid, and liquid-solid transitions (except at the critical point), the superconducting to normal transitions of type I superconductors in magnetic field and the superfluid transitions in liquid ^3He . Typical continuous phase transitions include the superconducting to normal transitions in the absence of magnetic field and the superfluid transition in liquid ^4He .

1.2 Superconductivity

Superconductivity is characterized by zero linear electrical resistance and the exclusion of the interior magnetic field (the Meissner effect).

Since its discovery in 1911, much work has been done to understand supercon-

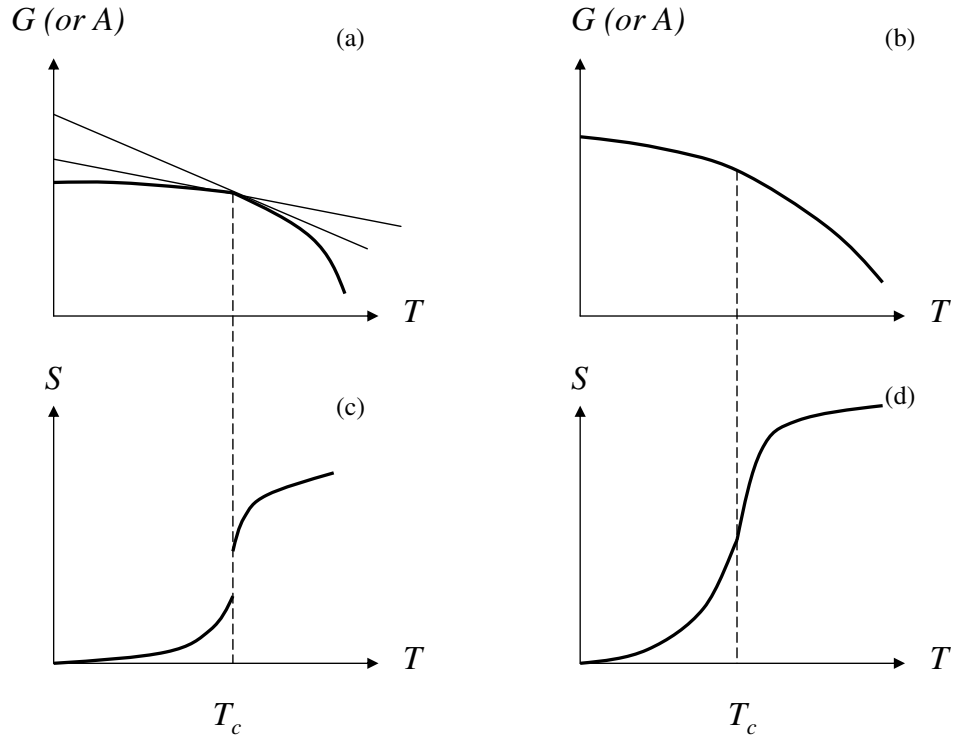


Figure 1.2: (a) Temperature dependence of the Gibbs free energy G or Helmholtz free energy A . The system undergoes a first order phase transition at $T = T_c$ as illustrated by the discontinuity of the slope at T_c . (b) Same as (a) except that the phase transition is continuous. (c)-(d) show the entropy obtained from the temperature derivative of G or A .

ductivity. In 1935, F. and H. London [5] proposed two equations which relate the current to the microscopic electric and magnetic fields (here we use the notation in Tinkham [6])

$$\mathbf{E} = \frac{\partial}{\partial t}(\Lambda \mathbf{J}_s) \quad (1.1)$$

$$\mathbf{H} = -c\nabla \times (\Lambda \mathbf{J}_s) \quad (1.2)$$

where \mathbf{E} and \mathbf{H} are the electric and magnetic fields, \mathbf{J}_s is the supercurrent density, n_s is the number density of superconducting electrons and

$$\Lambda = \frac{4\pi\lambda^2}{c^2} = \frac{m}{n_s e^2} \quad (1.3)$$

is a phenomenological parameter. The purpose of these two equations is to describe the zero resistance and the exclusion of the magnetic field.

In 1957, John Bardeen, Leon Cooper, and Robert Schrieffer [7] proposed the BCS theory. They received the Nobel Prize for Physics in 1972 as a result. In BCS theory, it was shown that even a weak attractive interaction (interaction between the electrons and crystal lattice) between electrons can cause an instability of the ordinary Fermi-sea ground state. Cooper pairs can then be formed by the electrons with opposite spin. The pairing opens a gap in the continuous spectrum of allowed energy states of the electrons and the gap leads to superconductivity.

Seven years before the BCS theory, Ginzburg and Landau [8] proposed a complex pseudowave-function ψ as an order parameter based on Landau's previously established theory of second-order phase transitions. The superconducting "Cooper pairs" can then be described by the wave function, $\psi = |\psi|e^{i\varphi}$, which is also referred

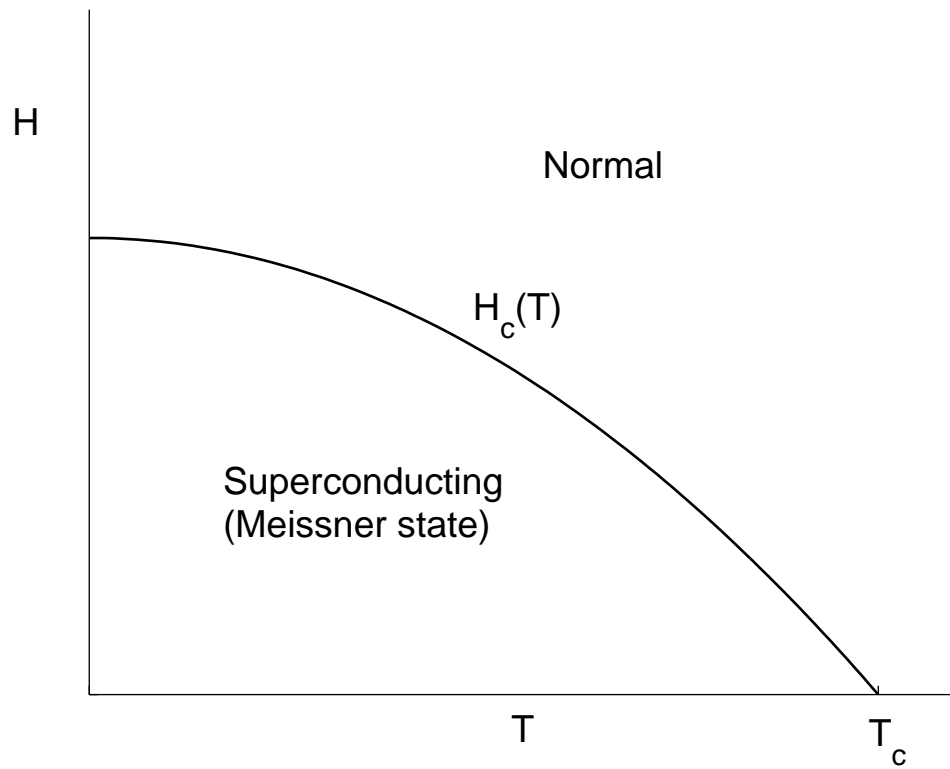


Figure 1.3: Phase diagram of a type I superconductor.

as the “order parameter”. We will discuss the Ginzburg-Landau theory in more detail in later sections.

1.2.1 Phase Diagrams of Type-I and Type-II Superconductor

Superconductors can be classified into two categories depending on the GL parameter

$$\kappa = \frac{\lambda}{\xi} \tag{1.4}$$

For type-I superconductors (mercury, lead, tin, etc), $\kappa < 1/\sqrt{2}$. The type I superconductors have a simple phase diagram which is shown in Fig. 1.3. The coexistence curve, $H_c(T)$, which separates the normal and superconducting phases, is defined by $H_c(T)$ which varies approximately as $(1 - T/T_c)^{1/2}$ near T_c . Below the coexistence curve, the material is in the superconducting state or Meissner state. The linear resistance is strictly zero and the material is a perfect diamagnet with a penetration depth λ (usually on the order of 500 Å). At T_c , the phase transition from the normal state to superconducting state is second-order. However, the transition is first-order in the presence of a magnetic field.

For type-II superconductors, $\kappa > 1/\sqrt{2}$. A simplified schematic phase diagram is shown in Fig. 1.4. The type-II superconductors undergo a continuous transition at zero magnetic field. There is a third phase, called the “mixed state”, which is separated from the normal state by $H_{c2}(T)$ and from the superconducting (Meissner) state by $H_{c1}(T)$. Contrary to the case in type-I, the transitions from the mixed state to superconducting state and from normal state to mixed state both are continuous. Inside the mixed state, the magnetic flux penetrates the materials in the form of vortices. Each vortex carries a quantized amount of magnetic flux, $\Phi_0 = h/2e = 2.07 \times 10^{-15} \text{ T}\cdot\text{m}^2$. The vortex is composed of normal state electrons which form the core of vortex and superconducting electrons which circulate outside the core. The core has a size of ξ , the superconducting coherence length. The supercurrents decay for distances much greater than λ from the core.

In the GL theory of the mixed state, the vortices form a triangular array of patterns called the Abrikosov lattice [9]. When there is no vortex pinning, there

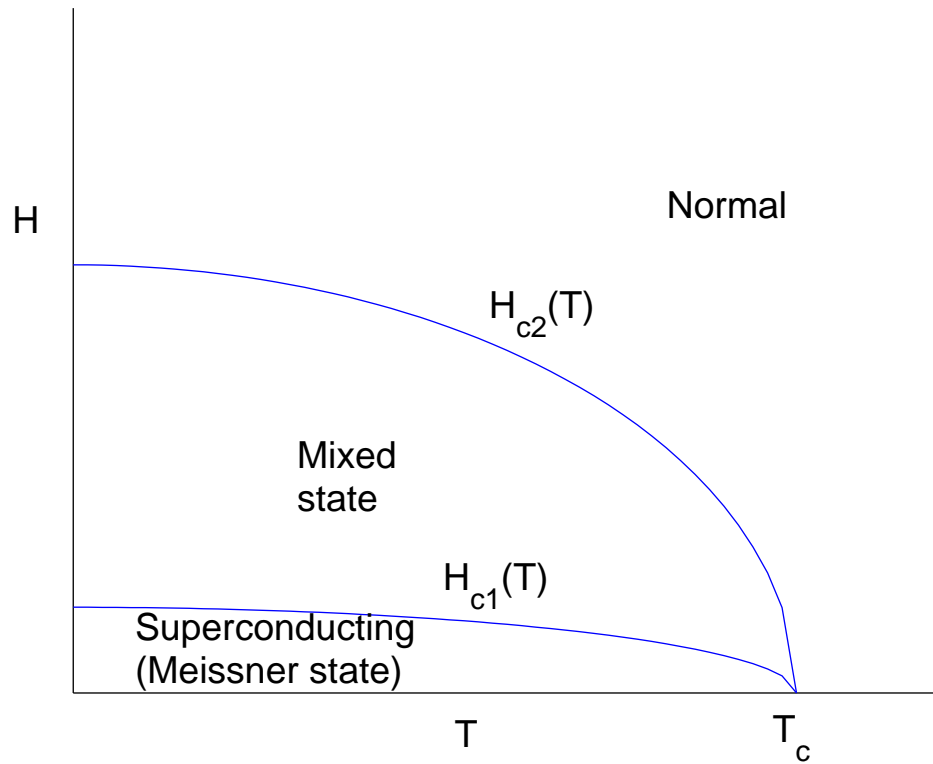


Figure 1.4: Phase diagram of a type II superconductor.

will be dissipation when a current is applied due to the motion of moving vortices since the inside of a vortex is normal. In this sense, the mixed state is not truly superconducting and has finite linear resistivity even in the limit $I \rightarrow 0$.

One of the earliest models of the motion of vortices is given by Bardeen and Stephen [10]. The theory is based on a local model that is a generalization of the London theory. Even in the presence of vortex pinning (such as defects), the theory of flux creep [11] proposed by Anderson and Kim predicts that thermal energy may allow flux lines to jump from one pinning point to another in response to the driving force of the current. The resulting flux creep leads to finite resistance in the mixed state.

After the discovery of high temperature superconductors, Fisher, Fisher and Huse (FFH) [12] proposed that the vortex-lattice phase is unstable against the introduction of quenched-disorder or random pinning and may be replaced by a vortex-glass state which has long range spin-glass order. Thermal fluctuation will cause the formation of dislocation loops of the vortex line and the vortex-glass phase can melt into the vortex liquid phase as shown in Fig. 1.5.

1.2.2 $\text{YBa}_2\text{Cu}_3\text{O}_{7-\delta}$

$\text{YBa}_2\text{Cu}_3\text{O}_{7-\delta}$ (YBCO) was discovered in 1987 [13], the first superconductor to have a T_c above the boiling point of nitrogen.

Fig. 1.6 shows the crystal structure of YBCO. It has a perovskite structure with oxygen vacancies (The oxygen vacancy determines the carrier concentration).

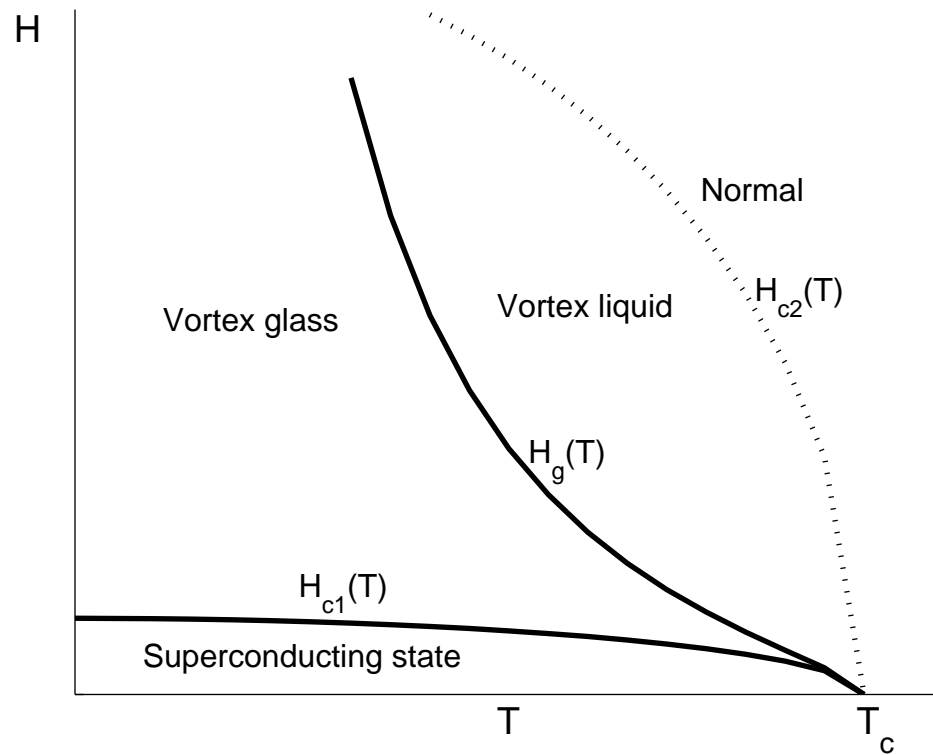


Figure 1.5: Schematic phase diagram of a 3-D type II superconductor according to Fisher, Fisher and Huse [12]. Note that $H_{c2}(T)$ is no longer a phase transition, but marks a broad crossover from the vortex liquid to normal state.

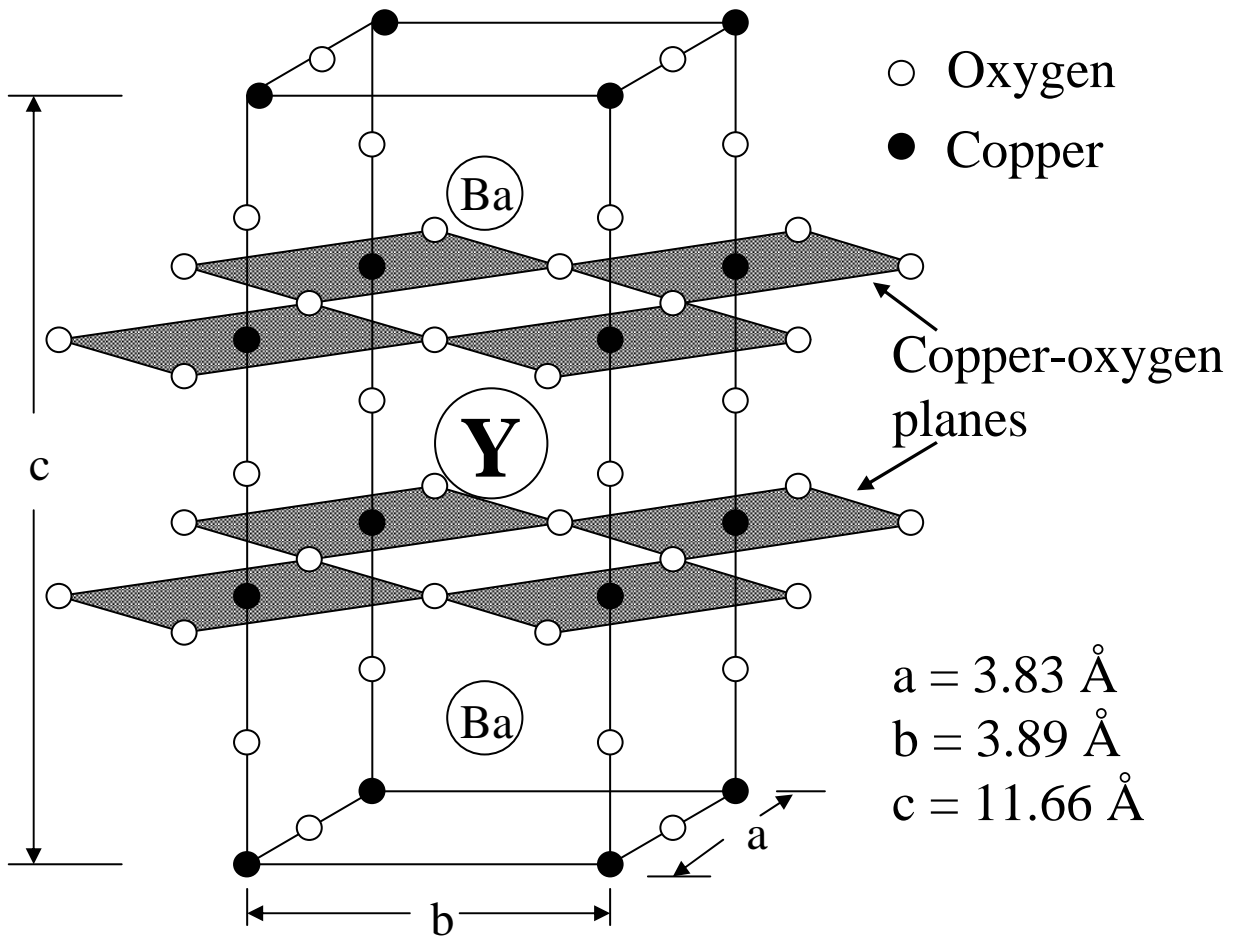


Figure 1.6: The unit cell of YBCO.

The unit cell is orthorhombic with $a = 3.818 \text{ \AA}$, $b = 3.89 \text{ \AA}$, and $c = 11.68 \text{ \AA}$. Each unit cell consists of two CuO_2 planes separated by an atom of yttrium, a CuO chain along the b direction above these planes and two barium atoms lying between the CuO_2 planes and the CuO chains. YBCO is a hole-doped superconductor since the oxygen vacancies supply carriers with positive charge.

In our experiment, we use the samples with optimal doping where T_c is highest. The reason is that the samples with optimal doping are more homogenous in T_c since small changes in doping do not affect T_c as much as they do for over- and under-

doped samples.

1.3 Critical Phenomena and Critical Exponents

Critical phenomena [4] occur in continuous phase transitions. These phenomena include scaling and power law divergences of some physical quantities, such as the divergence of specific heat $C \sim |t|^{-\alpha}$ at constant volume of PVT system at the critical point and the magnetic susceptibility $\chi \sim |t|^{-\gamma}$ in the ferromagnetic phase transition.

To describe critical phenomena, we first define an expansion parameter:

$$t \equiv \left| \frac{T - T_c}{T} \right| \quad (1.5)$$

which is a measure of the distance from the critical point in terms of reduced variables. Critical phenomena occur because the correlation length ξ , diverges at the critical point, $t \rightarrow 0$, $\xi \rightarrow \infty$.

Near the critical point, scaling theory says that thermodynamic functions can be written as

$$f(t) = At^\lambda(1 + Bt^\eta + \dots). \quad (1.6)$$

The critical exponent for the function $f(t)$ is then defined:

$$\lambda = \lim_{t \rightarrow 0} \frac{\ln(f(t))}{\ln(t)}. \quad (1.7)$$

If λ is negative, $f(t)$ diverges at the critical point as in Fig. 1.7(a) . If λ is positive, $f(t)$ goes to zero at the critical point as in Fig. 1.7(b). The $\lambda = 0$ case can

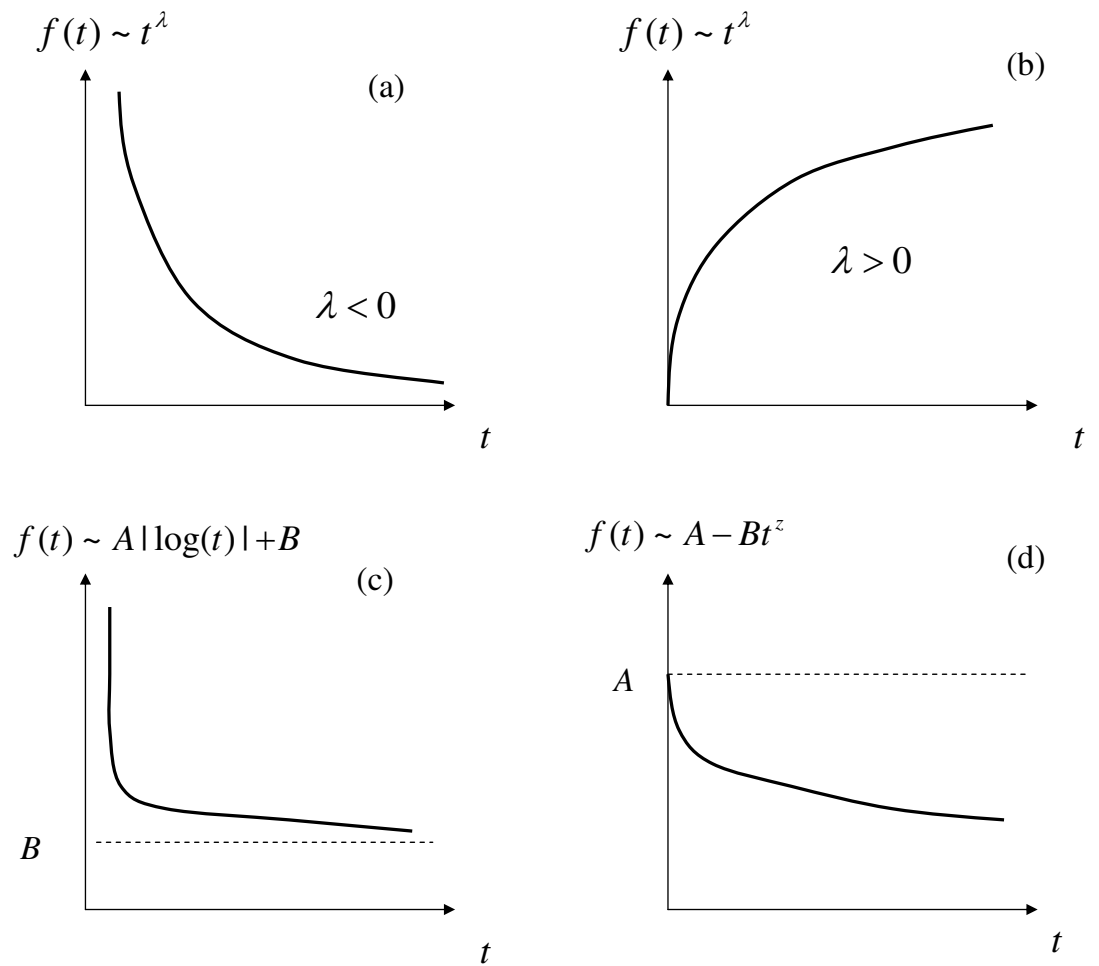


Figure 1.7: Examples of the various types of behavior near $t = 0$.

correspond to a logarithmic divergence as in Fig. 1.7(c), or a cusp-like singularity in Fig. 1.7(d).

1.3.1 Mean-Field Theory

In Ginzburg-Landau theory, the order parameter ψ is slowly varying in space, the free energy density can be expanded in the form (here we use the notation in Tinkham [6]):

$$f = f_{n0} + \alpha|\psi|^2 + \frac{\beta}{2}|\psi|^4 + \frac{1}{2m^*} \left| \left(\frac{\hbar}{i} \nabla - \frac{e^*}{c} \mathbf{A} \right) \psi \right|^2 + \frac{h^2}{8\pi} \quad (1.8)$$

where f_{n0} is the free energy density of the normal state, $m^* = 2m$ and $e^* = 2e$. Note that in Eq. 1.8 h is the magnetic field; see Ref. [6] for a discussion of the subtleties of magnetic fields and non-standard notation in superconductors. If $\psi = 0$, this will reduce to the free energy of normal state:

$$f = f_{n0} + \frac{Hh^2}{8\pi}. \quad (1.9)$$

First, we consider the case of zero external magnetic field. The difference between the normal and superconducting free energy density is

$$\Delta f = f_s - f_n = \alpha|\psi|^2 + \frac{1}{2}\beta|\psi|^4, \quad (1.10)$$

where α changes sign at T_c . By minimizing the free energy with respect to the order parameter, we find that $|\psi|^2 = 0$ (for $T > T_c$ and $\alpha > 0$) in the normal state and that the density of superconducting carriers is (for $T < T_c$ and $\alpha < 0$)

$$|\psi|^2 = -\frac{\alpha}{\beta}. \quad (1.11)$$

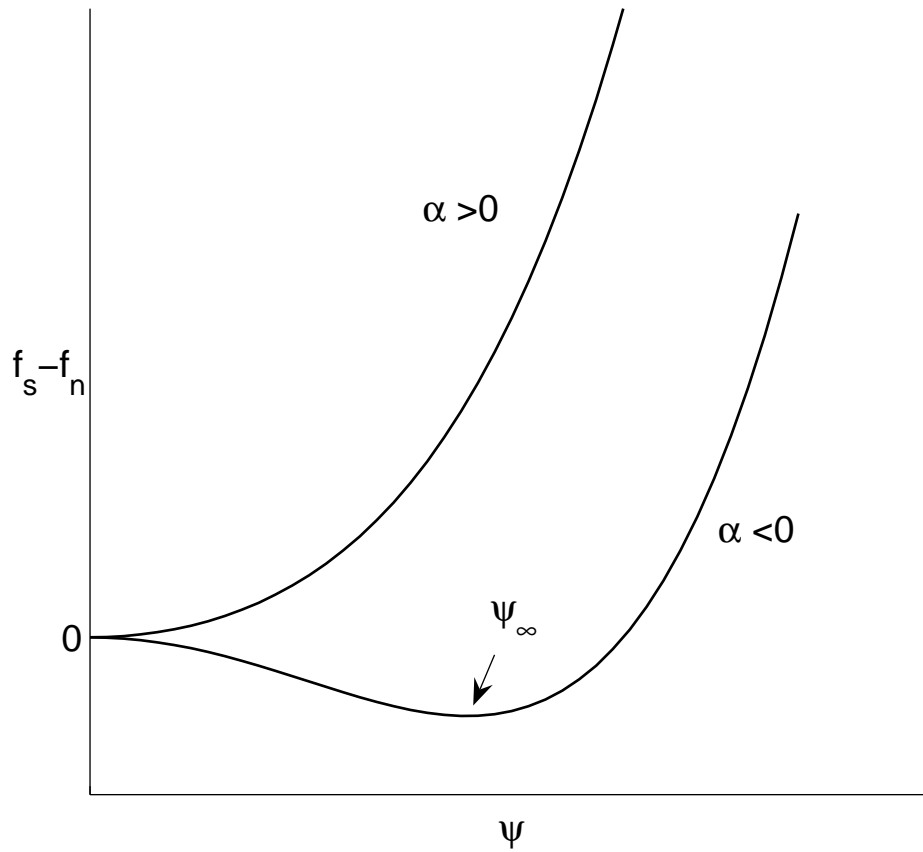


Figure 1.8: Ginzburg-Landau free-energy functions for $T > T_c$ ($\alpha > 0$) and for $T < T_c$ ($\alpha < 0$)

The corresponding free energy density below T_c is then

$$\Delta f = -\frac{\alpha^2 t^2}{\beta} \equiv -\frac{H_c^2}{8\pi}. \quad (1.12)$$

Since $\alpha(T)$ changes sign from positive to negative at T_c , we can make a Taylor series expansion of $\alpha(T)$ about T_c , keeping only the first order term:

$$\alpha(T) = \alpha' \left(\frac{T - T_c}{T_c} \right) = \alpha' t. \quad (1.13)$$

If we assume that β is a constant, Eq. (1.11) becomes:

$$|\psi|^2 \propto |t| \quad (1.14)$$

from which we may correlate $|\psi|^2$ with n_s , since $n_s \propto \lambda^{-2} \propto |t|$ is the density of superconducting electrons in the London theory.

Eq. (1.11) is the solution for minimizing the free energy without imposing any boundary conditions. We denote it as ψ_∞ . The GL differential equation can be written as:

$$\alpha\psi + \beta|\psi|^2\psi + \frac{1}{2m^*} \left(\frac{\hbar}{i} \nabla - \frac{e^*}{c} A \right)^2 \psi = 0. \quad (1.15)$$

In the case of zero external field, $A = 0$, Eq. 1.15 becomes

$$\frac{\hbar^2}{2m^*|\alpha|} \frac{d^2 f}{dx^2} + f - f^3 = 0 \quad (1.16)$$

where $f = \psi/\psi_\infty$. If we define $f = 1 + g$, by solving Eq. 1.16 to first order in g , we find that

$$g \sim e^{\pm x/\xi(T)} \quad (1.17)$$

where $\xi(T) = \sqrt{\frac{\hbar^2}{2m^*|\alpha(T)|}} \propto \frac{1}{(1-t)^{1/2}}$ is the coherence length which is the characteristic length scale over which the order parameter ψ varies. By comparing with the general

form for the coherence length $\xi \sim |1-t|^{-\nu}$, we come to the conclusion that the mean-field static critical exponent is $\nu = \frac{1}{2}$.

1.3.2 Thermal Fluctuations and the Critical Regime

Although the Ginzburg-Landau theory is successful in explaining the physical properties of conventional superconductors, it fails to explain some other second order phase transitions such as the superconducting to normal phase transition of high temperature superconductors in zero magnetic field and the vortex-glass phase transition.

In the Ginzburg-Landau theory, thermal fluctuations are ignored. In any materials, there are always thermal fluctuations in the order of $k_B T$. As the system approaches T_c , fluctuations in ψ , of energy $k_B T$, occur around the equilibrium value of ψ . This means that above T_c , regions of the material of size ξ can go superconducting while below T_c , regions of normal material appear.

If the thermal fluctuations in the GL order parameter, $\delta\psi$, remain small in comparison to the order parameter, ψ , they can be treated as perturbations to Ginzburg-Landau theory. Such small perturbations are called Gaussian fluctuations[14]. However, since ψ goes to zero as T approaches T_c , there is a temperature range close to T_c which $\delta\psi$ is in the order of ψ . In this range, called the critical regime, thermal fluctuations cannot be treated as perturbations and the Ginzburg-Landau theory breaks down [15].

In the critical regime, the energy density of thermal fluctuations is of the order

of condensation energy. Since the typical size of fluctuation is ξ , the energy density of a fluctuation in a 3D system can be approximated by $k_B T / \frac{4}{3} \pi \xi^3$. Let

$$k_B T / \frac{4}{3} \pi \xi^3 > \frac{\mu_0 H_c^2}{2}. \quad (1.18)$$

The upper critical field of H_{c2} is

$$H_{c2} = \frac{\Phi_0}{2\pi\mu_0\xi^2}. \quad (1.19)$$

The thermodynamic critical field H_c can be related to H_{c2} by

$$H_c = \frac{H_{c2}}{\sqrt{2}\kappa} \quad (1.20)$$

Combine Eq. 1.18, Eq. 1.19 and Eq. 1.20, we can derive the critical regime:

$$|T - T_c| < 72 \frac{\pi\mu_0\kappa^4}{\Phi_0^3 H_{c2}(0)} k_B^2 T_c^3. \quad (1.21)$$

For YBCO, $\kappa \approx 120$, $T_c \approx 90$ K and $\mu H_{c2}(0) \approx 100$ T. From Eq. 1.21, $|T - T_c| < 0.5$ K which is the critical regime where Ginzburg-Landau theory fails [15, 16, 17, 18].

1.3.3 Universality and the 3D-XY Theory

Universality [19] is the observation that there are properties for a large class of systems that are independent of the details of the systems. Thermodynamic phase transitions are characterized by order parameters. If phase transitions have order parameters with the same dimensions and samples have the same spatial dimensions, we say that they belong to the same universality class. Thus, behaviors close to the critical points are expected to be the same, which leads to the same critical exponents.

The order parameter of the normal to superconducting phase transition is $\psi = |\psi|e^{i\varphi}$, the dimension of which is $n = 2$. It belongs to the 3D-XY universality class, which is a three-dimensional lattice of spins rotating in a plane. Numerical simulation results generated from the 3D-XY model can be applied to the study of normal to superconducting transitions.

The Hamiltonian of the XY model can be written as [20]:

$$H = -J \sum_{\langle i,j \rangle} \mathbf{s}_i \cdot \mathbf{s}_j. \quad (1.22)$$

It is a special case of the n -vector model with spins rotating in the 2D plane ($n=2$). For $n = 1$, the n -vector model becomes the Ising model with spins confined only in one dimension. For $n = 3$, it becomes the Heisenberg model with spins rotating in three dimensions. The free energy is minimal in the ordered state, when all spins are aligned. Therefore on a 3D lattice at low temperatures there is a phase transition to an ordered state with non-zero magnetization.

Numerical simulations for the static exponent ν yield [21, 22]

$$\nu = 0.672 \pm 0.002 \quad (1.23)$$

which is different from the result from the mean field approach, $\nu = \frac{1}{2}$ [6].

Chapter 2

Experiment

2.1 Overview

Our goal was to determine the critical exponents from DC measurements on high temperature superconductors such as YBCO. We did this in zero magnetic field and non-zero magnetic field using both thin-film and single-crystal samples.

There are two parameters that characterize the continuous superconducting to normal phase transition in zero field. The first is the temperature-dependent correlation length, $\xi(T)$, which close to T_c varies as

$$\xi(T) \sim \left| \frac{T - T_c}{T_c} \right|^{-\nu} \quad (2.1)$$

which defines a static critical exponent ν . A second parameter is the correlation time $\tau(T)$, which close to T_c varies as

$$\tau \sim \xi^z \sim \left| \frac{T - T_c}{T_c} \right|^{-z\nu} \quad (2.2)$$

which defines a dynamical critical exponent z . In the case of vortex-glass phase transition, we replace ξ by $\xi_g \sim \left| \frac{T - T_g}{T_g} \right|^{-\nu}$, the glass-correlation length, where T_g is the vortex-glass transition temperature.

FFH [12] proposed the general scaling function in the fluctuation-dominated critical regime

$$\frac{E}{J} = \xi^{D-2-z} \chi_{\pm}(J\xi^{D-1}, \omega\xi^z, H\xi^2) \quad (2.3)$$

where χ_+ stands for a function above T_c (or T_g) and χ_- stands for a function below T_c (or T_g), E is the electric field, J is the applied current density, ω is the frequency, H is the magnetic field and D is the dimension of the system. We tested the scaling function by measuring the E vs. J nonlinear behavior around T_c (T_g) and we got consistent values of dynamic critical exponent z in YBCO films and crystals.

2.2 YBCO Films

Film growth

Much of our data was taken using optimized YBCO films. We grow our films in the pulsed laser deposition (PLD) lab in the Center for Superconductivity Research.

PLD is one of the thin film deposition techniques. Other methods include molecular beam epitaxy (MBE) [23], chemical vapor deposition (CVD) [24], and sputter deposition [25]. The first film deposited using the PLD technology was in 1965 by Smith and Turner (see ref. 27). However, until the 1980's, the laser deposited films were inferior to those obtained using other techniques. The breakthrough came in 1987 when Dijkkamp and Venkatesan [27] were able to laser deposit a high quality thin film of $\text{YBa}_2\text{Cu}_3\text{O}_{7-\delta}$. Fig. 2.1 shows a schematic diagram of the PLD setup (from CSR website).

In the making of $\text{YBa}_2\text{Cu}_3\text{O}_{7-\delta}$ thin films, a laser beam is first emitted from the laser. It travels through an aperture and then is reflected by a mirror. The beam is focused inside a vacuum chamber through a convex lense into a tight spot (a few square millimeters in area) to achieve greater energy densities at the target site. The

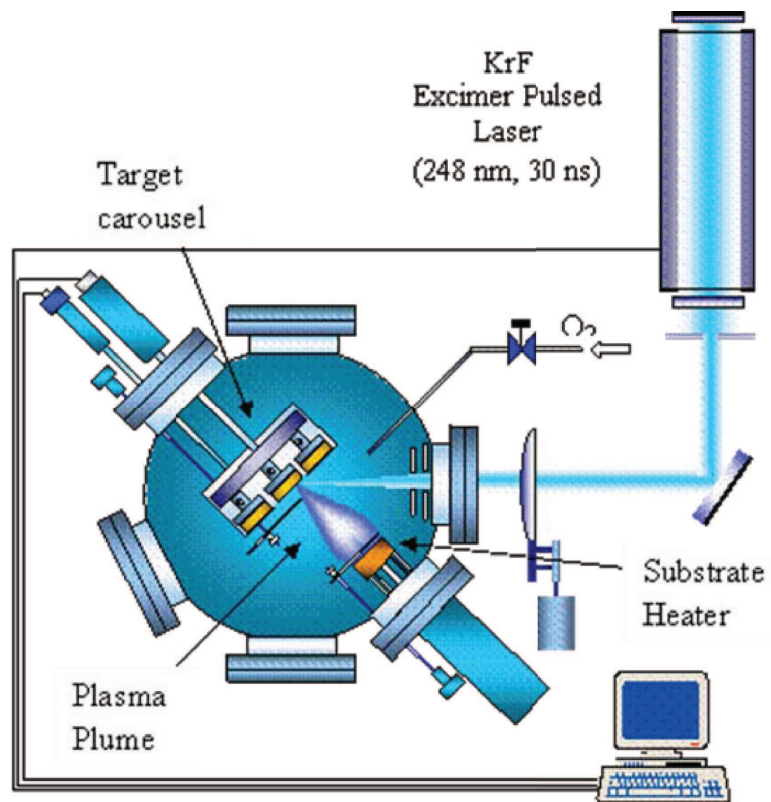


Figure 2.1: Schematic of a pulsed laser deposition setup. The figure is from CSR website.

beam strikes the YBCO target at an angle around 45° . The beam's pulse energy is absorbed within a few nanometers of the target's surface layer, which is heated to thousands of degrees. The layer is then ignited into a plasma plume containing atoms, molecules, and ions of the target. The plume interacts with the background gas chemically and physically and finally forms a thin film by condensing onto a substrate which is glued on the heater.

Our group has been making YBCO thin films for five years and we are able to make high quality films with high T_c and sharp transitions. The laser we are using is an ultra-violet Kr-F laser with $\lambda = 248$ nm and energy of 430 mJ per pulse. We set the heater temperature to be 850°C and the deposition is in a 150 mbar oxygen environment. After the deposition, we cool the film in a rate of $30^\circ\text{C}/\text{min}$ to room temperature in a 200 Torr oxygen background.

The most common substrate materials used for deposition of YBCO thin films are given in Table 2.1. LaAlO_3 substrates usually feature crystal twinning which results in the largest surface roughness amongst the three. NdGaO_3 substrates have a much smaller dielectric constant and a smaller lattice mismatch to YBCO than the SrTiO_3 substrates, so NdGaO_3 should be an ideal choice for thin-film growth. However, YBCO films grown on the NGO substrates tend to have much larger resistivity than films grown on STO substrates. Fig. 2.2 shows a comparison of the measured resistivity of YBCO films on STO and NGO substrates. Because of their low resistivity, we often use films grown on the STO substrates for the DC experiment.

Unlike the untwinned YBCO single crystals which we will introduce in section

Substrate and orientation	Lattice mismatch $\frac{\Delta a}{a}$ (%)	Lattice mismatch $\frac{\Delta b}{b}$ (%)
LaAlO ₃ (100)	0.78	2.6
SrTiO ₃ (100)	-2.3	-0.51
NdGaO ₃ (110)	<0.1	<0.1

Table 2.1: Lattice mismatches of several substrates used for deposition of YBCO.

2.3, the YBCO thin films we grow using the PLD method are heavily twinned. This is because the optimally-doped YBCO is orthorhombic and so the material is likely to be twinned. YBCO single crystals can be detwinned using the simultaneous heat and uniaxial pressure (section 2.3). The approach has been proved to be futile in YBCO thin films. Recent study [28] has shown that detwinning in YBCO thin films can be achieved by suspending a portion of a YBCO thin film above the underlying substrate. Since disorder induced by twin boundaries will not change the universality class of the phase transition in zero-field transition, we did not put the effort in the detwinning of the thin films.

After the films are prepared, we use ac susceptibility and x-ray diffraction to examine the quality of the samples. We have to make sure that the samples to be used in the DC measurements have high T_c , are c -axis oriented and homogenous. Results from bad samples are meaningless.

AC susceptibility

AC susceptibility is a standard tool for determining the physics of superconductors, in particular measuring the critical temperatures and inhomogeneities of

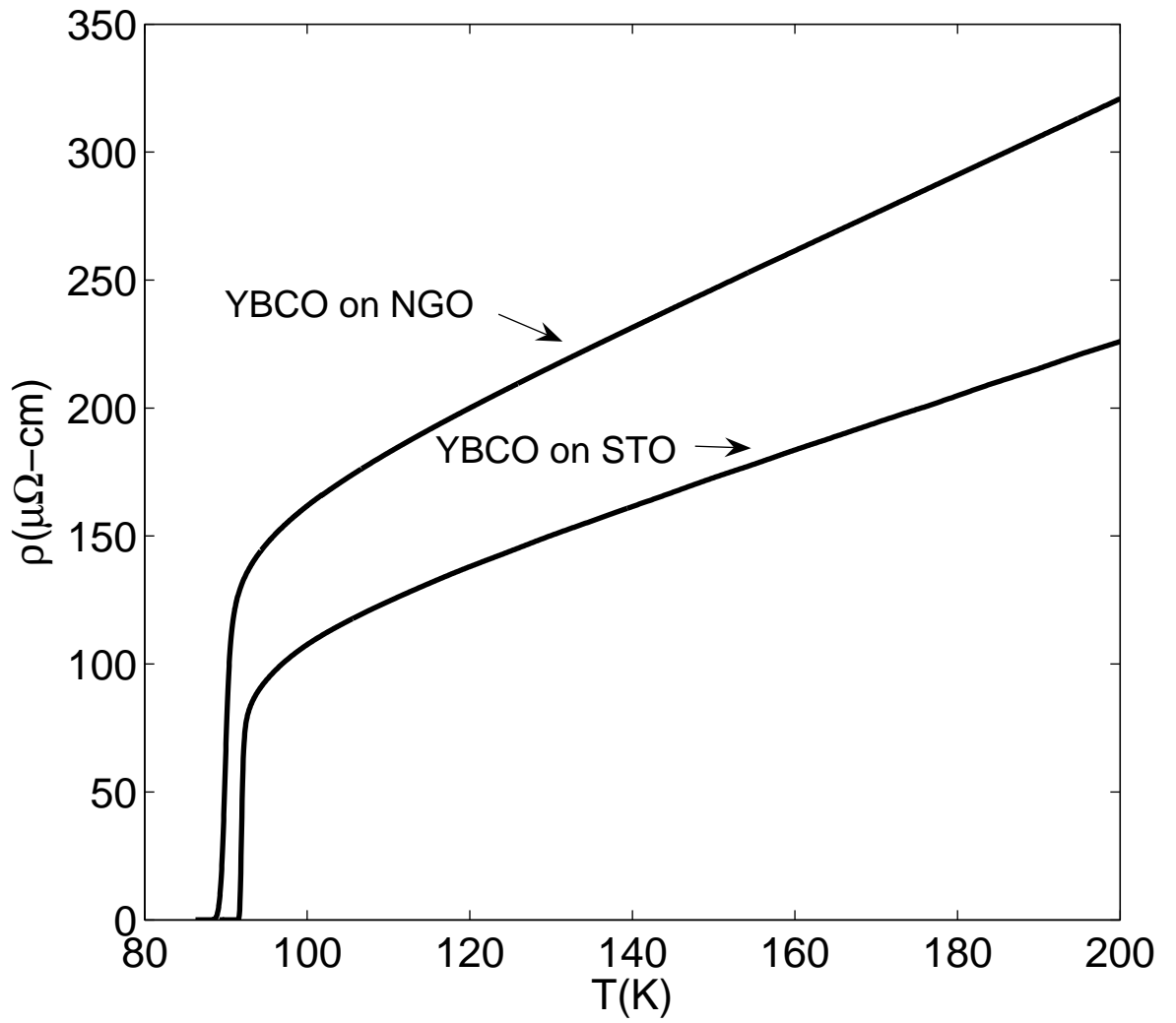


Figure 2.2: Resistivities of YBCO thin films grown on STO and NGO substrates vs. temperature.

the samples.

The magnetic susceptibility χ is defined as

$$\chi = \frac{M}{H} \quad (2.4)$$

where H is the applied magnetic field and M is the magnetization of the material.

In an ac applied magnetic field $H = H_0 e^{i\omega t}$, the material's susceptibility can be specified as a complex constant

$$\chi = \chi' - i\chi'' \quad (2.5)$$

where χ' measures the amount of magnetic flux penetrating the sample and χ'' measures how the magnetization can lag the applied field (only positive values of χ'' are physically possible).

In an ac susceptibility measurement, a small AC drive magnetic field is imposed on the DC field, causing a time-dependent moment in the sample. The time-dependent moment induces an emf in the pickup coils. Fig. 2.3 shows the schematic of an ac susceptibility apparatus. A small ac signal is applied to the drive coil. The sample is placed between the drive coil and pick up coil. By measuring the induced voltage in the pickup coil, we can get the temperature dependence of χ' and χ'' respectively.

We use a Princeton Applied Research Model 5210 lock-in amplifier to detect the signal at the pick up coil. Fig. 2.4 shows ac susceptibility data for the sample su113 which is a YBCO film grown on an STO substrate. The real part of the susceptibility decreases sharply through the transition. This is because below T_c , superconductors expel the magnetic flux ($\chi' \rightarrow -1$) and the amount of flux reaching

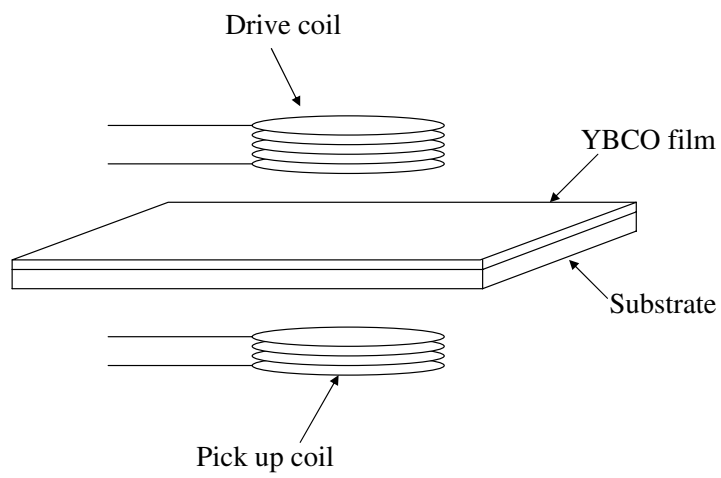


Figure 2.3: Schematic diagram of ac susceptibility measurement.

the pick up coil is greatly reduced. The imaginary part χ'' has a peak at the transition. T_c can be defined as the temperature at the maximum of the peak. The width of the superconducting to normal transition can be determined by the full width at half maximum of the peak. The narrower the peak, the sharper the transition, indicating better homogeneity of the sample. However, if there is more than one peak or the peak has a large width, it means that the sample has bad quality in that parts of the sample are a-axis oriented or the sample is inhomogeneous.

X-ray diffraction

X-ray diffraction is an excellent tool to analyze the crystalline structure of our films. It can help us investigate the formation of material phases and the orientation in thin films.

Fig. 2.5 shows a schematic diagram of the four-circle Siemens D5000 diffractometer setup we used in characterizing our films. The radiation is emitted from the X-ray tube, diffracted by the film and received by the detector. The diffraction angle (2θ) of the reflected beam always doubles the incident angle (θ). When the Bragg condition is satisfied,

$$2d \sin \theta = n\lambda \quad (2.6)$$

we expect constructive interference. In Eq. 2.6, d is the interplanar spacing, θ is the incidence angle, n is the diffraction order and λ is the X-ray wavelength.

During a $\theta - 2\theta$ scan, θ is changed, for a fixed d (which is 3 Å for YBCO films), there are certain values of θ which satisfies the Bragg condition and constructive interferences show up as large peaks.

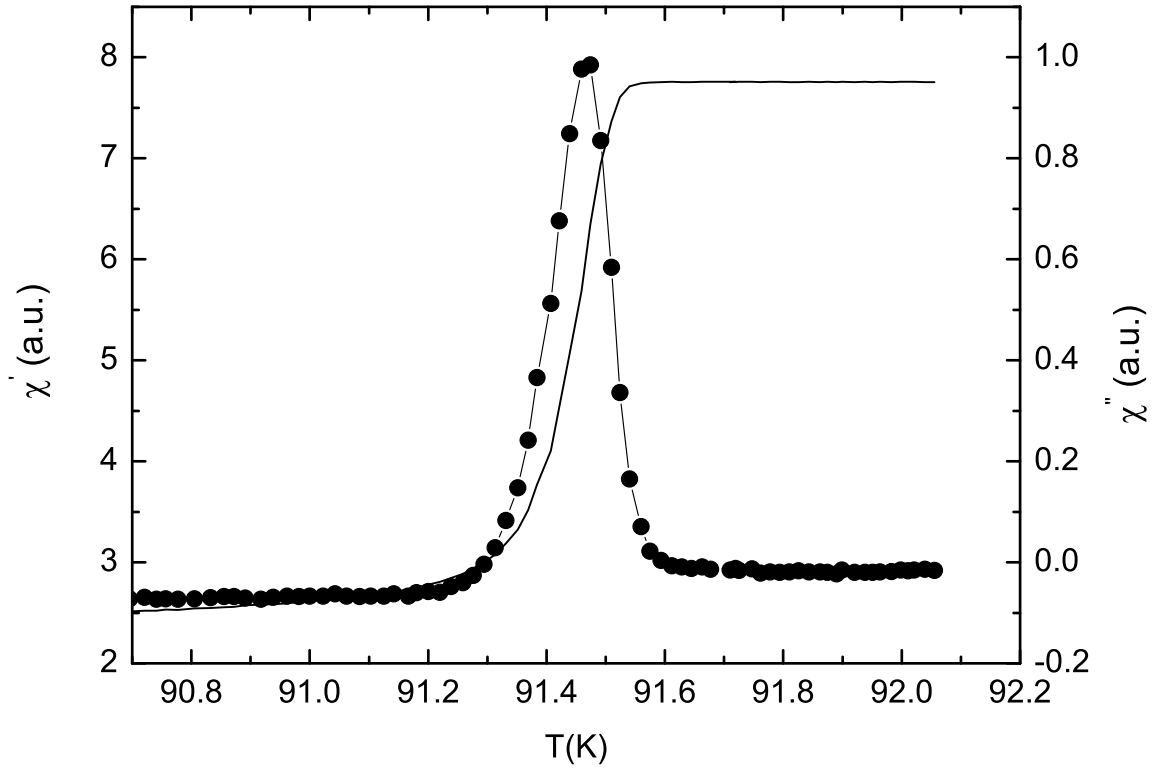


Figure 2.4: AC susceptibility of sample su126 with real (solid) and imaginary (with circles) parts. The transition temperature determined from the figure is around 91.45 K and the transition width (full width of half maximum) is 0.2 to 0.3 K.

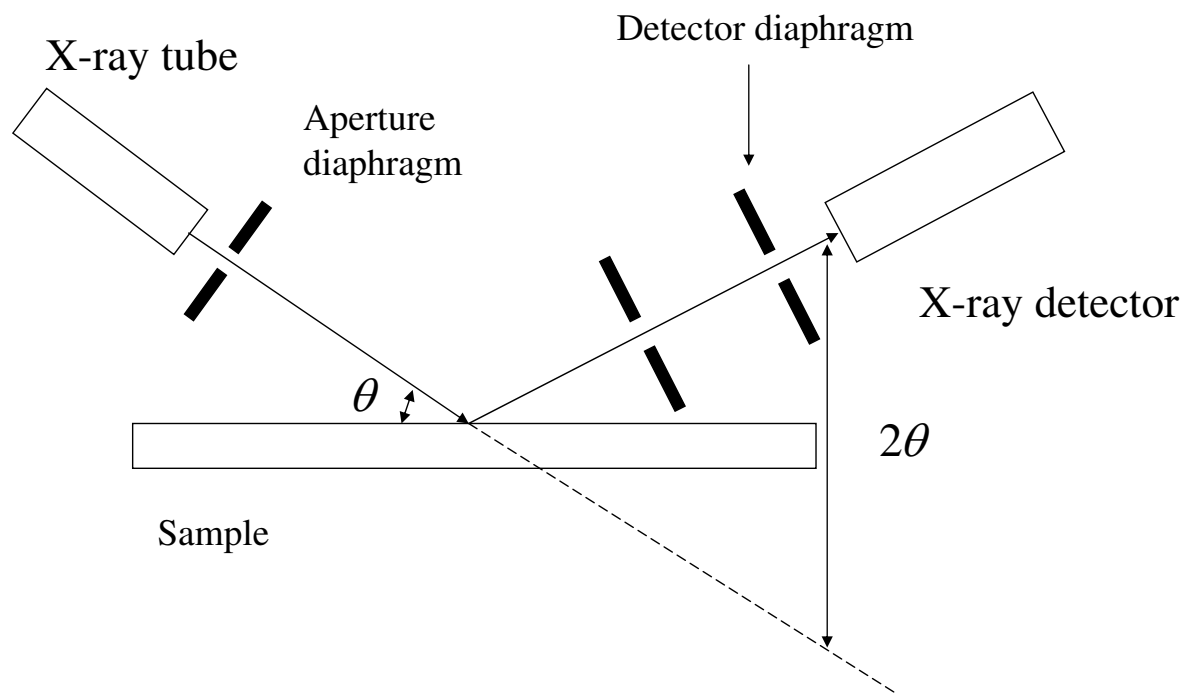


Figure 2.5: Schematic of a X-ray setup.

Fig. 2.6 shows a $\theta - 2\theta$ XRD scan of a c -axis oriented film on STO substrate. The only clearly visible peaks are ($n00$) of YBCO and the substrate peak which indicate a good c -axis orientation.

Patterning

After we get high quality YBCO films, we use optical lithography and chemical etching to make the pattern to be used in the DC transport experiment. The photoresist we use is Shipley S-1813. We spin photoresist on the films at 5000 rpm for 50 seconds, and then bake it on a hot plate at 90 °C for 1 minute. This produces a 1.0 μm thick layer of photoresist. We then put a film on the mask aligner and place a chrome mask on top of the films. We expose the film using UV light with intensity of 8 mW/cm² for 12.5 seconds. After the exposure, we develop the pattern in CD-30 for 7 seconds and a pattern of photoresist will show up on top of the film.

After development, we use chemical etching to remove the YBCO that is not covered by the photoresist. The advantage of chemical etching is that it is easier to operate, takes less time and does not affect the composition of the unexposed sample. We use 0.5% (in volume) of phosphoric acid (H₃PO₄) solution in water. In most cases, the etching rate is 100 \AA per second. However, if we etch the sample for too long, the sample will be over-etched and the bridge of the pattern will be thinner than expected.

Fig. 2.7 shows a photograph of the pattern after photolithography and chemical etching. The black region is the YBCO film and the gray region is the STO substrate. The current will flow from “I₊” to “I₋” and the voltage will be measured at “V₊” and “V₋”. This is a typical four-probe pattern.

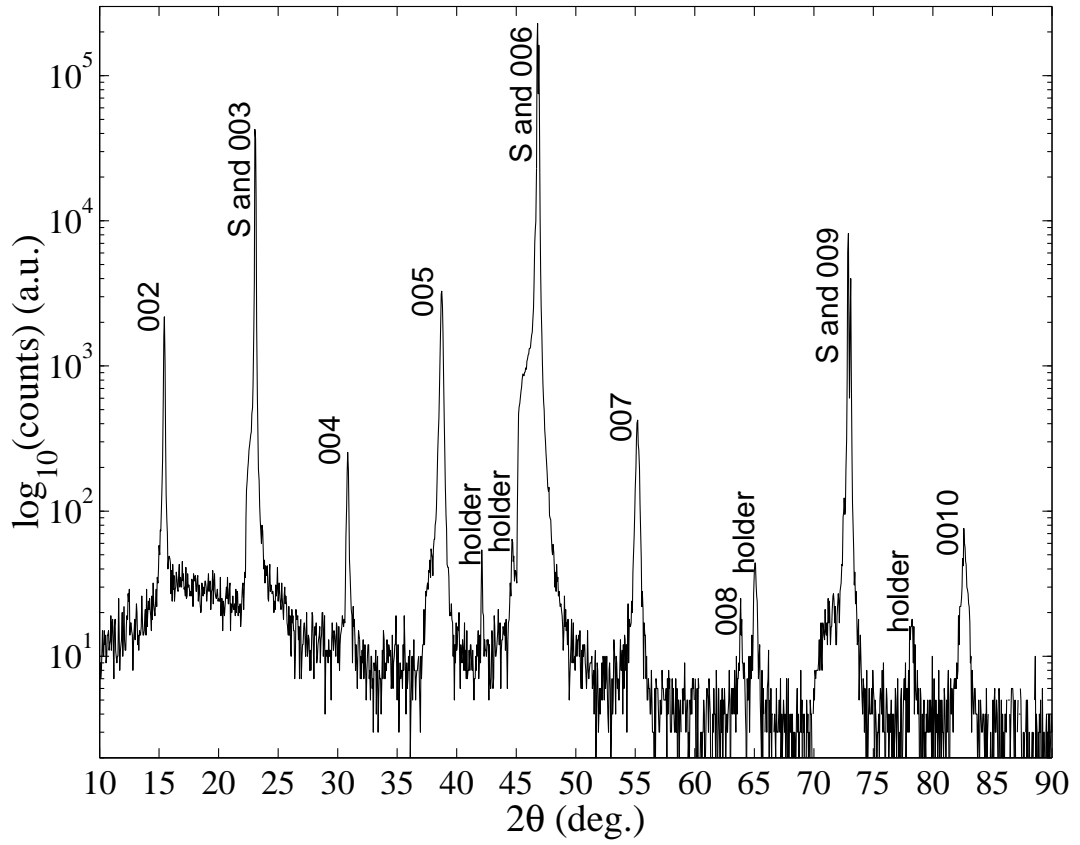


Figure 2.6: X-ray diffraction pattern for a YBCO thin film (sample mcs89) [17]. 00n stands for peaks of YBCO, holder stands for peaks of sample holder and S stands for peaks of substrate.

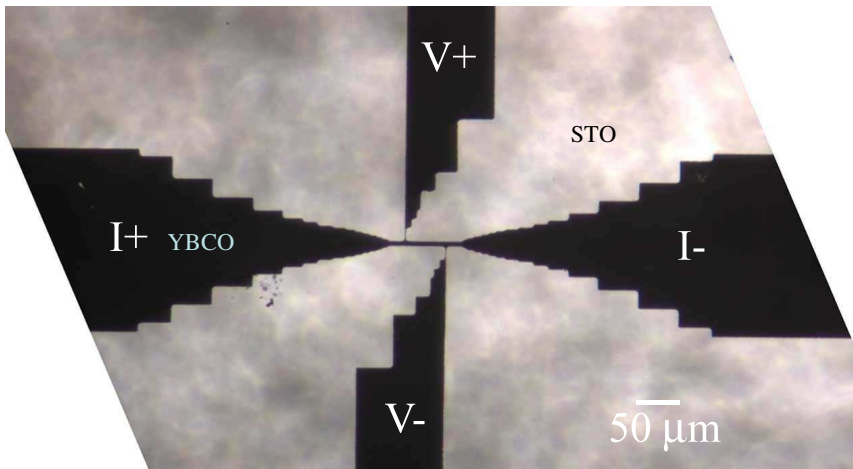


Figure 2.7: Photograph of a YBCO's bridge pattern for sample ro68. The bridge dimensions are $8 \times 40 \mu\text{m}^2$.

2.3 YBCO Crystals

We received untwinned optimally-doped YBCO crystals from Dr. Kouji Segawa and Dr. Yoichi Ando in Central Research Institute of Electric Power Industry. The YBCO single crystals were grown in Y_2O_3 crucibles by a conventional method [29, 30]. Before detwinning, the crystals are annealed to be tuned to the targeted oxygen content (optimally-doping at $\delta = 0.05$). The crystals are always quenched at the high temperature annealing. Detwinning is performed at temperature below 220 °C under a uniaxial pressure of 0.1 Gpa.

After detwinning, the crystals are left at room temperature for at least 7 days for the oxygen to equilibrate. During this process, the oxygen content does not change, however, the oxygen atoms tend to order locally to form longer Cu-O chains. The typical T_c of the optimally-doped YBCO crystals can be higher than 93 K with a transition width of 0.5 K.

Fig. 2.8 shows the photograph of a YBCO crystal sample with four probe contacts. The contacts are made by gold wires attached to the crystal using silver paste. Because of difference in contact area, the contact resistance of the current contacts is less than 0.5 Ω and contact resistance of the voltage contacts is less than 5 Ω . The current flows through the a -axis. We present ρ_{aa} vs. T in Fig. 2.9.

2.4 DC Measurements in Zero Magnetic Field

Experimental Setup

We have excellent probes to perform the DC transport experiments (measuring

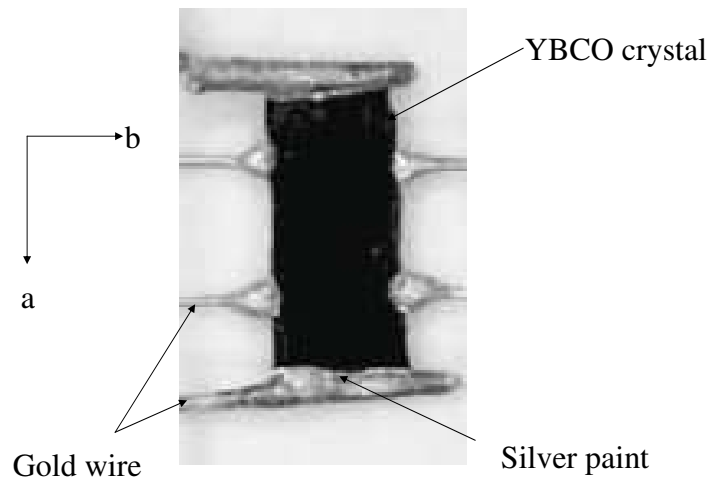


Figure 2.8: Photograph of a YBCO crystal sample with contacts. The picture is from reference [29]

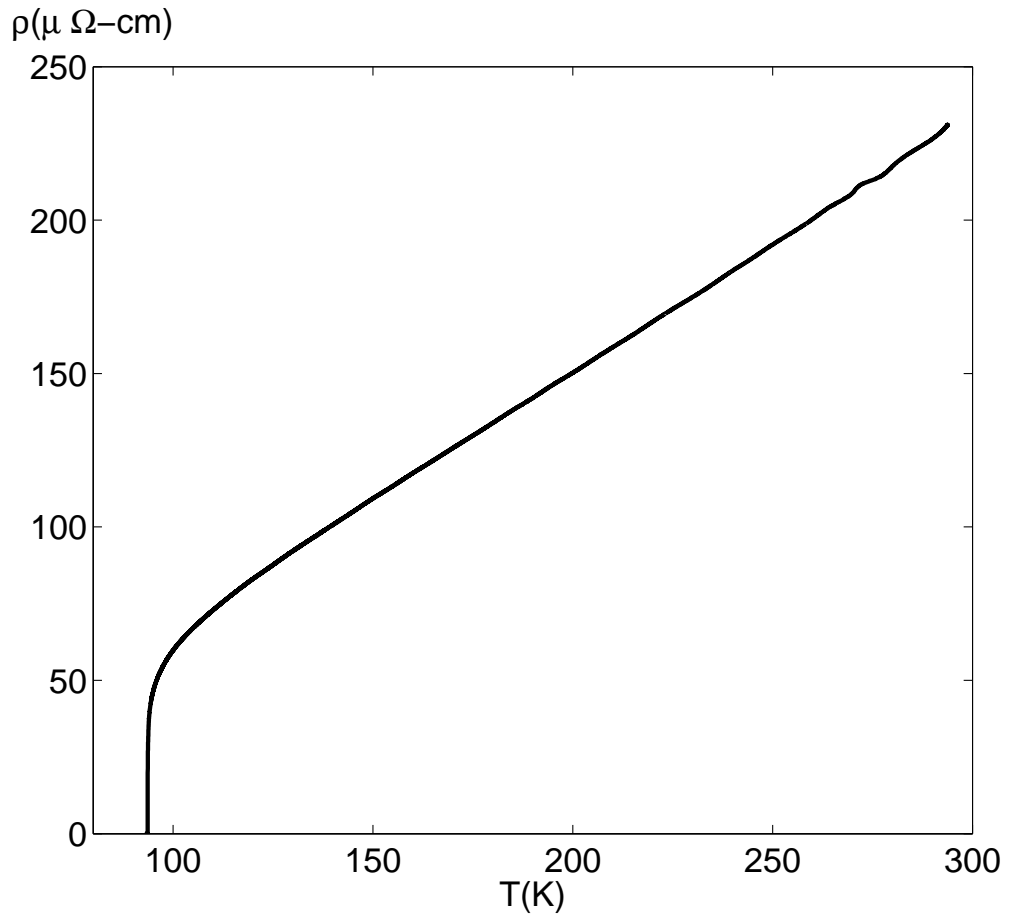


Figure 2.9: Resistivity vs. temperature of an untwinned YBCO optimally-doped single crystal (sample C1).

voltage vs. current) in zero field. Fig. 2.10 shows a photograph of the experimental setup. The sample is placed in the probe which is suspended in a cryostat filled with liquid nitrogen (for YBCO). The bath cools the sample to where the phase transition occurs. The cryostat is surrounded by three layers of μ -metal shields to reduce the ambient field to less than 10^{-7} T which is essential to our zero field measurements. The effect of ambient field on the experiment has been extensively discussed by M.C. Sullivan *et al.* [31]. Magnetic fields as small as the earth's magnetic field $50 \mu\text{T}$ can change the shape of $I - V$ curves and induce ohmic tails at low currents below T_c .

The whole setup is placed inside a screen room and has low pass filters both inside the probe and at the wall of screen room. The double T filters inside the probe have 3 dB point at 3 KHz and the Pi filters at the wall of the screen room have 3 dB point at 5 KHz. Theory predicts that noise will cause ohmic tails at low current densities. Strachan [18] and Sullivan [17] have measured $I - V$ curves for the same sample with and without filtering. They have found that at high currents, the two sets of $I - V$ curves collapse. However, at low currents, they have seen ohmic tails in the isotherms taken without filtering that are not present in the isotherms taken with filtering. By installing low-pass filters, we can reduce the ohmic tails caused by the noise.

The currents to the sample are applied by a Keithley 224 current source and the voltages are measured by a Keithley 182 nano-voltmeter. The temperature of the sample is regulated by the Neocera LT-21 temperature controller. The precision of the temperature control is 1 mK.

Fig. 2.11 shows photographs of the probe. The high- T_c superconducting films

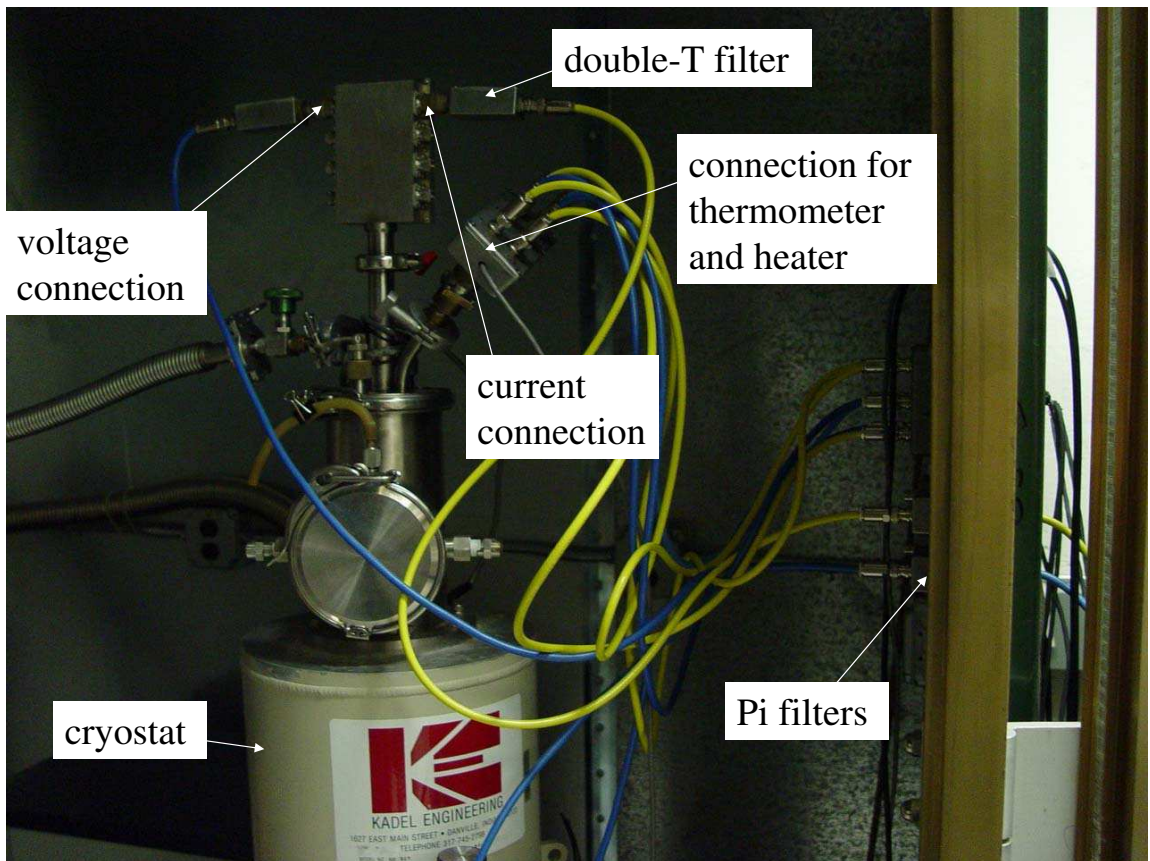


Figure 2.10: Photograph of the setup of the zero-field measurement.

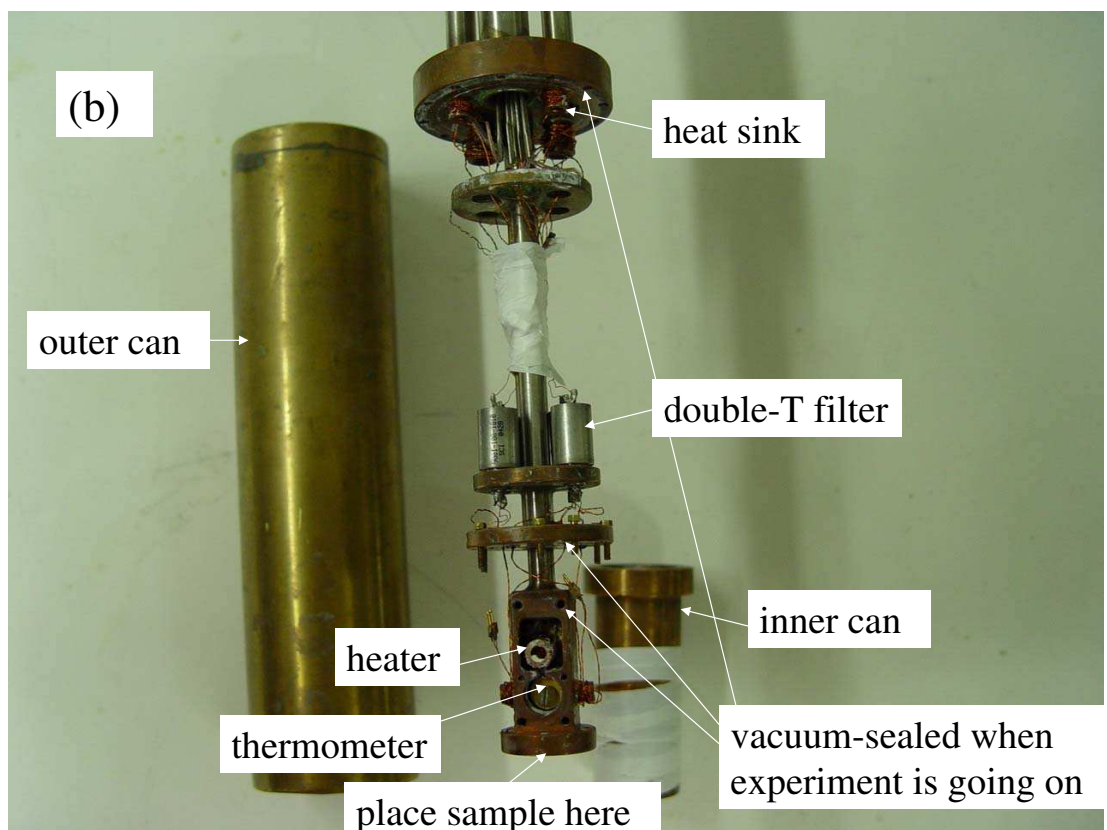
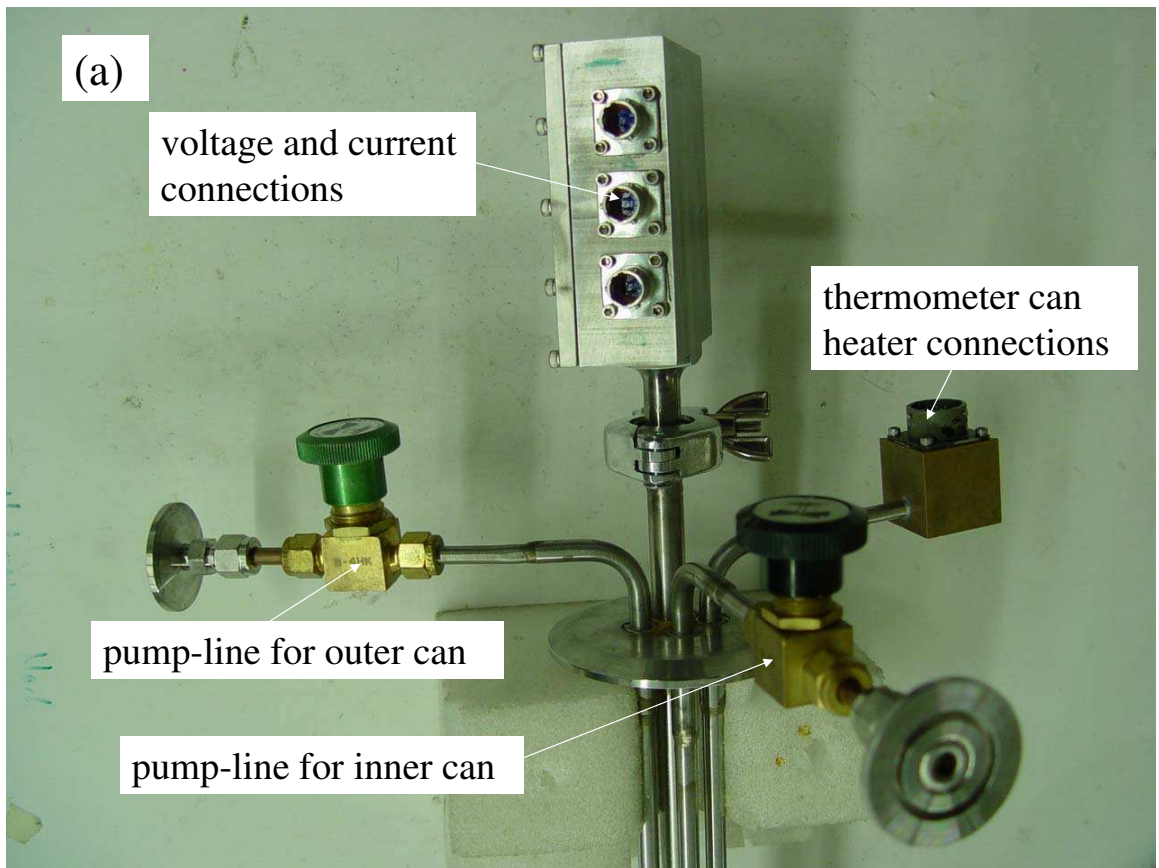


Figure 2.11: (a) Head of the probe. (b) Bottom end of the probe.

are thermally anchored on a block of OFHC (oxygen free high conductivity) copper (sample stage). The thermometer and heater are placed inside the copper block. The thermometer is Cernox 1080 model made by Lakeshore. The heater is home-made, consisting of twisted-paired high-resistance wire winding around a small copper cylinder. The whole sample stage is put inside an inner can made of brass. The inner can has vacuum separate from the outer can which means that we can put exchange gas into the inner can and have the temperature controllers set the sample and the inner can at the same temperature. In this exchange gas method, we can greatly reduce the heating occurring in the sample.

Measurement Technique

We use four-probe measurements in the DC transport experiment. This method allows us to measure the voltage across the sample without the interference of the contacts. We first apply current I to the sample and set the desired temperature of the sample using the temperature controller.

Once the temperature of the sample is stable, we measure the voltage ΔV_1 using the Keithly 182. This ΔV_1 , however, includes the voltage drop across the bridge of the sample (ΔV) in addition to thermal emfs (ΔV_{emf}). A thermal emf is caused at a junction of two dissimilar metals. In our setup, the solder joints between the different metal wires are inevitable and the thermal emf is usually in the order of $1 \mu\text{ V}$. By applying current I in the opposite direction and taking another measurement ΔV_2 , we can eliminate the thermal emf effect.

After switching the sign of the current, the intrinsic voltage across the sample

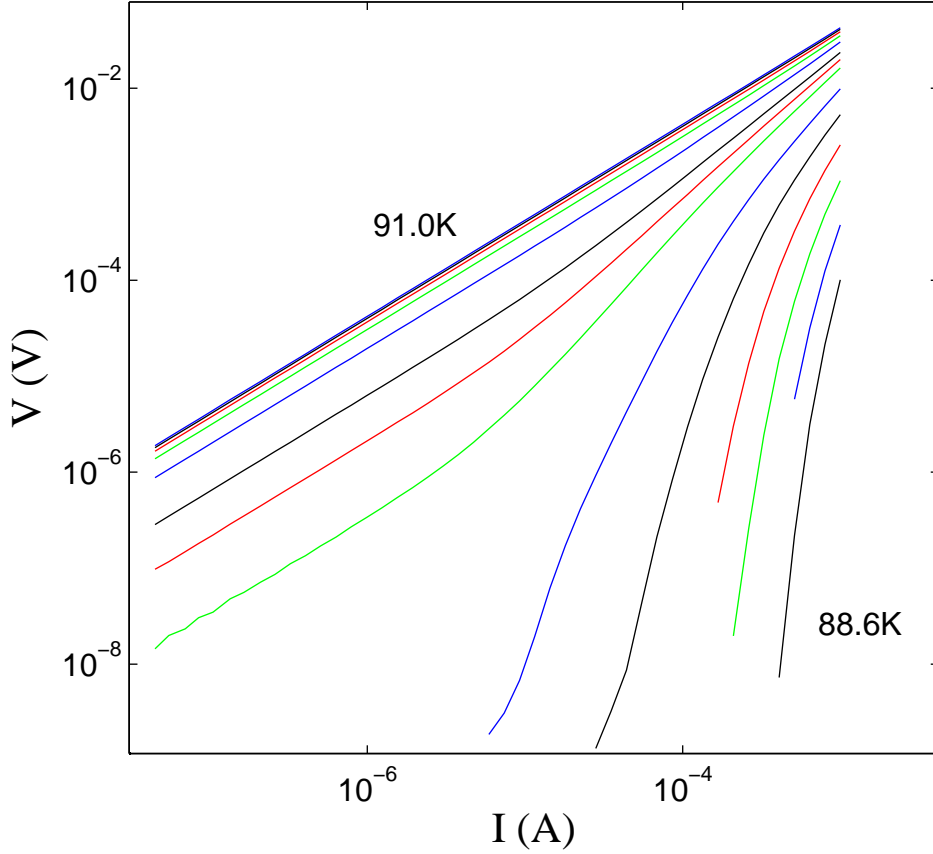


Figure 2.12: $I - V$ curves for sample su058.

bridge can be derived from

$$\Delta V = \frac{\Delta V_1 - \Delta V_2}{2} = \frac{(\Delta V + \Delta V_{emf}) - (-\Delta V + \Delta V_{emf})}{2}. \quad (2.7)$$

V_{emf} can be cancelled out by the reverse polarity measurement.

Suppose we take n measurements, the average of the voltage measurements is \bar{V} and the standard deviation is $\sigma_{\bar{V}}$. In order to get a precise voltage, we repeat the reverse polarity measurements until either of the following two conditions have been met. The first condition is that $\frac{\sigma_{\bar{V}}}{\bar{V}} < 1000$ and the second condition is that

$\sigma_{\bar{V}} < 1$ nV. In this way, we can make very precise measurements over many decades in current and voltage. In Fig. 2.12, we present the \bar{V} vs. I curves from 91.0 K to 88.6 K of sample su058. The spacing between each isotherm is 0.2 K.

Low frequency measurements

Heating can distort the I-V curves at high current. To reduce the heating, we can either reduce the contact resistance by depositing gold on the contacts or reduce the width and length of bridges so that we could pass a smaller current through the contacts while maintaining E and J (a more detailed discussion on the relation of the dimensions of the bridges of film with heating can be found in Chapter 3).

There is another method using the swept-AC technique which can reduce the heating. It was originally used in the transport measurement to study the vortex-glass phase transition by Koch *et al.* in [48, 62]. The schematic setup is shown in Fig. 2.13. Instead of the discrete method we introduced earlier, this method applies an AC sinusoidal current. Suppose the frequency of the AC current is ω and the relaxation time of the sample is τ . If $\omega\tau \gg 1$, which means the sinusoidal wave oscillates faster than the relaxation rate of the sample, the sample will be at a relatively constant temperature over the whole current range (The high and low currents are at the same temperature). The ac method thus ensures that all current-induced heating is averaged to a steady temperature offset (ΔT) applying to the whole curve.

The disadvantage of the AC method is that we cannot get good resolution at low currents due to the limitation of our setup. The data at high currents look smooth but are too noisy to perform a derivative plot (Chapter 3). A comparison of

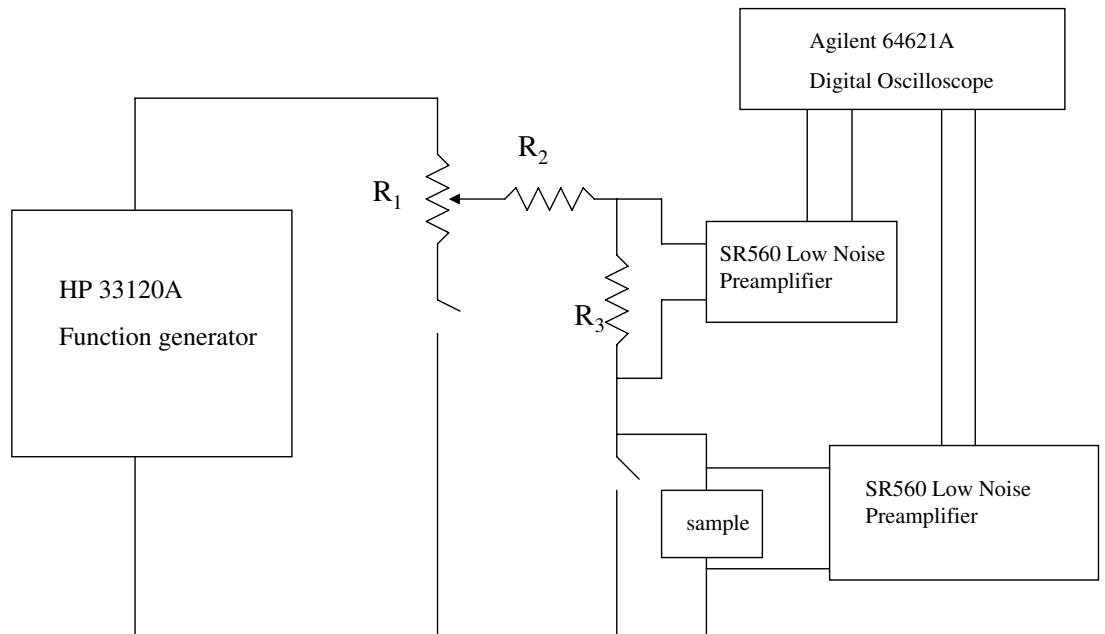


Figure 2.13: Schematic of low frequency measurement setup.

the high currents results between ac sweep method and DC discrete method can be found in [18] (page 75). The two sets of $I - V$ curves start to deviate just below 1 mA for the same YBCO film. It tells us that $I - V$ curves above 1 mA are distorted by the heating effects.

2.5 DC Measurements in Magnetic Field

The DC transport measurements in magnetic field up to 9 T are performed in the “Blue” magnet. The “Blue” magnet is a Cryomagnetic cryogenic system consisting of a dewar made by Precision Cryogenic Systems with magnet inside and an insert made by Janus. A schematic diagram is shown in Fig. 2.14

We use the same sample probe as we used in the DC measurements in zero magnetic field. The helium vapor flows through the needle valve from the helium bath to the sample space to cool the sample. The sample space temperature can be controlled by changing the He gas flow and by a Lakeshore temperature controller which controls the temperature of the vaporizer. The superconducting magnet can provide a magnetic field of 9 tesla without pumping the helium bath and a maximum field of 11 tesla by lowering the helium bath temperature down to 3 K.

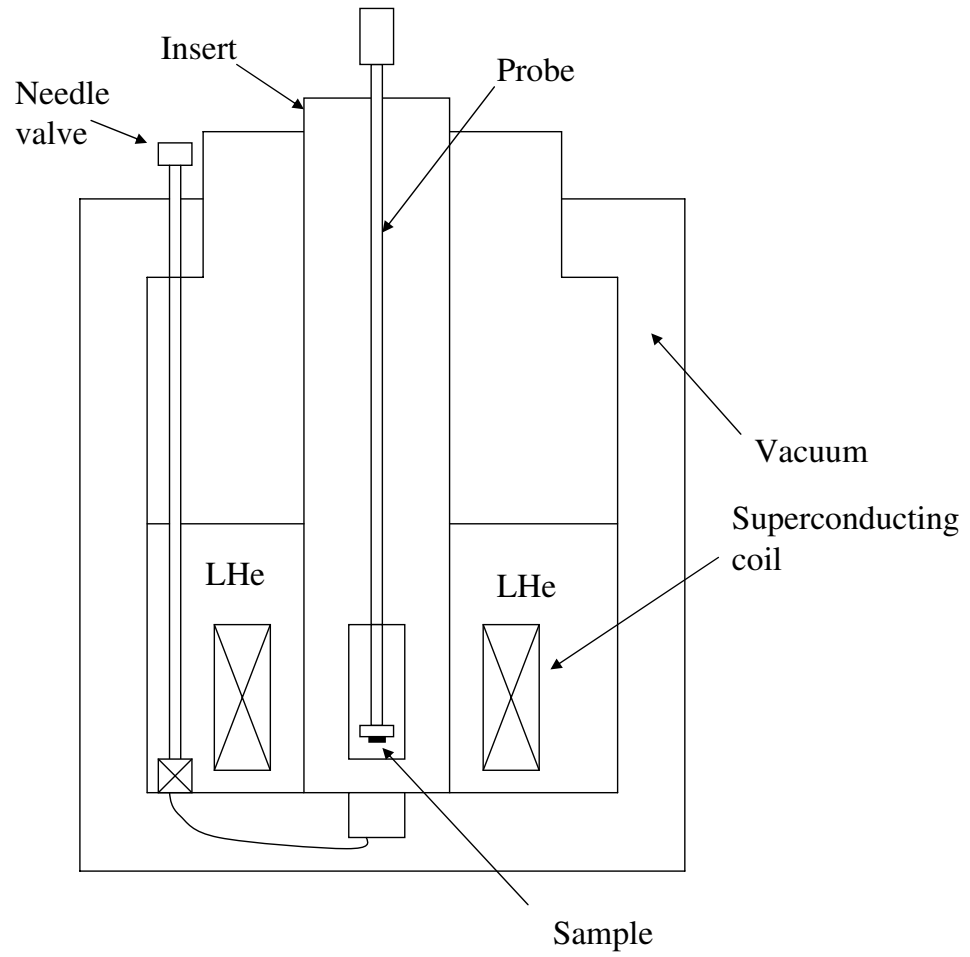


Figure 2.14: Schematic of the “Blue” magnet.

Chapter 3

The Superconducting Phase Transition of YBCO in Zero Field

The high critical temperatures (T_c), large penetration depths (λ), and short coherence lengths (ξ) of high-temperature superconductors make it possible to measure critical fluctuations in these materials, in contrast to conventional superconductors. In spite of nearly two decades of work, however, experimental results are not consistent, and do not always agree with theory.

It is generally accepted that ν should be close to 0.67 in a superconductor in zero magnetic field, since the phase transition belongs to the three dimensional XY universality class [19]. There are some specific heat [33, 33, 35] and thermal expansivity [34] data which agree with theory, although there are others [36, 37] which do not. The exponent ν has also been inferred from DC and high-frequency electrical measurements. Some of these measurements [43, 54] agree with the XY model, and others [44, 53, 52] do not, yielding values of ν between 1.1 and 1.5.

The situation for the dynamical exponent z is even more uncertain. Fisher, Fisher, and Huse [12] argue that motion of vortex loops should be diffusive, so that model A dynamics [19], which give $z = 2$, should apply. Other theoretical considerations yield that $z = 1.5$ [38], as for model E and model F dynamics [19]. Lidmar [39] and Weber [40] argue that z should be around 1.5 by Monte Carlo

simulation. Experimental results vary even more widely. Yeh *et al.* [42] found $z \approx 2$ from $\text{YBa}_2\text{Cu}_{2.98}\text{Au}_{0.02}\text{O}_{6.97\pm 0.02}$ single crystal and epitaxial films in [42], but later found $z \approx 3$ in twinned superconducting $\text{YBa}_2\text{Cu}_3\text{O}_{7-\delta}$ crystal in [43]. Booth *et al.* [44], using microwave conductivity scaling, found that $z \approx 2.6$. Moloni *et al.* [45] found that $z \approx 2.3$ and later found $z \approx 1.25$ for under-doped $\text{YBa}_2\text{Cu}_3\text{O}_{7-\delta}$ films.

Although the critical exponents should be universal, there is at present no consensus in the field. We test universality by doing DC measurement on both $\text{YBa}_2\text{Cu}_3\text{O}_{7-\delta}$ crystals and films. We show that z and ν obtained from film data agrees very well with the z obtained from crystal data. We argue that the wide ranges for both z and ν reported in the literature, are due to the finite-size effects present in films.

3.1 The Zero-Field Transition

In the zero-field transition of high temperature superconductors, thermal fluctuations dominate the critical regime. The correlation length, ξ , also the typical size of a fluctuation, diverges at T_c as [12]

$$\xi = \xi_0 \left| \frac{T - T_c}{T_c} \right|^{-\nu}. \quad (3.1)$$

The fluctuations are dynamic and they pop in and out of existence. The typical life time of a fluctuation is τ , also diverging at T_c as [12]

$$\tau \sim \xi^z. \quad (3.2)$$

The scaling function for the nonlinear dc conductivity is in the form of [12]

$$\frac{E}{J} = \xi^{D-2-z} \chi_{\pm}(J\xi^{D-1}). \quad (3.3)$$

3.1.1 Scaling Theory

The assumption underlying the scaling theory is that physical properties depend only on ξ and τ if the system is very close to the critical temperature T_c . We will use a dimensional analysis to derive the scaling behavior of E and J as shown in Eq. 3.3.

We know that

$$E = -\frac{\partial A}{\partial t} \sim \frac{A}{\tau} \quad (3.4)$$

where A is the vector potential. Using dimensional analysis, we can postulate that

$$A \sim \frac{\Phi_0}{\xi}. \quad (3.5)$$

Combining Eqs. 3.4 and 3.5 we arrive at

$$E \sim \frac{\Phi_0}{\xi\tau} \sim \xi^{-1-z}. \quad (3.6)$$

We thus conclude that $E\xi^{1+z}$ is an appropriate dimensionless scaling variable.

We next try to find how J scales with ξ . We follow the argument in [18] and [17]. The typical fluctuation region in a D dimensional space is in a size of ξ^D . The power dissipated in this volume is proportional to $JE\xi^D$. We equate this to the thermal energy over the lifetime of a fluctuation, $k_B T/\tau$,

$$JE\xi^D \sim \frac{k_B T}{\tau}. \quad (3.7)$$

Combining Eq. 3.6 and Eq. 3.7, we can conclude

$$J \sim T\xi^{1-D}. \quad (3.8)$$

The appropriate scaling combination is $J\xi^{D-1}$.

Having obtained the scaling of E and J with ξ , we can write a scaling ansatz as

$$E\xi^{1+z} = F_{\pm}(J\xi^{D-1}) \quad (3.9)$$

for temperatures above (+) and below (-) the critical temperature T_c where F_{\pm} is an appropriate scaling function.

Eq. 3.9 can also be written as

$$\frac{E}{J} = \xi^{D-2-z}\chi_{\pm}(J\xi^{D-1}) \quad (3.10)$$

where we follow the convention of dropping the $T \approx T_c$ in Eq. 3.8. The scaling function behaves as $\chi_+ \rightarrow \text{constant}$ as $J \rightarrow 0$ implying a finite resistivity and $\chi_- \sim e^{-a/J}$ due to vortex-loop unbinding, as seen in the following section.

We then introduce two useful arguments from the scaling function. In the limit of $T \rightarrow T_c$, $\xi \rightarrow \infty$. The ξ^{D-1} term in the right hand side of Eq. 3.10 will diverge. In order to make the left hand side of the equation remain finite, we have to require that $\chi \sim (J\xi^{D-1})^x$ to cancel the ξ^{D-2-z} term. This will lead to

$$\xi^{D-2-z+x(D-1)} \sim \text{constant} \quad (3.11)$$

and

$$x = \frac{2+z-D}{D-1}. \quad (3.12)$$

Combining Eq. 3.10 and Eq. 3.12, we can find the power law relationship of E vs. J at T_c

$$E \sim J^{\frac{z+1}{D-1}}. \quad (3.13)$$

Above T_c , as $J \rightarrow 0$ (in the low current limit), $J\xi_{D-1} \rightarrow 0$ and χ_+ becomes a non-zero constant

$$\rho = \frac{E}{J} = \xi^{D-2-z} \chi_+(0) \sim \left| \frac{T - T_c}{T_c} \right|^{\nu(D-2-z)}. \quad (3.14)$$

3.1.2 Vortex-Loop Unbinding

In the Meissner state, according to the mean field theory, there is no dissipation occurring which is linear in the current density up to a critical current density. However, due to thermal fluctuations, the system can dissipate energy when the applied current is less than the critical current. The fluctuations take the form of vortex loops. The nucleation and subsequent growth of vortex loops leads to a nonlinear $E - J$ relation in the Meissner state.

According to FFH [12], below T_c , when a current is applied to the sample, the vortex loops will feel a force of $J\Phi_0$ per unit length. This Lorentz force will either compress or expand the loops depending on the orientations of the loops. Compressing the vortex loop will cause no net dissipation, so we only study the case where the current expands the loop. The effective potential due to the Lorentz force is

$$-\pi J\Phi_0(R^2 - \xi_{GL}^2) \quad (3.15)$$

which can be derived from integrating $-F_{\text{lorentz}} dr = -2\pi J\Phi_0 r dr$, where R is the

radius of the loop. Thus, the free energy of a circular vortex loop lying in a plane normal to the current, of radius $R > \lambda$ and having the appropriate sign of the orientation, is

$$U_{loop} \approx 2\pi R\varepsilon - J\Phi_0\pi R^2, \quad (3.16)$$

where $2\pi R\varepsilon$ is the self energy of the vortex loop (we assume here that ε is the energy per unit length of vortex line).

The critical radius at which Eq. 3.16 has a maximum is

$$R_c = \frac{\varepsilon}{J\Phi_0} \quad (3.17)$$

as seen in Fig. 3.1. If the radius of the vortex loop is above this critical radius as in Eq. 3.17, the loop will expand towards infinity. Since the loop has a normal core, such expansion will cause dissipation of energy. The resulting free energy barrier is

$$U_c = \frac{\pi\varepsilon^2}{J\Phi_0}. \quad (3.18)$$

Vortex loops with radius larger than the critical radius R_c are produced at a rate proportional to the Boltzmann factor $e^{-\frac{U_c}{k_B T}}$. Some of these vortex loops will annihilate with loops of the opposite orientation. In equilibrium, the creation rate equals the annihilation rate and the number density of the vortex loops which cause dissipation is proportional to

$$n_f \propto e^{-\frac{U_c}{2k_B T}} = e^{-\frac{\pi\varepsilon^2}{2\Phi_0 k_B T J}} = e^{-\frac{J_T}{J}} \quad (3.19)$$

with the characteristic current scale set by thermal fluctuations given by

$$J_T = \pi\varepsilon^2/2\Phi_0 k_B T. \quad (3.20)$$

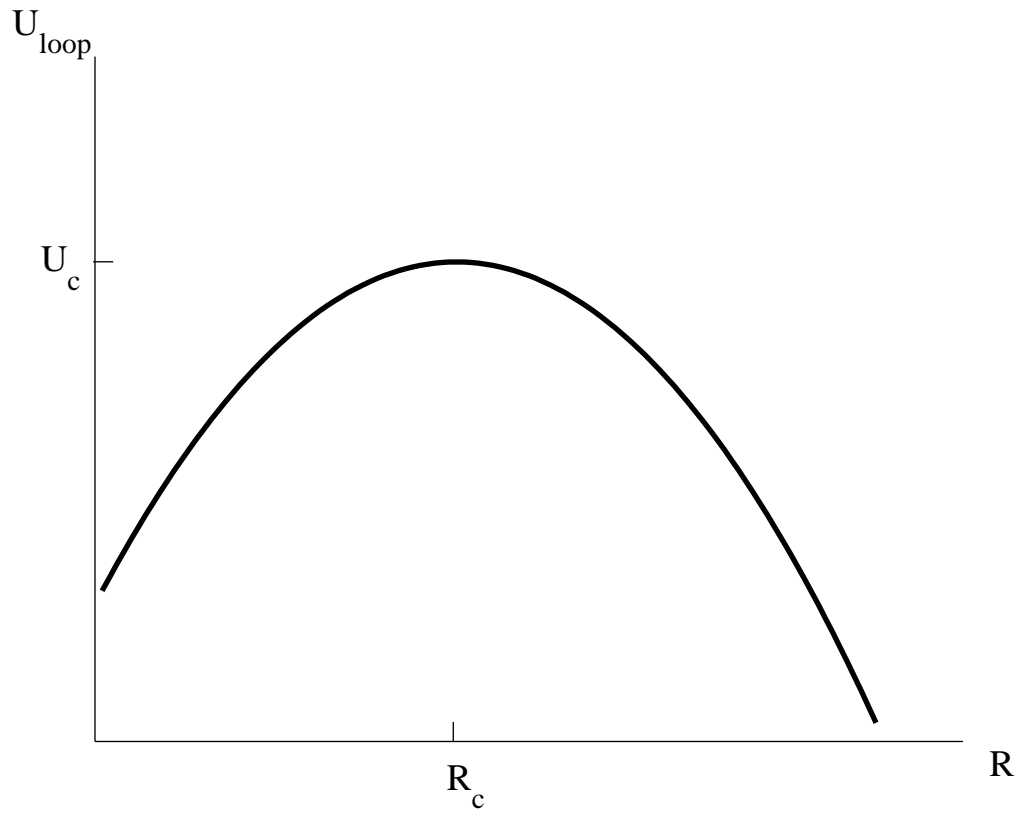


Figure 3.1: Schematic diagram of the potential barrier for vortex-loop. Vortex loops with radius less than R_c will tend to shrink while ones with radius greater than R_c will expand towards to infinity and cause dissipation.

The resistivity of the superconductor will be proportional to the number density of these excitations

$$\rho \propto e^{-\frac{J_T}{J}}. \quad (3.21)$$

3.1.3 Finite-Size Effects

In the previous section, we discussed the dissipation caused by the vortex loops unbinding in the Meissner state. The expanding of the radius of certain vortex loops to infinity causes the nonlinear behavior of E vs. J but the resistivity still converges to 0 as $J \rightarrow 0$. In reality, samples have finite sizes. Thus, there is always a cut off in the expansion of vortex loops. We will show that, because of the finite size effects, below a crossover current density, the samples (especially films) have finite linear resistance even below T_c . Finite size effects, neglected by much earlier work, can cause misinterpretations of the experimental data.

Dekker *et al.* [47] observed the crossover from the critical scaling behavior to an ohmic resistance at low currents near the 3D phase transition from normal to vortex-glass phase as well as for the transition into the Meissner phase. They argued that the crossover takes place when the growth of correlation length, $\xi_g(\xi)$, is limited by film thickness. They also made an observation that at lower field, deviation from the critical behavior is more pronounced than in higher field. However, I believe that it is not the correlation length but the vortex loop that is cut off by the thickness of the sample. In Chapter 4 I will also show that finite size effects are more pronounced in higher magnetic fields.

Woltgen *et al.* [48] studied finite-size effects in the vortex-glass transition. In their paper, they asserted that for YBCO films with thickness less than 1000 Å, the transition is obscured by the finite thickness of the sample and that for thicker samples, the finite size effects are absent. M. C. Sullivan *et al.* [50] studied the case in the zero-field transition. By studying the YBCO films with thickness up to 3000 Å, they concluded that finite-size effects are present even in the thickest sample. Both papers used the length scale proposed by FFH [12]

$$L_J = \sqrt{\frac{ck_B T}{\Phi_0 J}}. \quad (3.22)$$

This comes from Eq. 3.7, and is usually interpreted as the size of fluctuations probed in the samples with current density J . Here c is a dimensionless constant of order 1.

In our YBCO films, the length l and width w are much larger than the thickness d , so the thickness is the limiting length. According to Sullivan [17], if $d > L_J$, we are only looking at fluctuations smaller than the thickness of the film which means we are probing 3D fluctuations. On the other hand, if $d < L_J$, we probe only fluctuations that are limited in size along the c -axis. These fluctuations are 2D fluctuations. From this argument, we can determine a crossover current

$$J_{min} = \frac{ck_B T}{\Phi_0 d^2}. \quad (3.23)$$

When $J < \frac{ck_B T}{\Phi_0 d^2}$, we will expect the system to deviate from the 3D critical scaling and to become two dimensional. Experimental data [50] are consistent with a crossover current density J_{min} that has a linear relation with d^{-2} .

The argument above does not have a clear physical picture behind it. We will start with a vortex loop model and hope to better understand finite size effects. From the previous section, the critical radius of a vortex loop at current density J is $R_c = \frac{\varepsilon}{J\Phi_0}$ and the resulting free energy barrier is $F_c = \frac{\pi\varepsilon^2}{J\Phi_0}$. If we consider a typical thermal fluctuation with energy of $k_B T$, then

$$2\pi R\varepsilon = k_B T. \quad (3.24)$$

Combining Eqs. 3.17 and 3.24, we find when a typical thermal fluctuation is equal in size to the critical radius,

$$R_c^* \sim \sqrt{\frac{kT}{J\Phi_0}}. \quad (3.25)$$

Comparing Eq. 3.22 to Eq. 3.25, we arrive at a refined picture of the meaning of L_J . When J is very small, R_c is very large, and only a small number of high-energy vortex loops “blow out” because they have $R > R_c$. As J is increased, smaller and smaller loops are affected by the current. At some point, J is large enough, and R_c is small enough, that roughly half of the loops that occur due to thermal fluctuations “blow out”. At this point, currents have become a significant perturbation on the system. L_J is thus not just a length scale probed by a current, but it is the current-dependent length scale at which roughly half the thermally-generated vortex loops “blow out”. It separates a current-dominated regime from an equilibrium thermal-fluctuation dominated regime. (A more detailed discussion can be seen in Appendix A.)

This crossover occurs in bulk, but will not be observed in a thin film unless $L_J < d$, the film thickness. If $d \gg L_J$, the free energy can still be approximated by U_c

in Eq. 3.18, so we will still see the exponentially vanishing dissipation as in Eq. 3.21. However, if $d < L_J$, the cut-off vortex loops will become vortex-antivortex pairs as in Fig. 3.2(b), the resulting free energy barrier will become

$$F \approx 2d\epsilon_1 - J\Phi_0 r \quad (3.26)$$

where ϵ_1 is the energy per unit length of the vortex line and r is the spacing between the vortices. When $r > \min(d, \lambda)$, similar to the argument in Repacci [51], we will expect the ohmic response even in the “Meissner” state at low enough current density.

In conclusion, below T_c , when the applied current density J is less than J_{min} , the resistivity of the sample will change from the exponential vanishing behavior in Eq. 3.21 to a constant. Overlooking the finite-size effects will lead to incorrect determination of T_c and critical exponents.

3.2 Data and Analysis

Given a set of $I - V$ curves, each taken at a different temperature around T_c , how are we going to determine the critical exponents from the data? First, I am going to introduce the conventional analysis which has been used in previous literature. I will then show that this method can apply to the data taken from the YBCO crystals but fails when applied to the data taken from YBCO films because of finite-size effects.

Fig. 3.3 shows a schematic diagram of what is expected for the E vs. J in a double log plot. From Eq. 3.13, we expect the isotherm at T_c (the critical isotherm)

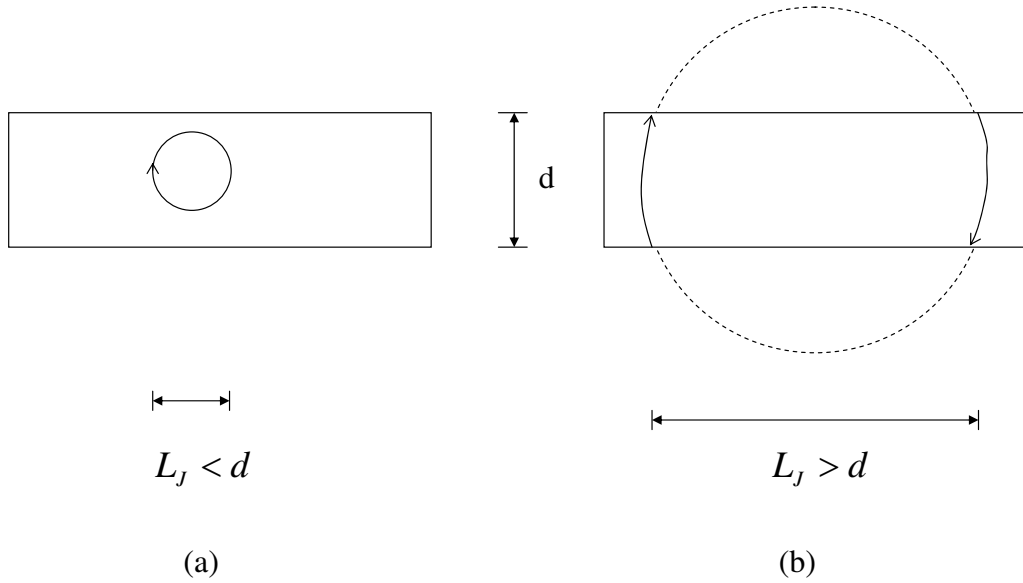


Figure 3.2: Schematic of the critical size of vortex loops with respect to the film thickness. (a) The critical size of the vortex loop is smaller than the film thickness d . We expect 3D scaling when $J > J_{min}$. (b) The critical size of the vortex loop is larger than the film thickness. We expect ohmic behavior even in the Meissner state.

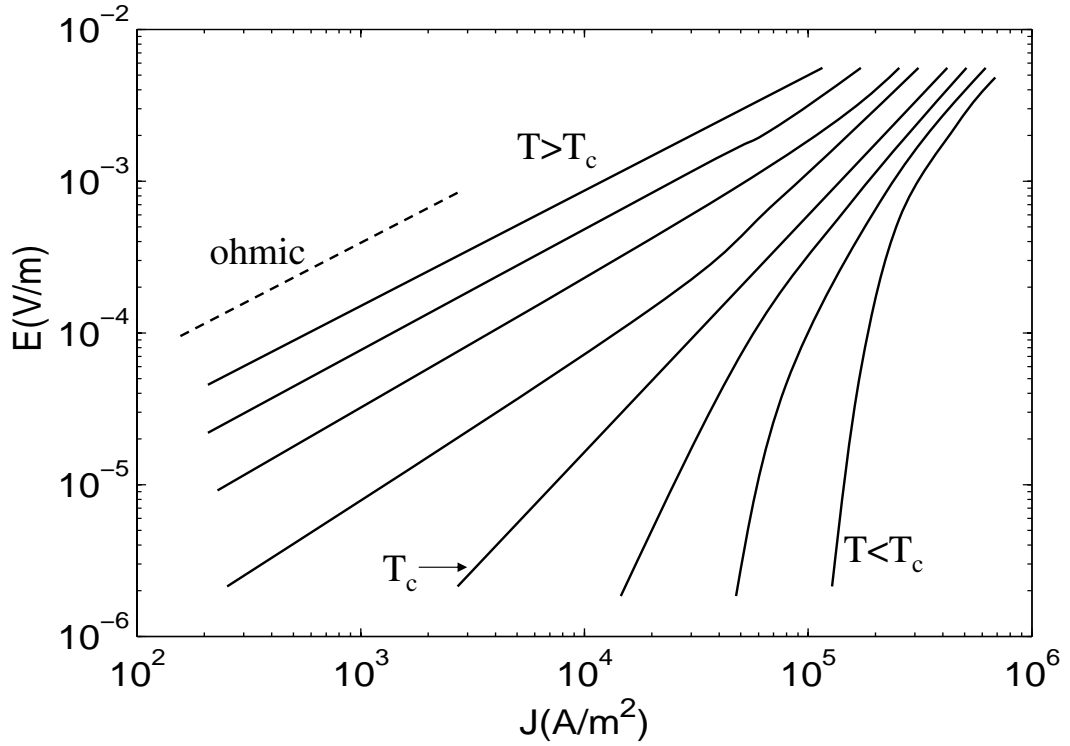


Figure 3.3: Schematic of expected $E - J$ isotherms. The dashed line indicates ohmic behavior (with the slope of 1 on a log-log plot). The isotherm at T_c is a straight line in the log-log plot with a slope of $(z + 1)/2$ for $D = 3$. Isotherms below T_c have negative curvatures illustrating the vanishing linear resistance. Isotherms above T_c have positive curvatures with nonlinear behavior at high currents and ohmic tails at low currents.

in Fig. 3.3 to be a straight line because of the power law behavior, Eq. 3.13. The slope of the critical isotherm is $\frac{z+1}{2}$ given that $D = 3$. We can thus determine z from fitting the power law behavior. Isotherms below T_c have negative curvatures illustrating the vanishing linear resistance. Isotherms above T_c have positive curvatures with nonlinear behaviors at high currents and ohmic tails at low currents. Fitting the ohmic resistance R_L as in Eq. 3.14 with $t = \frac{T-T_c}{T_c}$, we can get ν since we have determined T_c and z from the critical isotherm.

Sometimes, for real experimental data, it is difficult to determine which isotherm is closest to T_c since the data tends to be noisy at low current. The conventional analysis often chooses the first isotherm without ohmic tail as the critical isotherm. It is possible that this “critical” isotherm will have ohmic behavior at very small current density which is not observed simply because of the resolution of the experimental setup. Low frequency noise and finite size effects, which both contribute to spurious ohmic behavior at low current density, may mislead us into choosing too low a value for T_c [49, 50].

We can use another method as seen in [17, 18, 51] to determine T_c and z . This is done by taking the logarithm of Eq. 3.3 and then taking the partial derivative with respect to $\log J$

$$\left(\frac{\partial \log E}{\partial \log J}\right)_T = 1 + \frac{\partial \log \chi_{\pm}(x)}{\partial x} \frac{x}{\partial \log J}. \quad (3.27)$$

where $x = \xi^{D-1}J$. At $T = T_c$, Eq. 3.27 becomes

$$\left(\frac{\partial \log E}{\partial \log J}\right)_{T_c} = \frac{z+1}{D-1} \quad (3.28)$$

and the critical isotherm is a straight line parallel to the J axis.

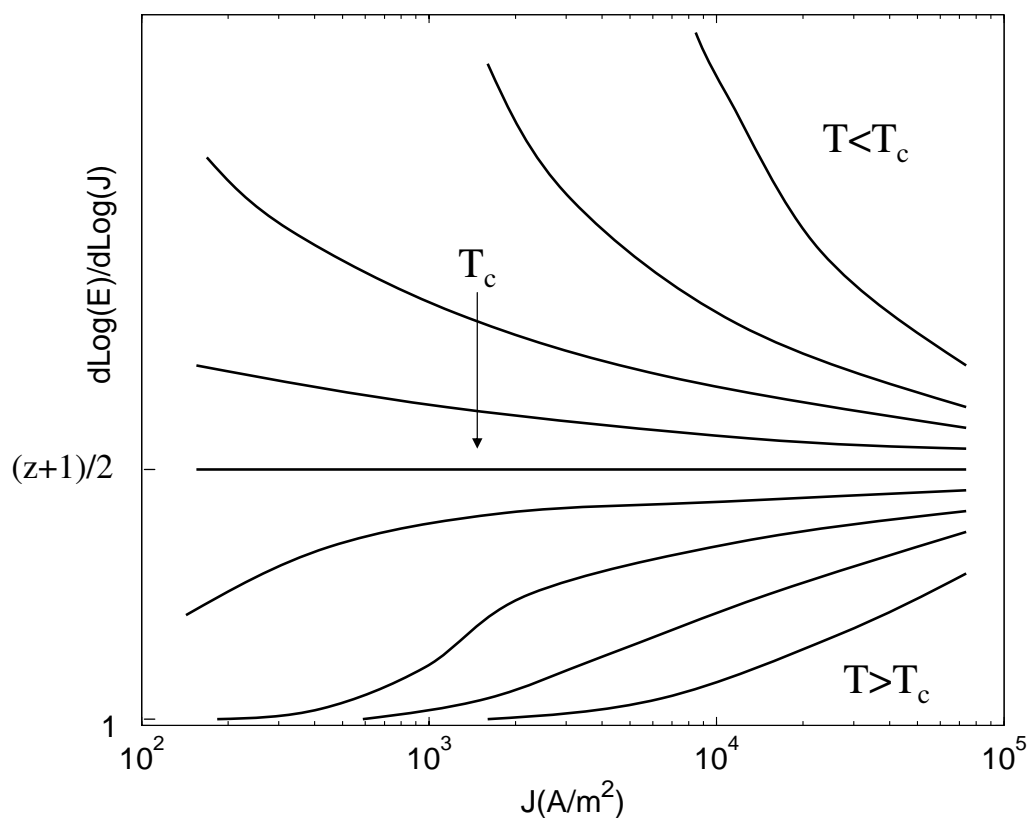


Figure 3.4: Schematic of the expected $d \log(E)/d \log(J)$ vs. J plot. The critical isotherm is a straight line parallel to the horizontal axis. Isotherms above T_c are monotonic decreasing functions while the ones below T_c are monotonic increasing.

Fig. 3.4 shows a schematic diagram of the expected $d \log(E)/d \log(J)$ vs. J . At T_c the intercept is $\frac{z+1}{2}$ which will help us determine the value of z . The isotherms above T_c are monotonically decreasing and the isotherms below T_c are monotonically increasing.

The derivative plot cannot help us find the static exponent ν , but the T_c and z determined from the derivative plot are less ambiguous than results from the

conventional analysis.

3.2.1 Crystal Data

A plot of ρ vs. T of an untwinned YBCO crystal is in Fig. 2.9 (sample C1). The applied current is along the a-axis. From the figure, the resistivity at 96 K is around $70 \mu\Omega$ and the transition temperature is estimated to be close to 93.8 K. The dimensions of the crystal are: $w = 371 \mu\text{m}$, $l = 700 \mu\text{m}$ and $d = 103 \mu\text{m}$. The sample was grown, and contacts were made using silver paint by Dr. Kouji Segawa of Central Research Institute of Electric Power Industry, Tokyo, Japan.

We first determine the critical exponents using the conventional analysis. In Fig. 3.5 we present the E vs. J curves of the crystal in double log scale. From the figure, all isotherms above the dashed line have positive curvature and have ohmic response in the limit of zero current, and all isotherms below the dashed line have negative curvature and vanishing linear resistance. We check this by fitting the E vs. J curves to a second-order form of $\log(E) = a_0 + a_1 \log(J) + a_2 [\log(J)]^2$. The coefficient a_2 can be used to measure the sign of the curvature of each isotherms. a_2 is positive above 93.839 K and negative below 93.833 K. Thus, the dashed line separates the superconducting and normal states of the sample. The power law fitting of the dashed line is $E \sim J^{1.23 \pm 0.08}$. From Eq. 3.13 (using $D = 3$), we get

$$z = 1.46 \pm 0.16. \quad (3.29)$$

In Fig. 3.6, we show the derivative plot of the data shown in Fig. 3.5. We find that the derivative plot of the crystal data looks similar to the schematic derivative

plot shown in Fig. 3.4. The dashed line we draw in Fig. 3.6 separates the two phases into the isotherms above T_c and isotherms below T_c . The isotherms below the dashed line are nearly monotonically increasing and approach 1 (ohmic behavior) at low current. The ones above the dashed line are nearly monotonically decreasing, indicating vanishing linear resistance. The intercept of the dashed line is 1.23 ± 0.1 and is expected to be $(z+1)/2$ from Eq. 3.28. Thus z determined from the derivative plot is

$$z = 1.46 \pm 0.2 \quad (3.30)$$

which is nearly identical to the result by the conventional analysis, Eq. 3.29.

We find the exponent ν from the low-current resistance

$$R_L \propto (T/T_c - 1)^{\nu(z-1)} \quad (3.31)$$

according to Eq. (3.14). We make a $\log(R_L)$ vs. $\log(T/T_c - 1)$ plot in Fig. 3.7. ν determined from this method is sensitive to the choice of T_c . If we set T_c to be 93.836 K, $\nu \approx 0.85$ from the power law fit whereas $\nu \approx 0.70$ if we set $T_c = 93.837$ K.

From FFH [12], we know that the difference between the critical temperature T_c and the first-order melting transition T_m is

$$T_c - T_g \sim H^{1/2\nu_0} \quad (3.32)$$

where ν_0 is the zero-field statical exponent. We show $T_c - T_m$ vs $\mu_0 H$ in double log scale in Fig. 3.8 and find $\nu_0 = 0.68 \pm 0.1$ from a power law fit. The result is consistent with the statical critical behavior of 3D-XY system.

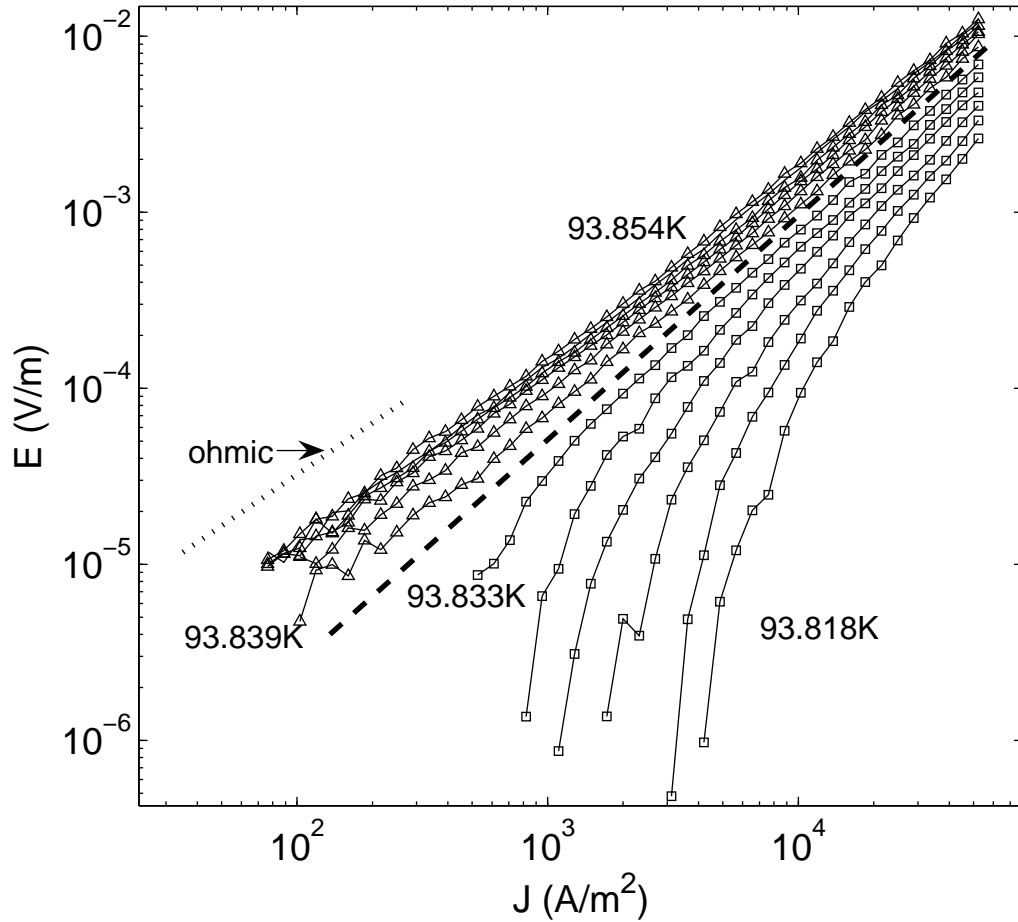


Figure 3.5: $E - J$ isotherms for a YBCO single untwinned crystal (sample C1) in zero field. The dotted line has a slope of one indicating ohmic behavior. The dashed line separates the isotherms above T_c and below T_c with opposite sign of curvatures. The isotherms with triangles and the ones with squares both have a spacing of 3 mK.

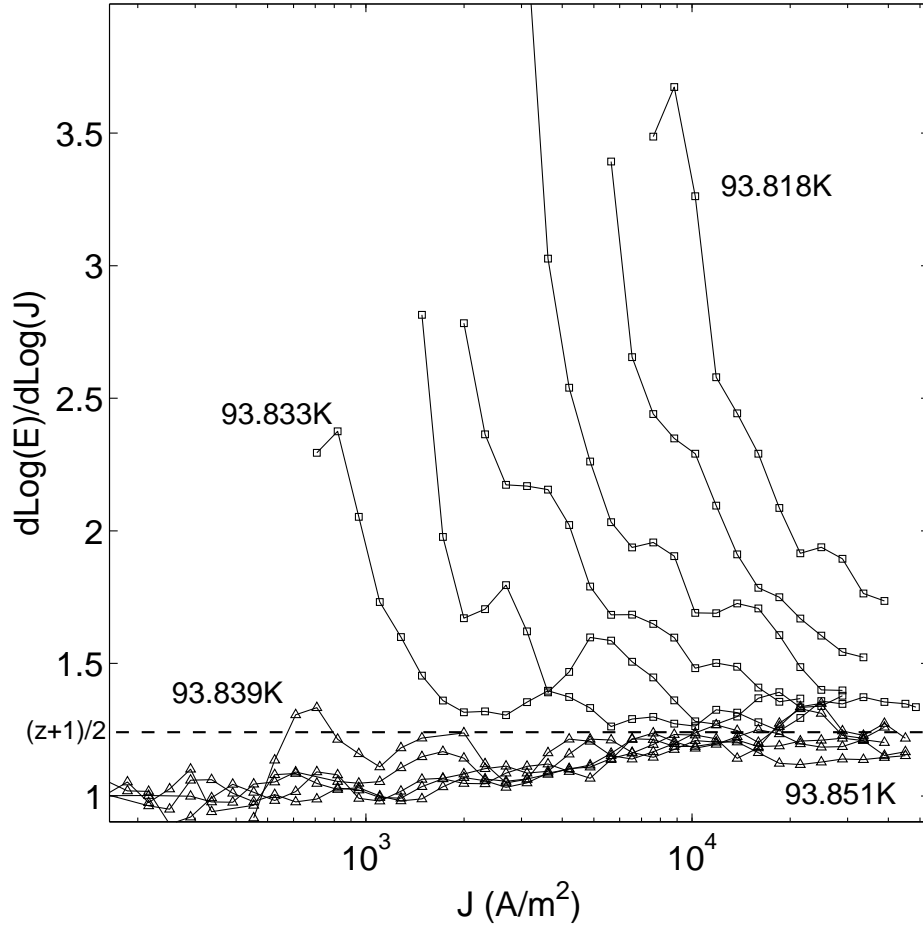


Figure 3.6: Derivative plot of the transport data from Fig. 3.5. The dashed line is drawn to separate the normal and superconducting phases. The crossing of the dashed line with isotherm of 93.839 K is due to the noise. The isotherms with triangles and the ones with squares both have a spacing of 3 mK.

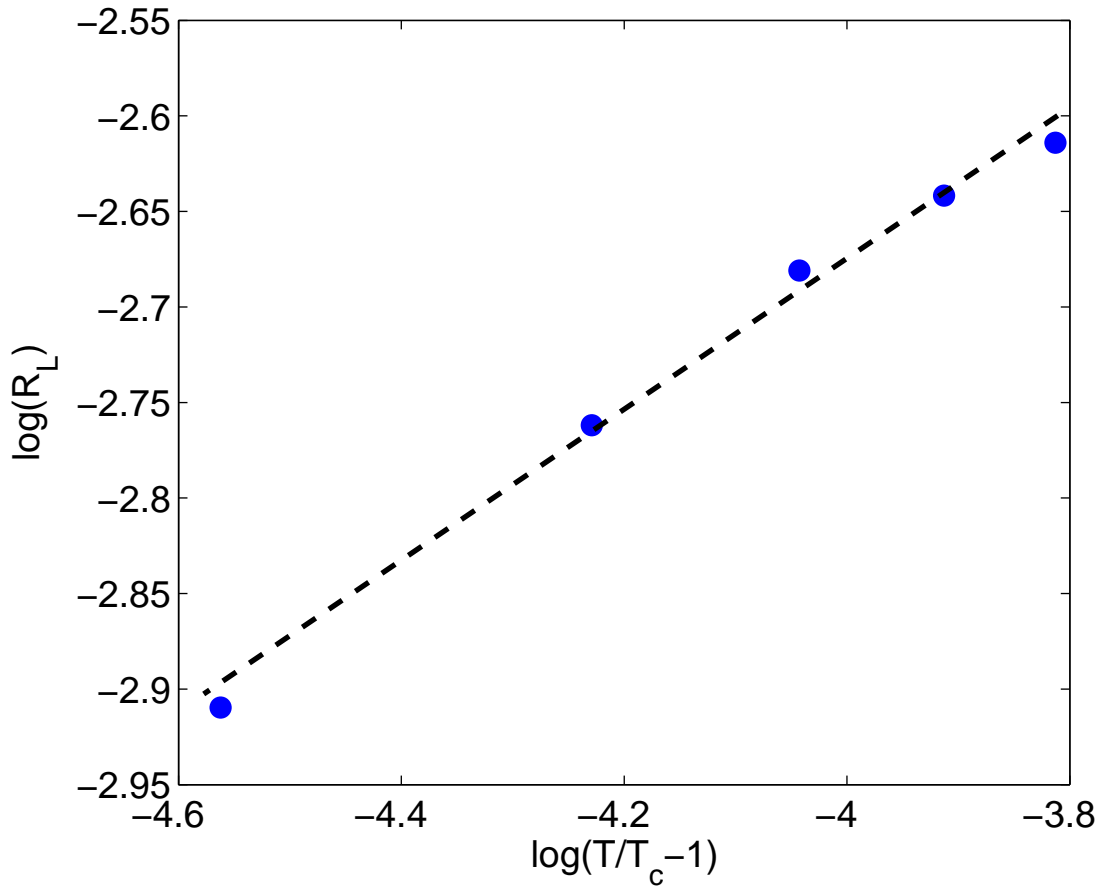


Figure 3.7: A log-log fit to Eq. 3.14 of the ohmic response of the isotherms just above the transition temperature. By setting $T_c = 93.837K$ and $z = 1.46$, we get $\nu = 0.85 \pm 0.2$.

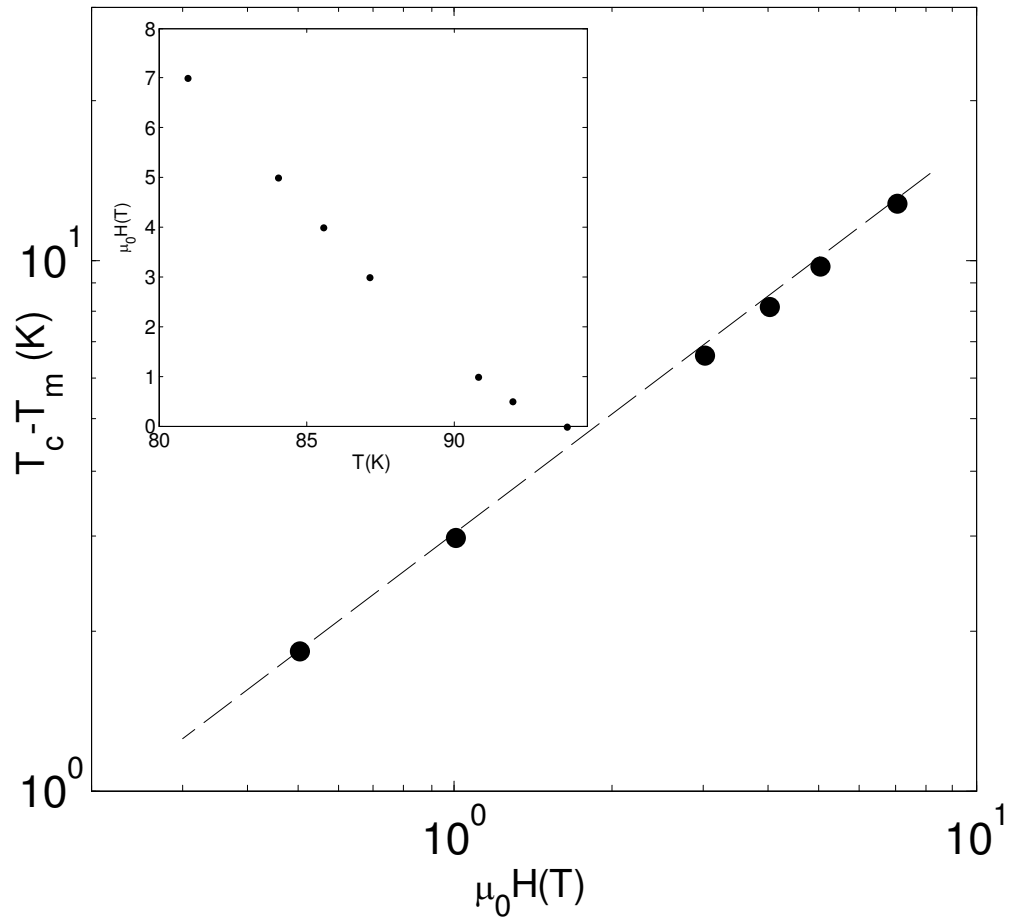


Figure 3.8: $T_c - T_m$ vs $\mu_0 H$ of an untwinned YBCO single crystal (sample C1). The insert is the melting line for the crystal up to 7 T.

3.2.2 Film Data

In Fig. 3.9, we present the E vs. J in a double-log scale of a 150 nm thick $\text{YBa}_2\text{C}_3\text{O}_{7-\delta}$ c -axis oriented optimal-doped film (sample su113). The isotherms differ by 0.05 K from 92.075 K to 91.225 K. Unlike what we did in Fig 3.5, we cannot find a single straight line in Fig. 3.9 that separates the isotherms into two groups which are either concave or convex exclusively. For example, the isotherm of 91.80K has negative curvature above 7×10^7 A/m² which means that the electric field E converges to 0 more quickly than the applied current density J . However, it has positive curvature below 7×10^7 A/m² and exhibits ohmic behavior at even lower current density.

If we were using the conventional analysis, we would choose $T_c = 91.525$ K to be the critical isotherm since it is the first isotherm that separates the isotherms with low current ohmic tails from the ones without. The power law fit of this “critical” isotherm is $E \sim J^3$ which gives the dynamic exponent $z \approx 5$. However, it is still possible that this isotherm will have ohmic behavior at lower current density and that we did not observe the ohmic response because of the resolution of the nano-voltmeter. To examine whether this candidate critical isotherm (91.525 K) has power law behavior, we can refer to the derivative plot shown in Fig. 3.10.

If the isotherm of 91.525 K is indeed the critical isotherm, it is expected to be a horizontal straight line in the derivative plot. However, in Fig. 3.10, the isotherm is monotonically decreasing above 2×10^7 A/m², and monotonically increasing below 2×10^7 A/m². So, if the experimental setup were to allow us to measure even smaller

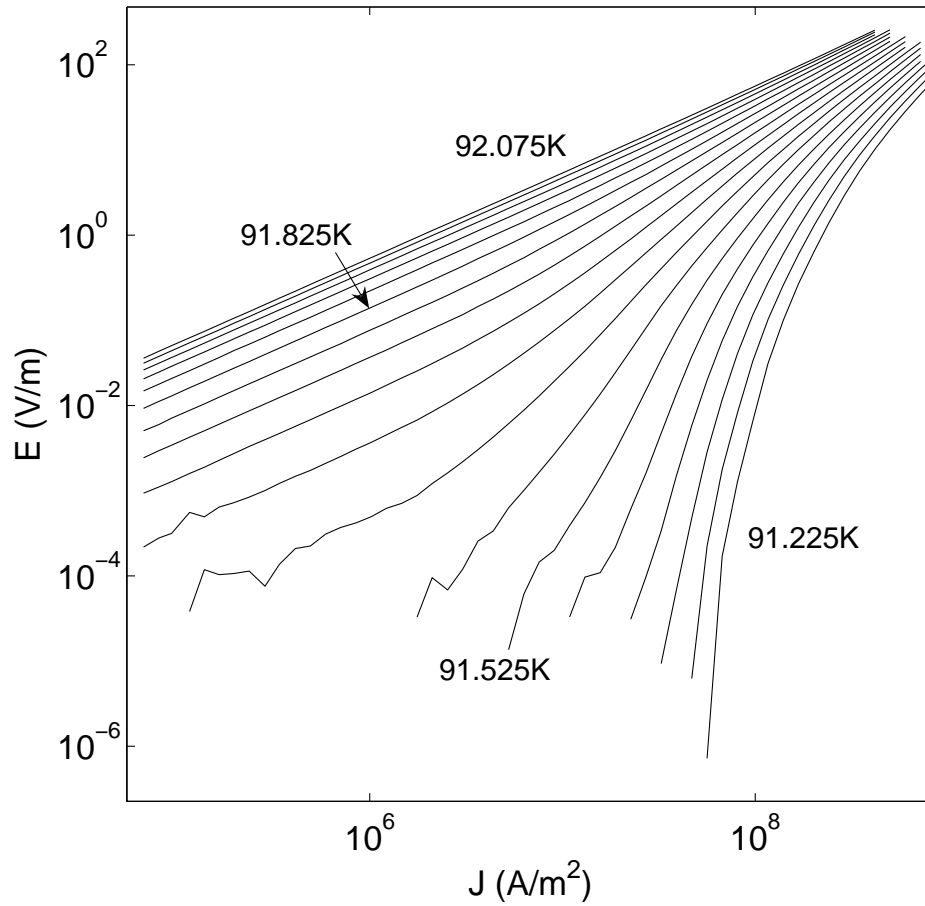


Figure 3.9: $E - J$ isotherms for a 1500 Å YBCO film in zero magnetic field. The isotherms are from 92.075 K to 91.225 K with spacing of 0.050 K.

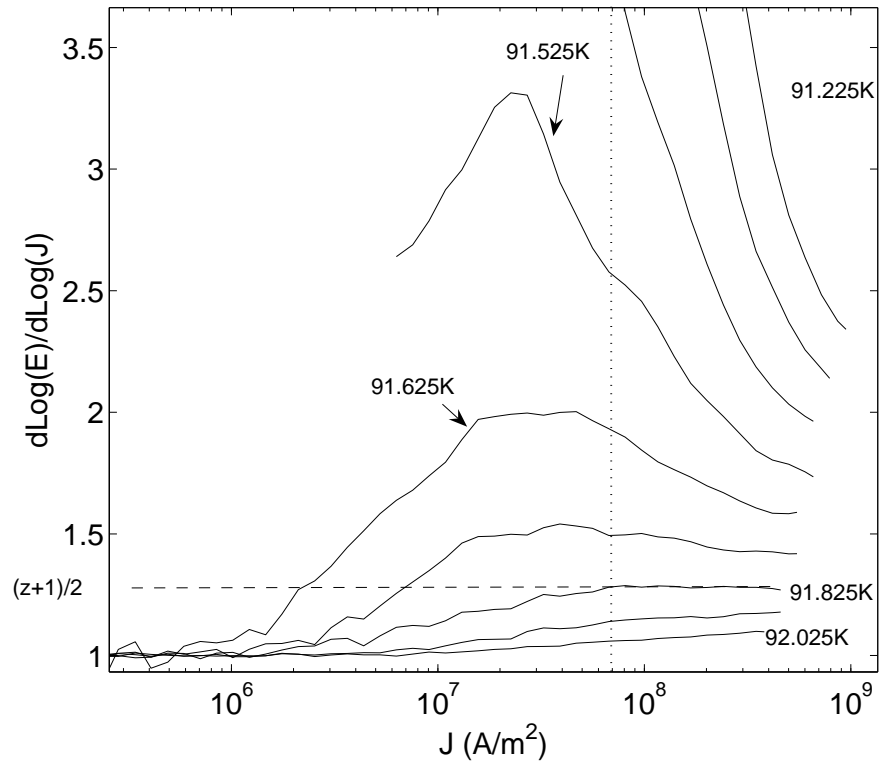


Figure 3.10: Derivative plot for a 1500 Å YBCO film (sample su113) in zero magnetic field. The isotherms are from 92.025 K to 91.275 K with spacing of 0.10 K.

voltage, we would expect the 91.525 K isotherm would bend down toward 1 (ohmic behavior) in the derivative plot at smaller current density just like the 91.625 K isotherm.

Recall that because of the finite size of the film, below a certain crossover current density, J_{min} , the film will have ohmic response even below the transition temperature T_c . The expected crossover current density J_{min} for a 1500 Å thick film is of order 10^7 A/m². From Fig. 3.10, if we only look at the data above 7×10^7 A/m² shown in Fig. 3.11, the derivative plot actually looks similar to the expected derivative plot (Fig. 3.4) from the scaling function. T_c determined from the high-current density data alone is around 91.825 K and dynamic exponent z is 1.54 ± 0.1 , which agrees with the result from the crystal data.

Because of finite-size effects, we cannot use the ohmic tails above T_c to determine the static critical exponent ν . The ohmic tails have contributions from finite-size effects and yet it is not known how to subtract such contributions. However, from FFH [12], close to T_c , similar to the case in the first-order melting transition in untwinned YBCO single crystal, the difference between the critical temperature T_c and glass transition temperature T_g has a power law relation with H as

$$T_c - T_g(H) \sim H^{1/2\nu_0} \quad (3.33)$$

where $T_g(H)$ is the vortex-glass transition temperature at H and ν_0 is the zero-field static exponent. A detailed discussion about the vortex-glass transition temperature can be found in Chapter 4.

We show $T_c - T_g(H)$ vs. H in double-log scale in Fig. 3.12. The dashed line

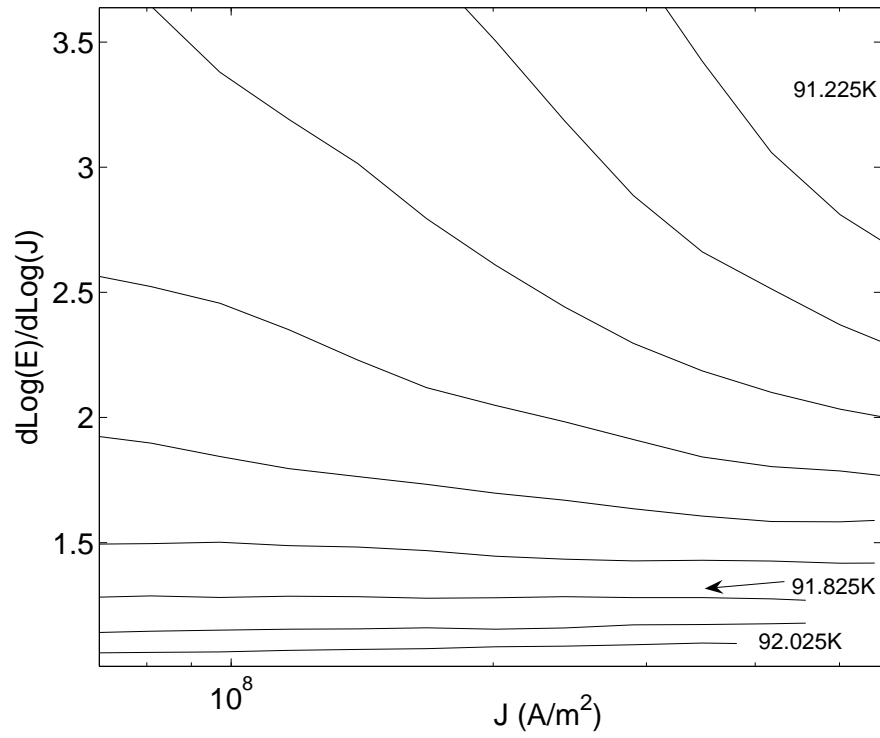


Figure 3.11: Derivative plot for a 1500 Å YBCO film (sample su113) in zero magnetic field at high-current regime. The isotherms are from 92.025 K to 91.275 K with spacing of 0.10 K. The isotherm of 91.825 K is very nearly horizontal with an intercept of 1.27.

is a power law fit to the data with a slope of around 0.81. Combined with Eq. 3.33 gives

$$\nu_0 = 0.62 \pm 0.1. \quad (3.34)$$

Finally, we have found consistent values for both exponents z and ν from crystals' data and films' data. The results show that the zero-field transition for YBCO is 3D-XY like and has a model-E dynamics.

3.2.3 Discussion

Normal channel subtraction

In the previous data analysis by Strachan [53] and Sullivan [17], the current density J used in the scaling function Eq. 3.3 is not the applied current density. Instead, they used the so-called fluctuating current density ΔJ . The ΔJ is associated with the fluctuation-enhanced conductivity $\Delta\sigma$ in the form

$$\Delta J = \Delta\sigma E. \quad (3.35)$$

The idea of fluctuation-enhanced conductivity actually comes from Gaussian fluctuations [6] (fluctuations as perturbations). Above the mean-field transition temperature T_{c0} , fluctuation-enhanced conductivity is expected to add to the conductivity due to the electrons in the normal state as shown in Fig. 3.13.

The applied current density J can be written as

$$J = \sigma E = \sigma_n E + \Delta\sigma E \quad (3.36)$$

where σ_n is the conductivity due to the normal background and $\sigma = \sigma_n + \Delta\sigma$ is the

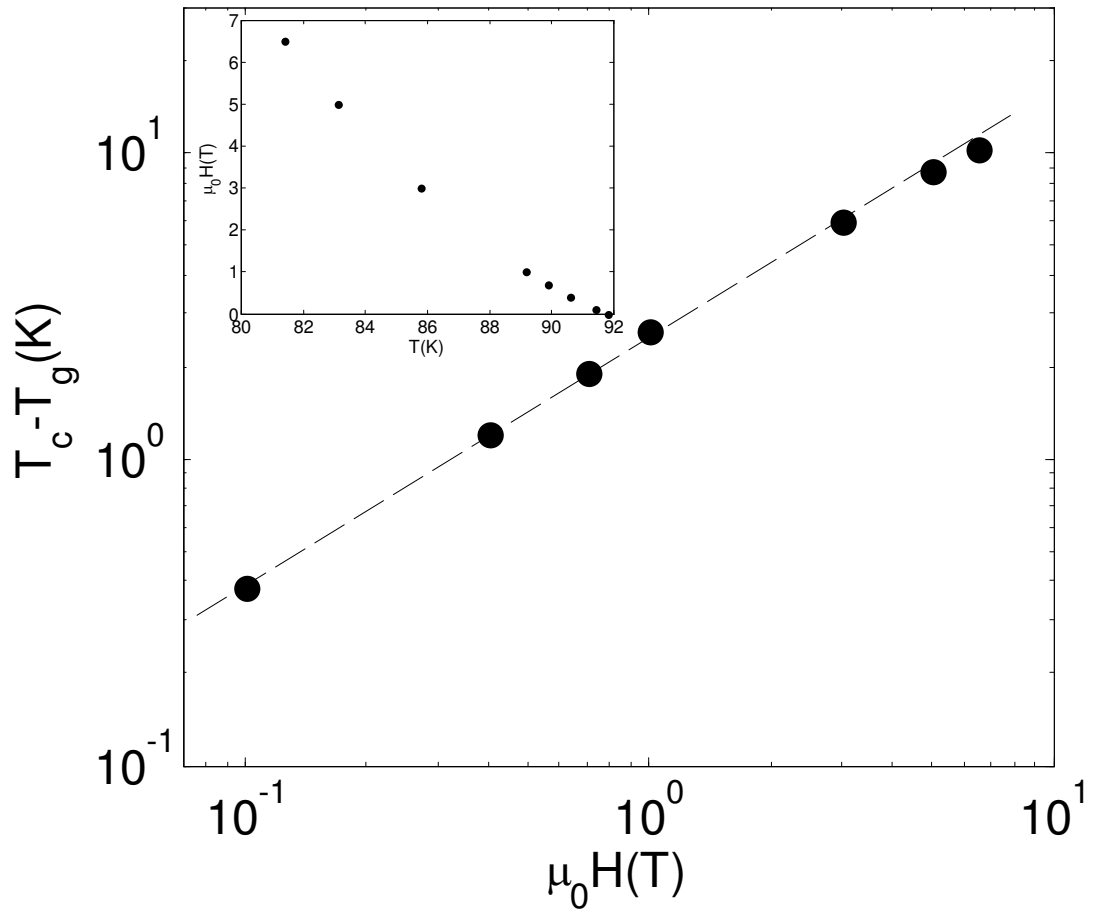


Figure 3.12: $T_c - T_g$ vs. H in double-log scale of a YBCO thin film (sample su113).

The insert is the melting line for the film up to 6.5 T.

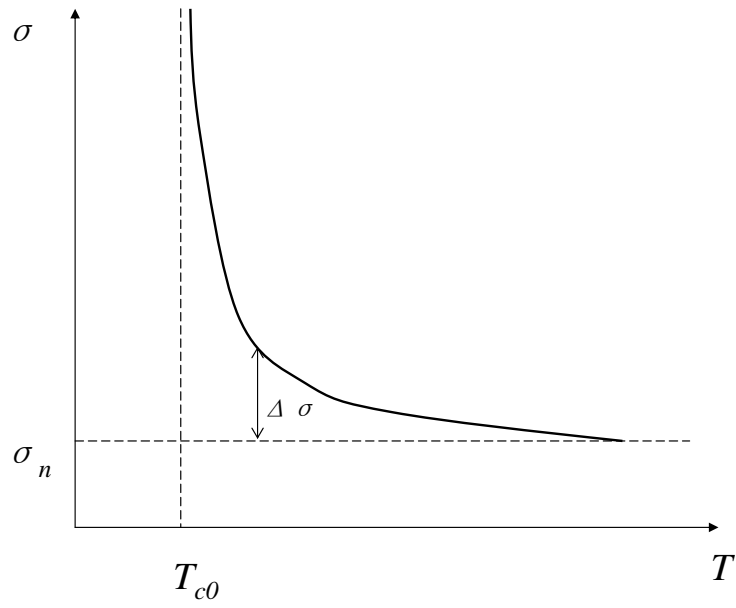


Figure 3.13: The solid line represents the predicted conductivity with Gaussian fluctuations. σ_n is the normal state conductivity and $\Delta\sigma$ is the fluctuation-enhanced conductivity.

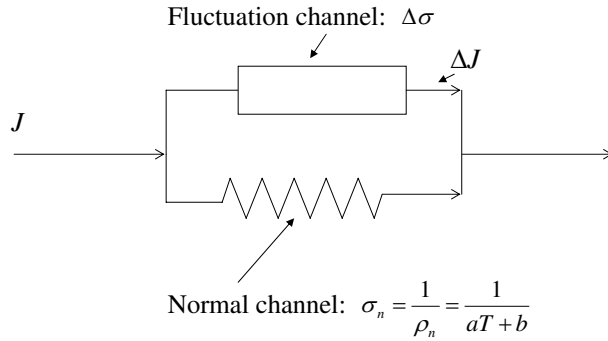


Figure 3.14: In the two-channel model, current is assumed to flow through the two parallel channels, the fluctuating channel and normal channel.

overall conductivity. Thus, fluctuating electrons and the normal electrons are two different parallel channels for the current to flow through, as shown in Fig. 3.2.3.

The normal channel is assumed to be just a simple resistor, the resistivity of which is assumed to be linear in T . The resistivity of the YBCO crystal (sample C1) ρ vs. T is shown in Fig. 3.15. The dotted line is the linear fit to the normal state resistivity above 140 K, $\rho_n(T) = aT + b$. The current through the fluctuation channel can be found

$$\Delta J = J - \frac{E}{aT + b}. \quad (3.37)$$

The question naturally arises, is it valid to subtract the normal background *below* T_c ? First, We don't see any reason to subtract the normal channel below T_c ,

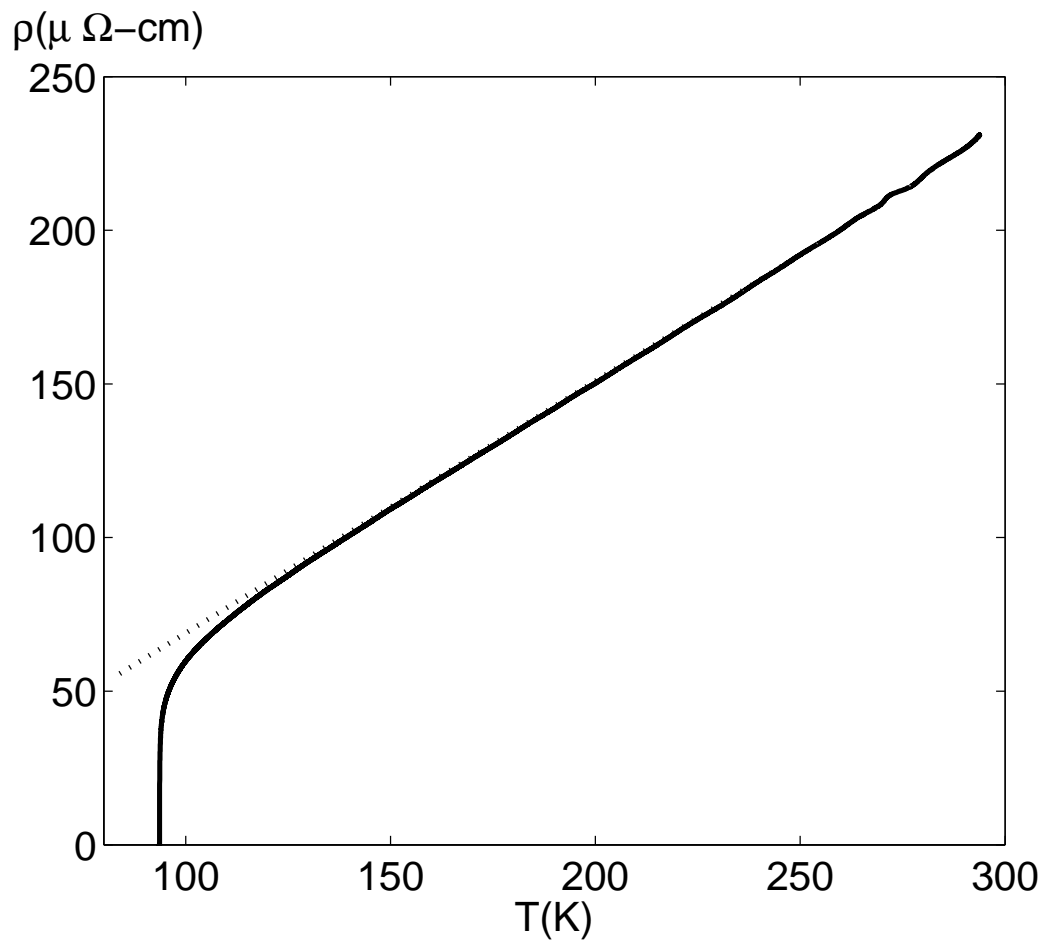


Figure 3.15: The solid curve is the ρ vs. T of untwinned single YBCO crystal (sample C1). The dotted line is the normal background which is the linear fitting of the solid curve above 140 K.

since the linear resistance of the sample below T_c is expected to vanish. Second, subtracting the normal background is appropriate for Gaussian fluctuation ([6]), but not justified in the critical region. From the FFH's derivation [12] of the scaling function 3.3, the current density is specified as applied current density J , not the ΔJ flowing through the fluctuation channel. Last, from Fig. 3.13, at or below the mean field transition temperature T_{c0} , the resistivity is strictly zero which is contrary to the behavior predicted by Eq. 3.3 and the experimental data: $\rho \rightarrow 0$, as $J \rightarrow 0$.

Fig. 3.16 shows E vs. J and E vs. ΔJ of a YBCO film (sample su113). The dotted curves are the isotherms with ΔJ and the solid curves are the isotherms with J . From the figure, below 91.825 K and at low current density, the dotted isotherms almost coincide with the solid isotherms since $\frac{E}{\rho_n}$ is a small term compared with $J = \frac{E}{\rho}$ when $\rho_n \gg \rho$ at lower T and lower current density J . At higher current density or higher temperature, deviations between the two sets of isotherms are observed since ρ_n and ρ are comparable at higher T or higher J . The sharp upturn at high ΔJ of the dotted isotherms greatly distorts the power law behavior and can not be explained by heating alone. The derivative analysis, $\frac{\partial \log(E)}{\partial \log(\Delta J)}$ vs. ΔJ gives us $T_c = 91.775$ K and $z = 2.3 \pm 0.2$ (Model A dynamics) whereas $\frac{\partial \log(E)}{\partial \log(J)}$ gives us $T_c = 91.825$ K and $z = 1.5 \pm 0.2$ (Model E dynamics).

To explain why two sets of isotherms give such different results, we compare the isotherms at $T = 91.775$ K as shown in Fig. 3.17. At $J > 5 \times 10^7 A/m^2$, where there are no finite size effects present, the E vs. J shows downward curvature which illustrates the vanishing linear resistance. This implies that this isotherm is actually below the transition temperature T_c and in the superconducting state. However, the

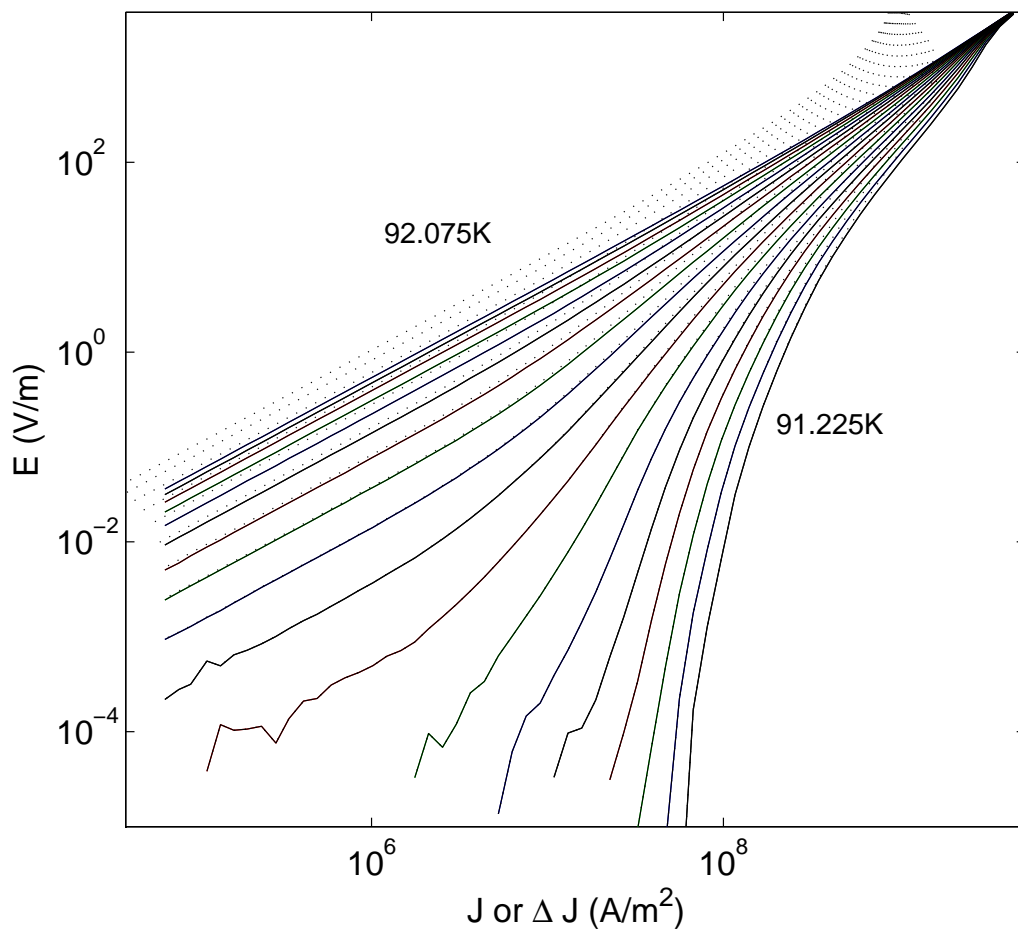


Figure 3.16: E vs. J (solid curves) and E vs. ΔJ (dotted curves) of a YBCO film (sample su113) on the same plot. The separation of each isotherm is 0.50 K

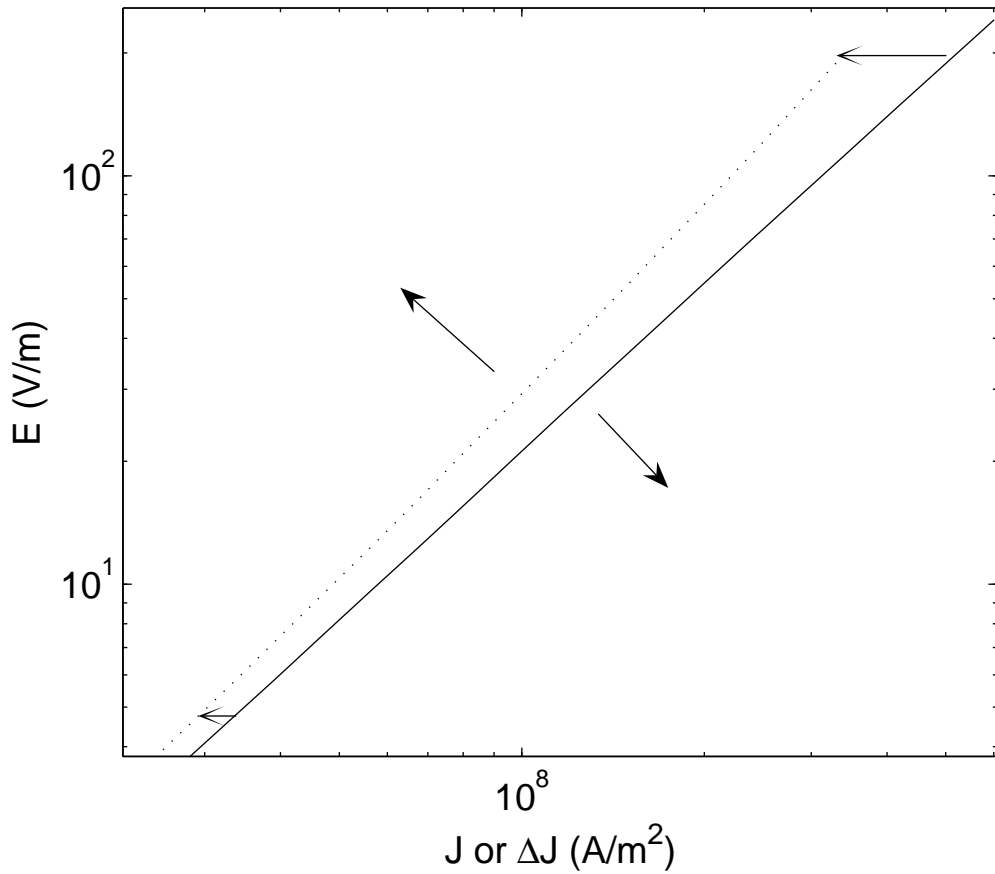


Figure 3.17: The solid curve is E vs. J of the 91.775 K isotherm with negative curvature at high current density. The dotted curve is E vs. ΔJ with positive curvature.

E vs. ΔJ shows upward curvature which can mislead us by saying that this isotherm (91.775 K) is still in the normal state. The explanation of the changing of the sign of the curvature is that the deviation is larger at higher current density than the deviation at lower current density as seen in Fig. 3.17 of the two horizontal arrows. Thus, T_c determined from E vs. ΔJ will be lower and the corresponding dynamic exponent z will be higher.

In Fig. 3.18, we present E vs. J and E vs. ΔJ of the YBCO crystal (sample C1) in the same plot. The dotted curves are the isotherms with ΔJ and the solid curves are the isotherms with J . At low current density, the dotted isotherms almost collapse with the solid isotherms. At higher current density, we notice that there are only small deviations between the dotted isotherms and solid isotherms. By doing the conventional analysis, T_c values determined from both two sets of isotherms are essentially the same. The dynamic exponent z determined from the E vs. ΔJ is 1.7 ± 0.3 where as z determined from E vs. J is 1.5 ± 0.2 . This is because although subtracting the normal background can change the power law behavior at high current density, it does not create or eliminate ohmic tails at low current density.

Heating

Heating can be a very big problem in our experiment. At low enough applied current, the effect of heating is negligible and the sample will be at a fixed temperature T_0 . However, at high applied current, the sample will be heated to $T_1 = T_0 + \Delta T$. The voltage across the sample is $V(I, T_1)$ instead of $V(I, T_0)$ and $V(I, T_1) > V(I, T_0)$. Thus, the heating of the sample at high current density can create extra nonlinear behavior and distort the shape of the $I - V$ curves. This

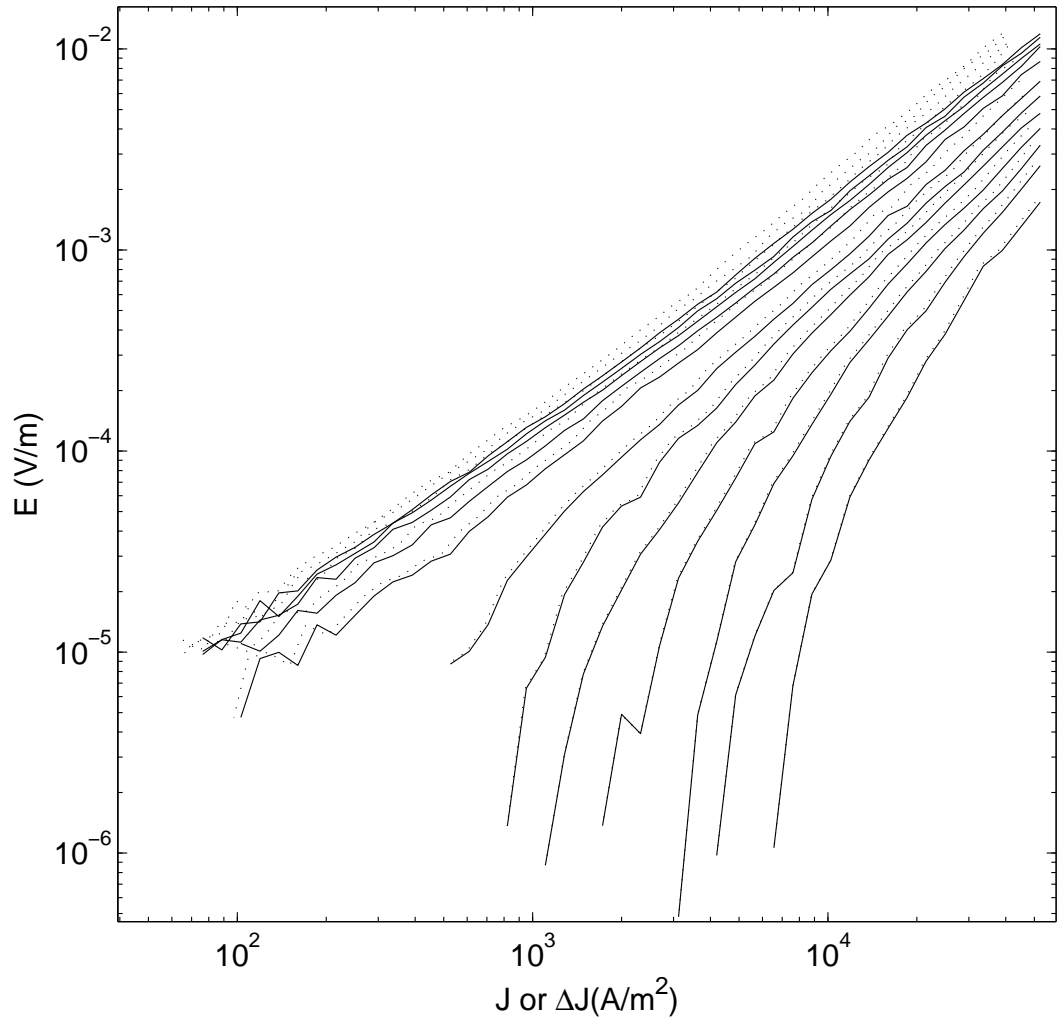


Figure 3.18: The solid isotherms are E vs. J of YBCO crystal (sample C1) and the dotted isotherms are E vs. ΔJ .

can give misleading results since we determine the dynamic exponent z from the high-current data.

Strachan [18] has systematically discussed the effect of heating of the sample. Strachan divided the sources of heating into two categories: heating from the sample itself and heating from contacts. He also found ways to quantify the rise of temperature due to heating.

Sullivan revisited the problem in [17] in which he found that for a typical 2000 Å film, at 1 mA, the leads and contacts dissipate a power of order 10^{-8} W, three orders of magnitude less than the power generated in the self-heating of the bridge. So the heating generated from the leads and contacts is negligible compared to the self-heating of the sample.

When the current is flowing through the sample, it can create heat, the power of which is given by $P = IV$ where V is the voltage across the sample. This power will raise the sample's temperature from T_0 to $T_0 + \Delta T$. Remember that in the scaling function Eq. 3.3, the scaling variables are E and J . So it is the relation between E and J that we are interested in, not the V and I . We wish to study how the geometry of the pattern affects heating while keep E and J fixed.

The possible sources of thermal gradients are the YBCO/substrate interface, the leads/bridge interface and the substrate/copper-block interface. First, let us consider the case that the thermal gradients are at the YBCO/substrate interface. The power P generated by the current is

$$P = VI = (EJ)lwd \tag{3.38}$$

where l is the length, w is the width and d is the thickness of the bridge. Assuming for simplicity that the sample temperature does not depend on position, the heat flowing out of the sample into the substrate is given by

$$P \approx G_1 \Delta T_1 \quad (3.39)$$

where G_1 is an interface conductance, related to an interface thermal conductivity κ_1 by

$$G_1 = \kappa_1 l w. \quad (3.40)$$

Combining Eqs. 3.38 through 3.40 yields

$$\Delta T_1 \approx \frac{E J d}{\kappa_1} \propto d \quad (3.41)$$

which is proportional to the thickness of the film. We cannot reduce the effect of heating, in this case, by changing the length and width of the bridge for fixed E , J and d .

Second, if we assume that most of the thermal gradients are located at the leads/bridge interface, then the thermal conductance $G_2 = \kappa_2 w d$. The temperature rise ΔT_2 due to κ_2 is then

$$\Delta T_2 \approx \frac{E J l}{\kappa_2} \propto l \quad (3.42)$$

In this case, we can reduce the self-heating of the sample by reducing the length of the bridge l while keeping E and J fixed.

At last, in the extreme case, if we assume that most of the thermal gradients are located at the substrate/copper-block interface, then the thermal conductance is independent of the dimensions of the bridge. The temperature rise ΔT_3 due to

the substrate/copper-block conductance, is

$$\Delta T_3 \approx \frac{P}{G_3} \propto lw \quad (3.43)$$

which is proportional to the product of the length and the width of the bridge. In this case, we can reduce the self-heating of the sample by reducing the length and width of the bridge simultaneously while keeping E and J fixed.

In reality, the effect of the self-heating is more complex and the temperature rise may be a combination of ΔT_1 , ΔT_2 and ΔT_3 . To show how the geometrical difference of the bridges can affect the self-heating of the sample, we present a comparison of the derivative plots of two different bridges as seen in Fig. 3.19. Both bridges ($20 \times 100 \mu\text{m}^2$ and $100 \times 500 \mu\text{m}^2$) are in the same YBCO film and in series with each other.

From Eqs. 3.42 and 3.43, the temperature rise on the $100 \times 500 \mu\text{m}^2$ bridge should be at least 5 times larger the one on the $20 \times 100 \mu\text{m}^2$ bridge at the same current density J assuming $\kappa_1 \gg \kappa_2, \kappa_3$. In the low current density regime, we see that the two sets of isotherms overlap with each other since heating is negligible at low current densities. In the high current densities, more heating in the $100 \times 500 \mu\text{m}^2$ bridge makes the isotherms (dotted curves) deviate from the solid curves. A rough estimate of the difference in temperatures of the two sets of isotherms in the high current density regime is 60 mK to 120 mK around $8 \times 10^7 \text{ A/m}^2$.

Since we are using the high current density data to determine the transition temperature T_c and dynamic exponent z of the YBCO films, failure to account for the higher heating effect on longer or wider bridges may give us misleading results.

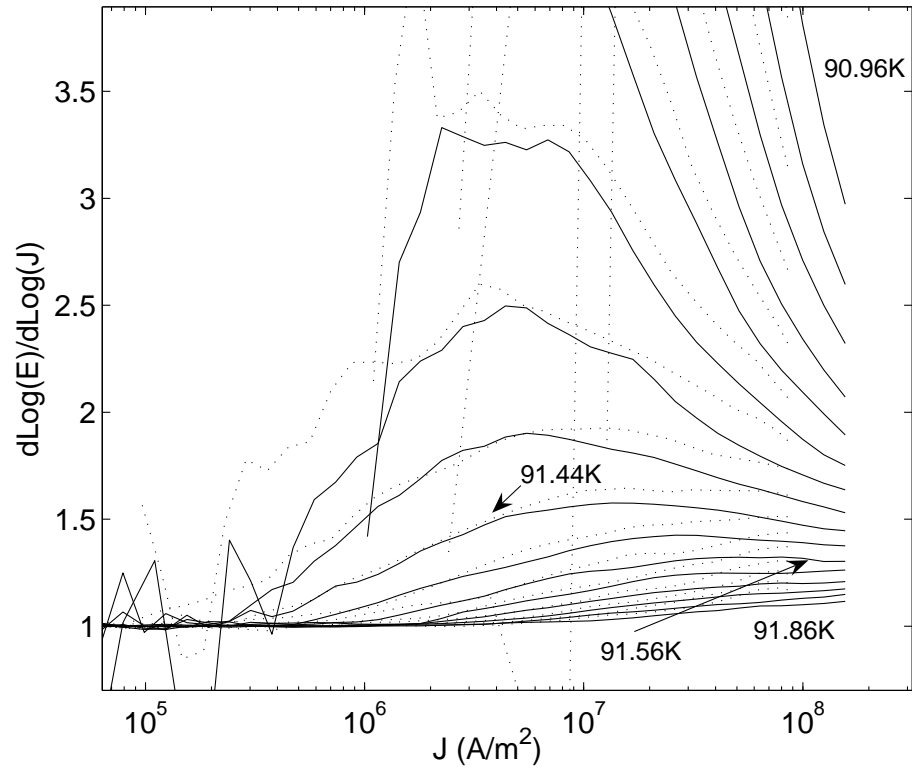


Figure 3.19: Comparison of the derivative plots of two different bridges in the same YBCO film. The set of solid isotherms is from the $20 \times 100 \mu\text{m}^2$ bridge and the set of dotted isotherms is from $100 \times 500 \mu\text{m}^2$ bridge. The spacing between the isotherms is 60 mK.

For instance, from Fig. 3.19, T_c and z determined from the data from $20 \times 100 \mu\text{m}^2$ bridge (sample mcs146) are 91.56 K and 1.6 respectively. Heating bends the curves up at high current densities; for the data from the $100 \times 500 \mu\text{m}^2$ bridge (sample mcs146) this makes us choose a lower $T_c = 91.62$ K and a larger $z = 2.2$.

Strachan [18] and Sullivan [17] have quantified the rise of the temperature for the $8 \times 40 \mu\text{m}^2$ bridge in a 2000 \AA thick YBCO film to be less than 10 mK at 10^8 A/m^2 much less than the spacing of the isotherms. Since most of the bridges I made are of this dimension, we are safe to determine T_c and z from the data on those bridges in the high current density regime which is less than 10^8 A/m^2 .

We now turn to heating effects in the YBCO crystals. Unlike YBCO films, which have good thermal conductivity between the YBCO and substrate, the YBCO crystals are not well thermally linked with the sapphire beneath them. Besides, the spacing between the isotherms of crystal data is usually several milikelvin, compared with 50 milikelvin in the films, and heating which can only causes the crystal to deviate a few milikelvin from the base temperature can give misleading results.

To reduce the heating effect of the crystal, we can use the exchange gas method. We fill the inner can with helium gas. The inner can temperature is set at the same temperature as the sample. The power generated from the current can thus be dissipated through the helium gas. In Fig. 3.20, we present a comparison of the E vs. J plots between the YBCO crystal data taken with and without exchange gas. Larger heating effects are observed for the data without exchange gas at high current density regime. Although the deviation is only 6 mK, dynamic exponent z determined from the data without exchange gas is 1.8, compared to $z = 1.5$

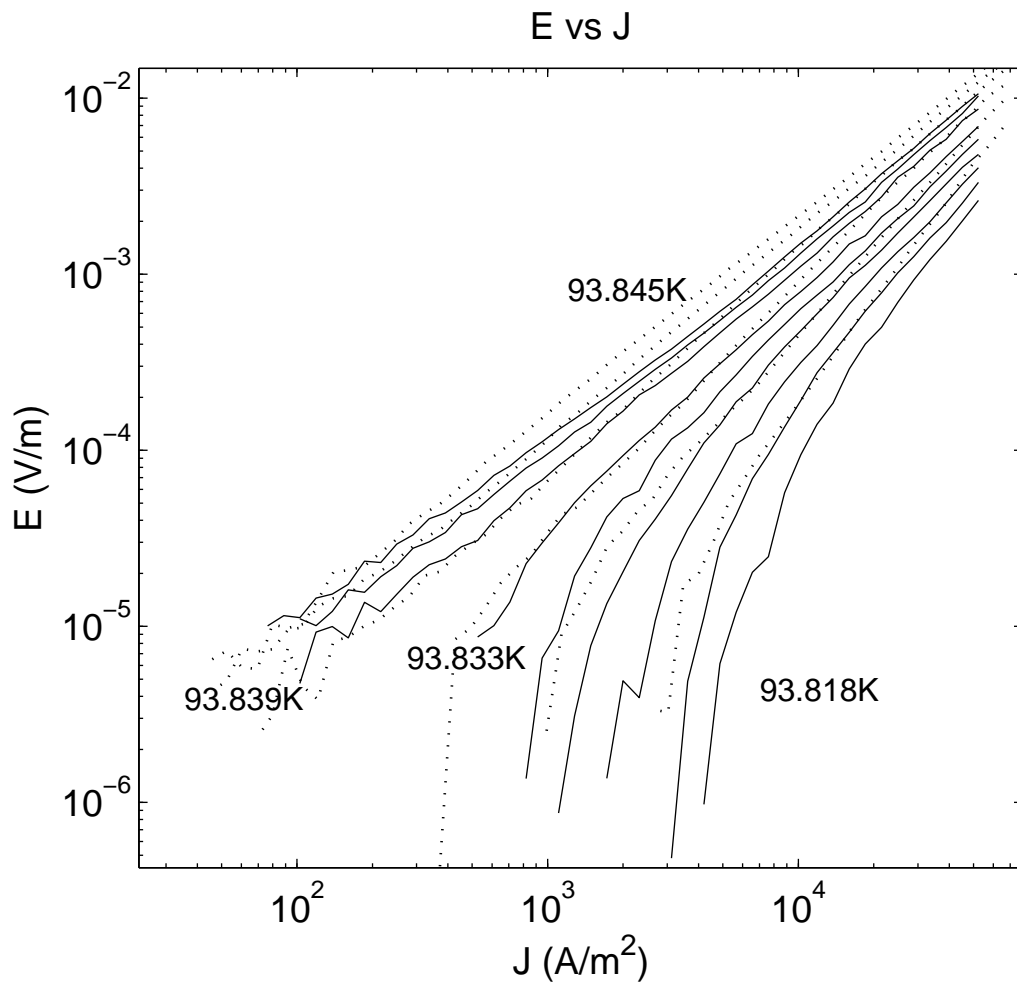


Figure 3.20: Comparison of the E vs. J between the data from a YBCO crystal with and without exchange gas. The solid curves represent the data taken with exchange gas while the dotted curves represent the data taken without exchange gas.

determined from the one with exchange gas.

Chapter 4

The Superconducting Phase Transition of YBCO in Magnetic Field

4.1 Vortex-Glass Phase Transition

So far we have discussed the topic of the phase transition of the high-temperature superconductors in zero magnetic field. Now we discuss the phase transition in non-zero magnetic field. Before the discovery of the high-temperature superconductors, it was generally believed that there is no phase transition in a magnetic field. The Anderson-Kim theory of “flux creep” [11] proposed that thermal fluctuation can allow flux motion even when pinning exists. The result is the existence of finite resistance $\rho \sim e^{-\frac{U}{T}}$ with U being the activation energy at all temperatures at fields larger than H_{c1} even in the limit of zero current.

After the discovery of high-temperature superconductors, it was first believed that there is flux-creep. The early experimental data on $\text{Bi}_{2.2}\text{Sr}_2\text{Ca}_{0.8}\text{Cu}_2\text{O}_{8+\delta}$ crystals [55] and $\text{YBa}_2\text{Cu}_3\text{O}_{7-\delta}$ films [56] showed flux-creep related phenomenon. In [55], Palstra *et al.* found a current-independent resistance which is thermally activated and can be described by an Arrhenius law, $\rho = \rho_0 \exp(-U_0/T)$ in the mixed state. In [56], Zeldov *et al.* found a current-dependent thermally activated electrical resistivity of the YBCO films in the mixed state in the form of $\rho = \rho_0 \exp(-U/T)$

where the activation energy U scaled with current density as $\ln(J_0/J)$.

In contrast, FFH [12] proposed a true superconducting state in field in which vortex flow is impeded due to random pinning or other imperfections in the material. Their argument [12] is that the introduction of random pinning will destroy the crystalline long-range order of the vortex lattice phase [57]. A vortex-glass phase will appear to replace the vortex-lattice phase with vanishing linear resistivity in the limit of zero current and long-range phase coherence. In the vortex-glass phase, the material is in a true superconducting state. The name vortex-glass comes from an analogy to the long-range order in spin glasses [58].

A phase diagram containing a vortex-glass phase is shown in Fig. 1.4. The lower critical field of $H_{c1}(T)$ separates the Meissner phase and the vortex-glass phase. The upper critical field $H_{c2}(T)$ is no longer a coexistence curve for the phase transition; there is instead a broad crossover from the normal phase to the vortex-liquid phase. There is a continuous phase transition, called the vortex-glass phase transition, between the vortex-liquid phase and the vortex-glass phase. The phase coexistence curve is $H_g(T)$ ($H_{c1} < H_g < H_{c2}$).

Similar to the phase transition in zero field, the vortex-glass phase transition has a diverging correlation length at T_g (transition temperature of the vortex-glass transition)

$$\xi_g \sim |T - T_g|^{-\nu} \quad (4.1)$$

and a diverging relaxation time (critical slowing down)

$$\tau_g \sim \xi_g^z. \quad (4.2)$$

Since the vortex-glass phase transition is second order, the scaling form Eq. 3.10 we discussed in Chapter 3 should also apply here, with substitutions of the vortex-glass correlation length, critical exponents and scaling functions. Thus the expected scaling form for a vortex-glass transition can be written as

$$\frac{E}{J} = \xi_g^{D-2-z} \chi_{\pm}(J\xi_g^{D-1}) \quad (4.3)$$

where χ_{\pm} are two universal functions which characterize the system above (+) and below (−) the glass transition temperature.

At the vortex-glass transition temperature, we still expect a power law $E - J$ curve

$$E \sim J^{(z+1)/(D-1)}. \quad (4.4)$$

For T near T_g , the $E - J$ characteristics should approach this power law behavior at high current densities, crossing over to ohmic behavior at low current densities for $T > T_g$ as

$$R_L \sim \xi_g^{(D-2-z)}, \quad (4.5)$$

and to an exponentially vanishing resistance for $T < T_g$.

The dynamic exponent z estimated in FFH [12] ranges from 4 to 7 since it is expected by FFH that it should be larger than the $z = 4$ for the 6D conventional spin glass and smaller than the $z = 6 \pm 1$ for the 3D Ising spin glass. Monto Carlo simulations of the gauge glass model in 3D by Olson *et al.* [59] give the dynamic exponent $z = 4.2 \pm 0.6$ and the correlation length exponent $\nu = 1.39 \pm 0.2$. Later data simulations by Vestegren [60] on a vortex-glass transition by a random pinning model give interesting values of $\nu = 0.7$ and $z = 1.5$, very close to those of the zero-

field 3D-XY model with model-E dynamics. Lidmar [61] studied a model describing vortices in strongly disordered 3D superconductors and found $\nu \approx 1.3$.

Clearly, there is no agreement on the exponents from simulation results. What happened on the experimental side? Ever since the publication of the FFH's paper [12], extensive experimental results [42, 43, 45, 46, 48, 62, 63, 64, 65] have been reported with z ranging from 1.25 to 8.3 and ν from 0.65 to 2. Similar to the case of critical exponents in the zero-field transition, there has been no consensus on the critical exponents for the vortex-glass phase transition from the experiments.

One of the earliest experimental results to support the vortex-glass phase transition is by Koch *et al.* [62]. In their paper, $I - V$ curves of a 0.4 μm YBCO film were measured up to 4 T and $z \simeq 4.8$ and $\nu \simeq 1.8$ were extracted from the data using conventional analysis. Although the results seemed to agree with FFH's predictions, finite sizes of the film were neglected. As we have discussed in Chapter 3, finite-size effects in a YBCO film would prevent us from picking the right "critical isotherm" and critical exponents in the zero-field transition. The crossover current density J_{min} for a 0.4 μm YBCO film is around 10^8 A/m² from Eq. 3.23, and the applied current density ranges from 10^5 A/m² to 10^9 A/m² in [62]. We can thus say that the critical exponents $z \simeq 5$ and $\nu \simeq 1.8$ [62] actually are extracted from the finite-size dominated regime and may not be the true critical exponents. In addition, Coppersmith *et al.* in [66] suggested that the measured $I - V$ curves in [62] could be explained using the flux-creep model.

Many later experimental results did not include finite-size effects in their analysis. Moloni *et al.* [45] [46] found high field vortex glass exponents $z \simeq 4.0$ and

$\nu \simeq 1.9$ for under-doped YBCO films in fields up to 26 T, however, in low fields (<0.1 T), they claimed that $z \simeq 1.25$. Sawa *et al.* in [63] measured $I - V$ curves of YBCO films with thickness ranging from 18 nm to 1000 nm and observed an increase of the exponent z with decreasing thickness (from 4.22 to 9.38).

As we discussed in Chapter 3, crystals are not strongly influenced by finite-size effects in zero magnetic field. If this is also the case in the vortex-glass phase transition, we would expect more consensus on the critical exponents from crystals in the literature. However, crystals' results are even more varied. Gammel *et al.* [64] found that $z = 4.3 \pm 1.5$ and $\nu = 2 \pm 1$ from twinned YBCO crystals in fields from 1 to 6 T. Later experimental results by Yeh *et al.* in [42] and [43] found that $z = 2 \pm 0.2$ and $\nu = 0.9 \pm 0.2$ in Au-doped YBCO single crystals at low fields (0 to 0.6 T) and that $z \simeq 3$ and $\nu \simeq \frac{2}{3}$ in twinned YBCO crystals at fields up to 7 T. Smaller dynamic exponents has been reported by Kim *et al.* in [67] with $z = 1.5 \pm 0.1$ which agrees with Model E dynamics [19].

The critical exponents in the vortex-glass phase transition are expected to be universal constants if the transition exists. The exponents should be independent of the sample, experimental technique and magnitude of the magnetic field. The wide range of computational and experimental results have raised doubts on whether there is a true vortex-glass phase transition [53].

As proposed by FFH [12], one of the key features of vortex-glass phase transition is that the experimental $I - V$ curves should collapse onto two scaling functions on either side of the transition. The data collapse has been used extensively to imply the transition and to extract the exponents. However, data collapse from the

measured $I - V$ curves can be explained using the flux-creep model [66] or the percolative transition model [68], and simulated data based on models without a transition [66, 68, 69] collapse onto two universal curves.

Strachan *et al.* in [53] questioned the vortex-glass transition by showing that data collapse can be achieved for a wide range of critical exponents and temperatures for the same sample. Not only did the paper prove that data collapse alone can not guarantee the existence of a vortex-glass phase transition, but it also partially explained the reported controversial experimental results.

Does the vortex-glass transition really exist? We will first present our experimental results based on the transport measurements on the optimal-doped YBCO films with thickness ranging from 700 Å to 2400 Å and extract the dynamic exponent z from the high-current regime. We will also show that finite-size effects exist in the vortex-glass transition and compare the results with the case in zero-field transition. In the last section of this chapter, we will discuss the first order melting transition for untwinned YBCO single crystals in field.

4.2 Experimental Results of YBCO Films

4.2.1 Conventional Method

We present in Fig. 4.1 the ρ vs. T of a YBCO film (sample su113) with magnetic field parallel to the c -axis. It is obvious that the width of the transition is broadened by the magnetic field.

We begin with the conventional analysis of the $E - J$ curves of sample su113 at

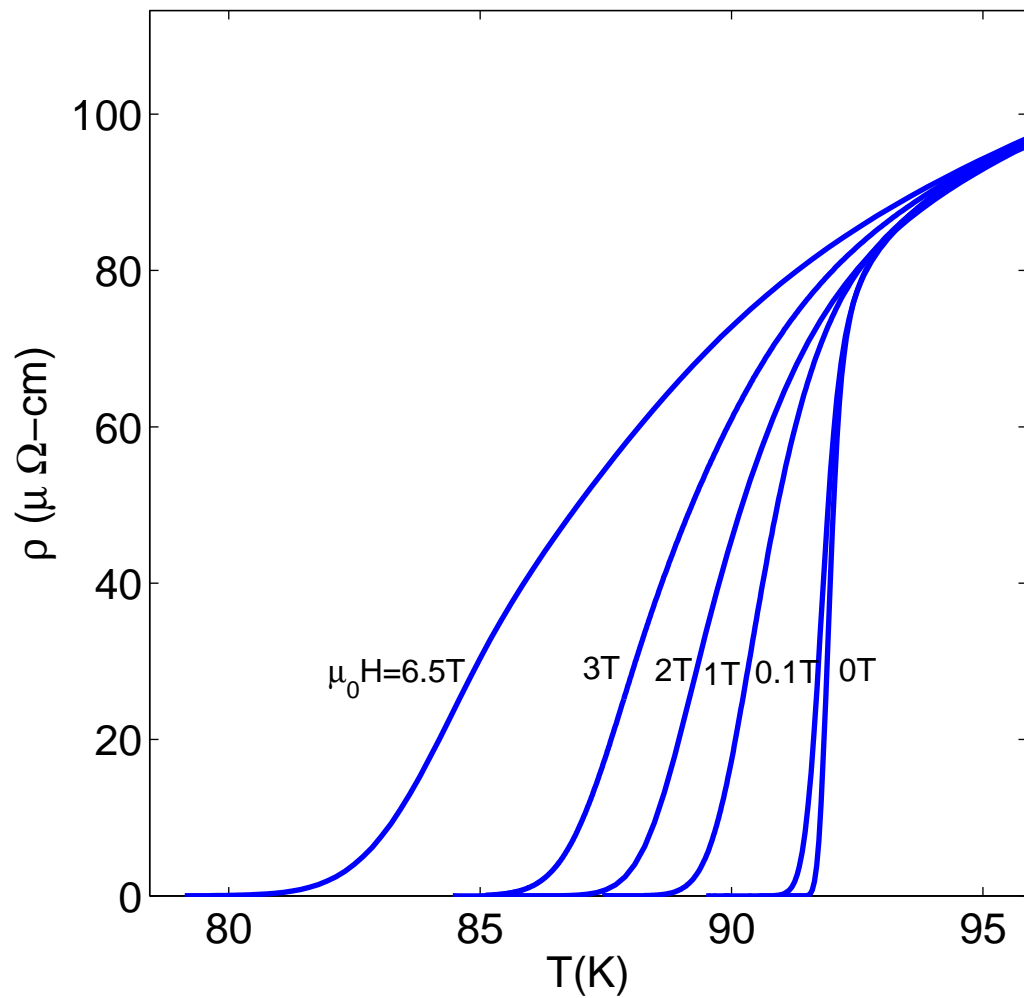


Figure 4.1: Resistivity vs. temperature of a YBCO film (su113) at various magnetic fields. The magnetic field is parallel to the c -axis.

magnetic field of 5 T. The $E - J$ curves in a double-log plot are shown in Fig. 4.2. The isotherms are separated by 0.60 K from 86.70 K to 75.90 K. At high temperatures, the $E - J$ curves are parallel to each other with a slope of 1 (ohmic behavior). At intermediate temperatures, the $E - J$ curves have nonlinear behaviors at high currents and cross over to ohmic at low currents. At low temperatures, the curves have negative curvatures, illustrating vanishing linear resistance.

The transition temperature T_g determined from the conventional analysis is 79.50 K since the isotherm at 79.50 K is the first isotherm without an ohmic tail. From Eq. 4.4, this isotherm should have a power law behavior. We do a linear fit at low currents and find the slope is 2.6 which gives

$$z = 4.2. \quad (4.6)$$

This is very similar to the z values reported for the vortex-glass transition [62] [64].

The other exponent ν can be found through data collapse. From Eq. 4.3, we get

$$\frac{V}{I} \left| \frac{T - T_g}{T_g} \right|^{\nu(1-z)} = \chi_{\pm} \left(\frac{I}{T} \left| \frac{T - T_g}{T_g} \right|^{-2\nu} \right). \quad (4.7)$$

By selecting the appropriate z , ν and T_g , all isotherms should fall on two curves, for above and below T_g , according to FFH [12].

We show the collapse of isotherms from Fig. 4.2 in Fig. 4.3. By keeping $z = 4.2$ and $T_g = 79.50$ K fixed and choosing various ν , we find that the data collapse looks best when $\nu = 1.2$. The ν value is very close to the reported values [62] [64].

However, we have some concerns about the conventional method. The dashed line which is the fit to the power law behavior in Fig. 4.2 crosses some adjacent

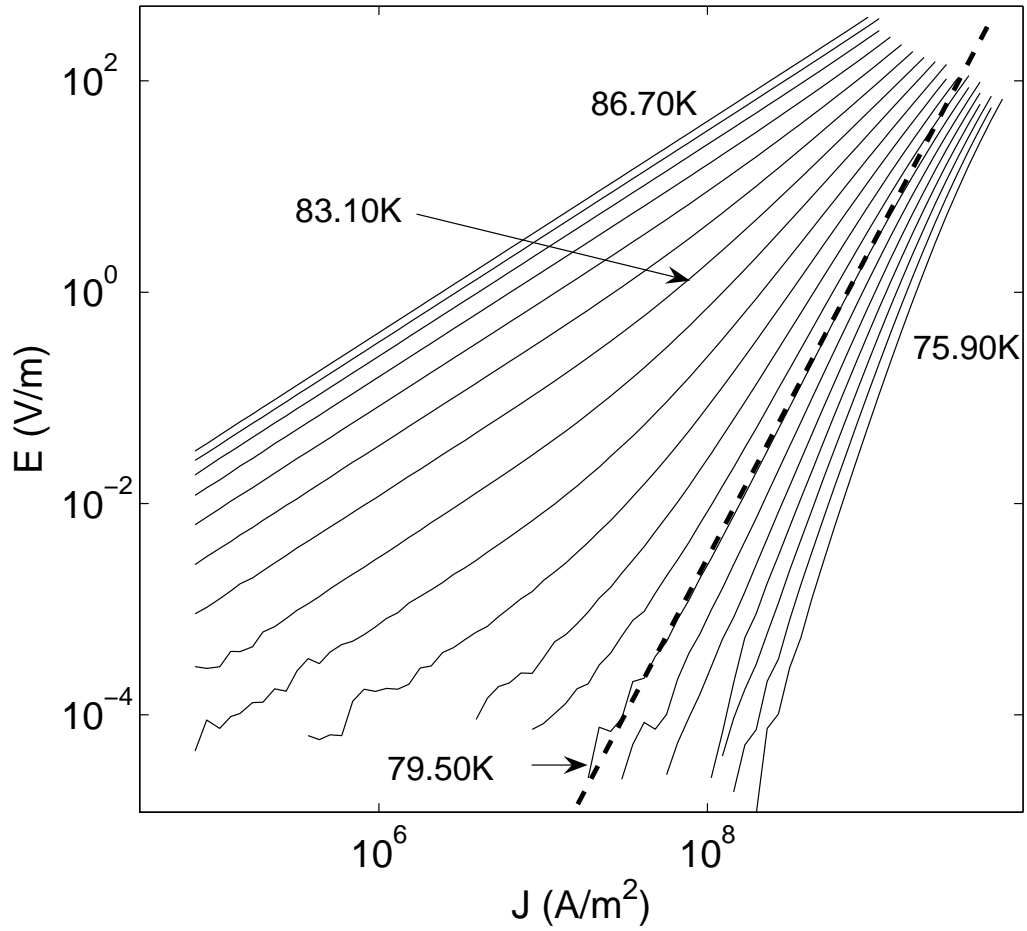


Figure 4.2: $E - J$ curves for sample su113 at 5 T magnetic field. Isotherms are separated by 0.60 K from 86.70 K to 75.90 K. The transition temperature from conventional analysis is $T_g = 79.50$ K. The dashed line at 79.50 K is a power-law fit at lower currents.

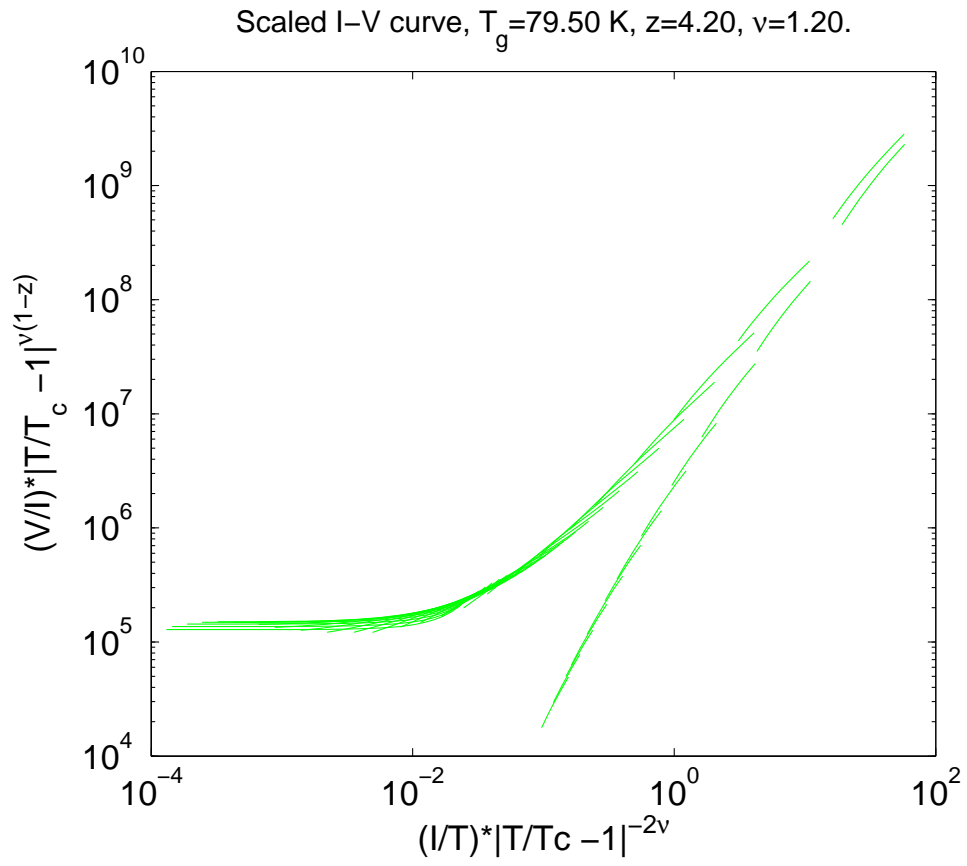


Figure 4.3: Conventional data collapse for sample su113 at 5T field. The transition temperature is chosen as $T_g = 79.50$ K and the exponents are chosen as $z = 4.2$ and $\nu = 1.2$.

isotherms, which is not expected. And we can see systematic deviations from the data collapse in Fig. 4.3.

4.2.2 Derivative Plot

Recall from Chapter 3, that finite-size effects are present in the $E - J$ curves of the YBCO films in zero magnetic field. They prevent us from extracting the correct exponents and transition temperature from the data using the conventional method. We now wonder whether there also exist finite-size effects of the films in the vortex-glass transition. The best way to study the finite-size effects is again the derivative plot [50].

In Fig. 4.4, we show the derivative plot for sample 113 from the isotherms in Fig. 4.2. Clearly, the conventional choice for T_g , 79.50 K, is not a horizontal line in the derivative plot. Thus this isotherm cannot have the power law behavior suggested by Fig. 4.2 and cannot be the correct T_g if the vortex-glass transition exists. Importantly, the derivative plot for su113 at 5 T looks similar to the derivative plot of the same sample in zero field. When $79.50 \text{ K} < T < 83.10 \text{ K}$, the isotherms are monotonically decreasing to the right of the dashed line in Fig. 4.4 and monotonically increasing to the left of the line. This makes us believe that the electric fields converge to zero more quickly than the current density when $J > 4 \times 10^8 \text{ A/m}^2$ and $79.50 \text{ K} < T < 83.10 \text{ K}$, but that vice versa when $J < 4 \times 10^8 \text{ A/m}^2$ and finally the sample becomes ohmic in the limit of zero current. If we only look to the right of the dashed line in Fig. 4.4, the derivative plot looks like the expected behavior shown

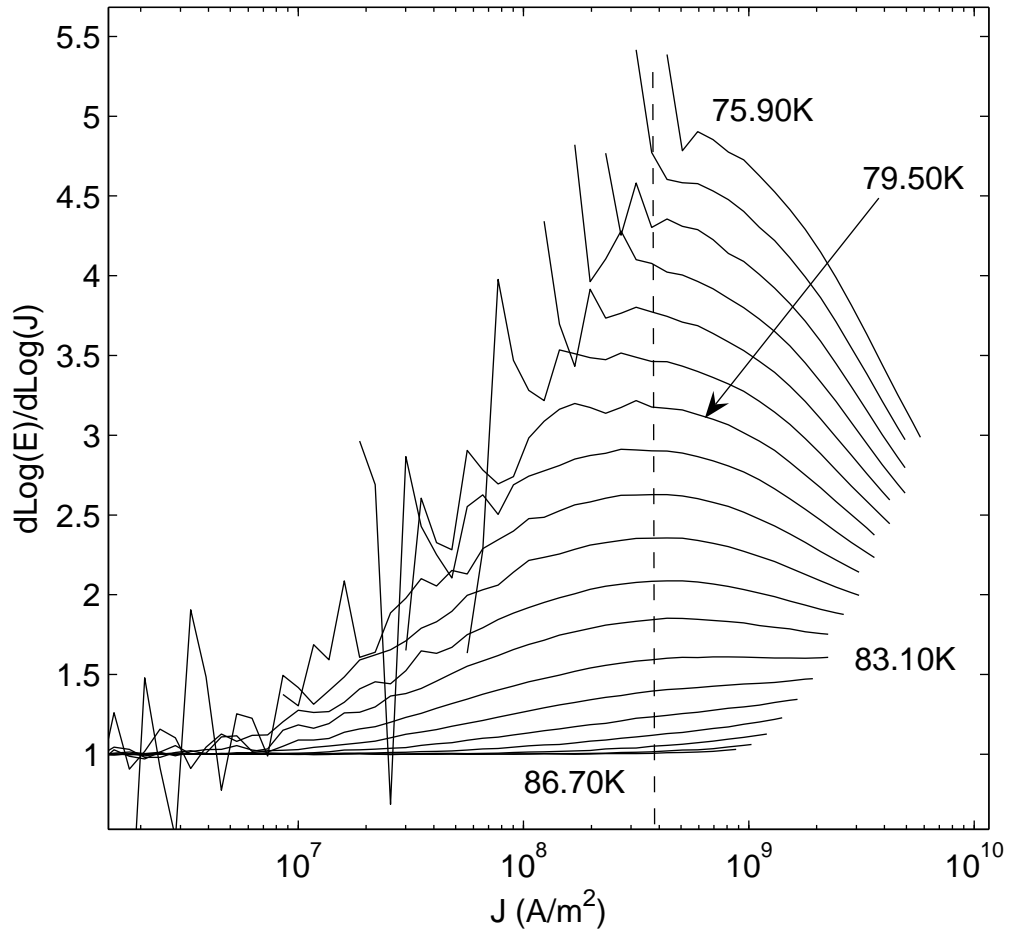


Figure 4.4: $\partial \log(E)/\partial \log(J)$ vs. J for su113 at 5 T field. The conventional choice for T_g , 79.50 K, is clearly not a horizontal line and thus cannot be T_g . The isotherms are separated by 0.60 K.

in Fig. 3.4. We thus have experimental reasons to believe that when $J < 4 \times 10^8$ A/m², finite size effects dominate. The vortex-glass transition may exist but is only visible when $J > 4 \times 10^8$ A/m² for sample su113.

As we did in Chapter 3, we can extract T_g and z from the high-current regime in Fig. 4.4 where there are no finite-size effects. We choose $T_g = 83.10$ K since it is the most horizontal line in the high-current regime. The intercept of this line with the vertical axis is 1.6, combined with

$$\left(\frac{d \log(E)}{d \log(J)} \right)_{T_g} = \frac{z + 1}{2} \quad (4.8)$$

we can find

$$z = 2.2. \quad (4.9)$$

The dynamic exponent, which is close to the value $z = 2$ of Model-A dynamics [19] implies that the motion of vortex line is diffusive.

By comparing the results at 5 T with the results at zero field of the same sample su113, we find that not only the dynamic exponents but also the crossover current densities are different. In zero field, the data start to deviate from the 3D scaling at $J \simeq 7 \times 10^7$ A/m², whereas the data at 5 T start to deviate from scaling at $J \simeq 4 \times 10^8$ A/m². In Section 4.3.1, we will discuss the possible reasons for the differences. We will show how magnetic field can affect the dynamic exponent and the crossover current density of the YBCO films.

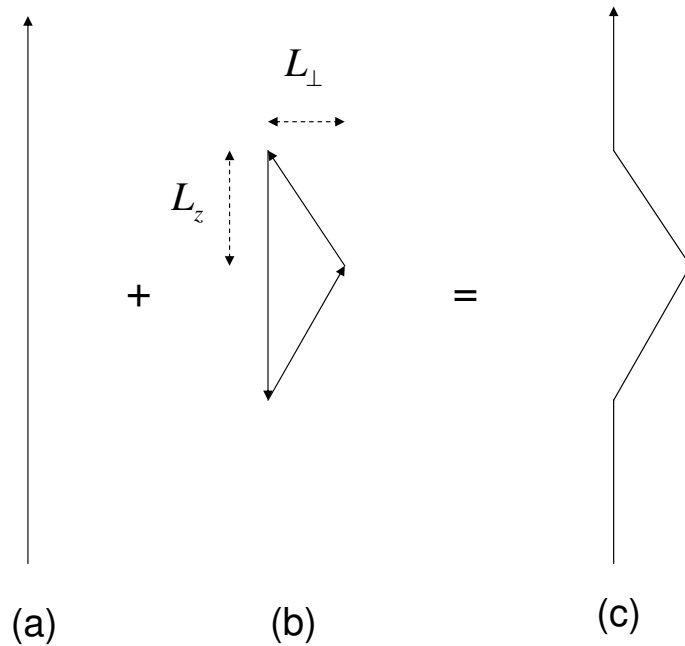


Figure 4.5: A schematic of an excitation of a single vortex line. (a) The initial configuration of the vortex line. (b) The fluctuation takes the form of a vortex loop. (c) The final configuration of the vortex line.

4.3 Discussion

4.3.1 Finite-size Effects in Fields

In Chapter 3, we discussed the vortex-loop picture and showed how thermal fluctuations generate the non-linear behavior in the Meissner state. Now we discuss how a single vortex line subject to quenched impurities is affected by thermal fluctuations and show that this process is related to the vortex-loop picture.

A schematic of an excitation of a vortex line due to thermal fluctuation in the mixed state is shown in Fig. 4.5. The final configuration of a single vortex line is shown in Fig. 4.5(c). It can be seen as a superposition of the initial configuration of a straight vortex line (Fig. 4.5(a)) and a triangular vortex loop (Fig. 4.5(b)). Thus, the fluctuation is similar to a vortex loop fluctuation in the Meissner phase. The difference is that the scaling of the displacement of the excitation in magnetic field is not isotropic as is the vortex loop in zero field. According to [12] and [70], a single vortex line subject to impurities is equivalent to a “directed polymer in a random medium” and hence the scaling is anisotropic. Suppose L_{\perp} is the transverse displacements of a vortex-line segment and L_z is the length of the loop along the z direction. Numerical simulations [70] give

$$L_{\perp} = aL_z^{\zeta} \quad (4.10)$$

with $\zeta \simeq 0.6$.

Creating the segment of length L_z will cost energy. The elastic energy can be approximated by

$$F_k \simeq \varepsilon \frac{L_{\perp}^2}{L_z} = \gamma L_z^{2\zeta-1} \quad (4.11)$$

according to FFH [12]. As L_z increases, we expect the elastic energy F_k to increase or, perhaps stay constant. This means that

$$2\zeta - 1 \geq 0. \quad (4.12)$$

Since L_{\perp} cannot grow faster than L_z , Eqs. 4.10 and 4.12 imply

$$\frac{1}{2} \leq \zeta \leq 1. \quad (4.13)$$

The $\zeta = \frac{1}{2}$ corresponds to the case of thermal fluctuations but no pinning in the mixed state [12] [70] and the $\zeta = 1$ corresponds to the case of isotropic scaling of the vortex-loop in zero magnetic field.

Similar to the free energy of a vortex loop in Eq. 3.16, we can write the free energy of the excitation of a single vortex as

$$F \simeq \gamma L_z^{2\zeta-1} - J\Phi_0 L_z L_\perp = \gamma L_z^{2\zeta-1} - J\Phi_0 a L_z^{1+\zeta} \quad (4.14)$$

in the presence of an external current density J where $L_z L_\perp$ approximates the area of the loop.

Analogous to the treatment of the critical size of a vortex loop in Chapter 3, we can find the critical size of the excitation of a single vortex line by taking the derivative with respect to L_z in Eq. 4.14 and setting it to zero,

$$L_{zc} = \left[\frac{(2\zeta - 1)\gamma}{(1 + \zeta)aJ\Phi_0} \right]^{\frac{1}{2-\zeta}}. \quad (4.15)$$

When $\zeta = 1$ and $\gamma = \varepsilon$, we get the same result (Eq. 3.17) as the critical size of vortex loop in zero field. The corresponding energy barrier is thus

$$F_c = \frac{\gamma^{\frac{1+\zeta}{2-\zeta}}}{(aJ\Phi_0)^{\frac{2\zeta-1}{2-\zeta}}} \left[\left(\frac{2\zeta-1}{1+\zeta} \right)^{\frac{2\zeta-1}{2-\zeta}} - \left(\frac{2\zeta-1}{1+\zeta} \right)^{\frac{1+\zeta}{2-\zeta}} \right] = \frac{c}{(J\Phi_0)^\mu} \quad (4.16)$$

where

$$c = \gamma^{\frac{1+\zeta}{2-\zeta}} \left[\left(\frac{2\zeta-1}{1+\zeta} \right)^{\frac{2\zeta-1}{2-\zeta}} - \left(\frac{2\zeta-1}{1+\zeta} \right)^{\frac{1+\zeta}{2-\zeta}} \right] \quad (4.17)$$

and

$$\mu = \frac{2\zeta-1}{2-\zeta}. \quad (4.18)$$

The resistivity can thus be written as

$$\rho \equiv \frac{E}{J} \sim e^{-\frac{F_c}{2k_B T}} \sim e^{-(\frac{J}{J_c})^\mu} \quad (4.19)$$

where

$$J_T = \left(\frac{c}{2k_B T}\right)^{\frac{1}{\mu}} \frac{1}{\Phi_0}. \quad (4.20)$$

Note that when $\mu = 1$ we get the same result as in Eq. 3.21 in the Meissner phase. If the vortex-loop excitations are the dominant nonlinear dissipative process in the vortex-glass phase, we will not have linear resistivity in the limit of zero current in contrast to the flux-creep theory [11].

Since the vortex-loop excitations exist in both the Meissner phase and vortex-glass phase, it is natural to make the following conjecture. The finite-size effect which occurs in the zero-field transition of the YBCO films also exists in the vortex-glass transition. There should exist a crossover current density J_{min} . Above J_{min} , the YBCO films obey the 3D scaling described in Eq. 4.3. Below J_{min} , the growth of the vortex-loop is limited by the thickness of the film and the system deviates from 3D scaling behavior. The consequence is that even in the vortex-glass phase, YBCO films will have linear resistivity in the limit of zero current. The vanishing linear resistivity predicted by Eq. 4.19 is thus only valid in the high-current regime.

From Fig. 4.4, we find that at 5 T, the film deviates from 3D scaling at around 4×10^8 A/m² whereas in the zero-field transition, the same film deviate from 3D scaling at 7×10^7 A/m² from Fig. 3.10. We present J_{min} vs. H in Fig. 4.6 for the sample su113, where we define J_{min} to be the current density where the system deviates from 3D scaling. J_{min} increases when $\mu_0 H$ changes from 0 T to 1 T, but stays relatively constant above 1 T. We have seen the same behavior for samples with different thickness (800 Å and 2400 Å).

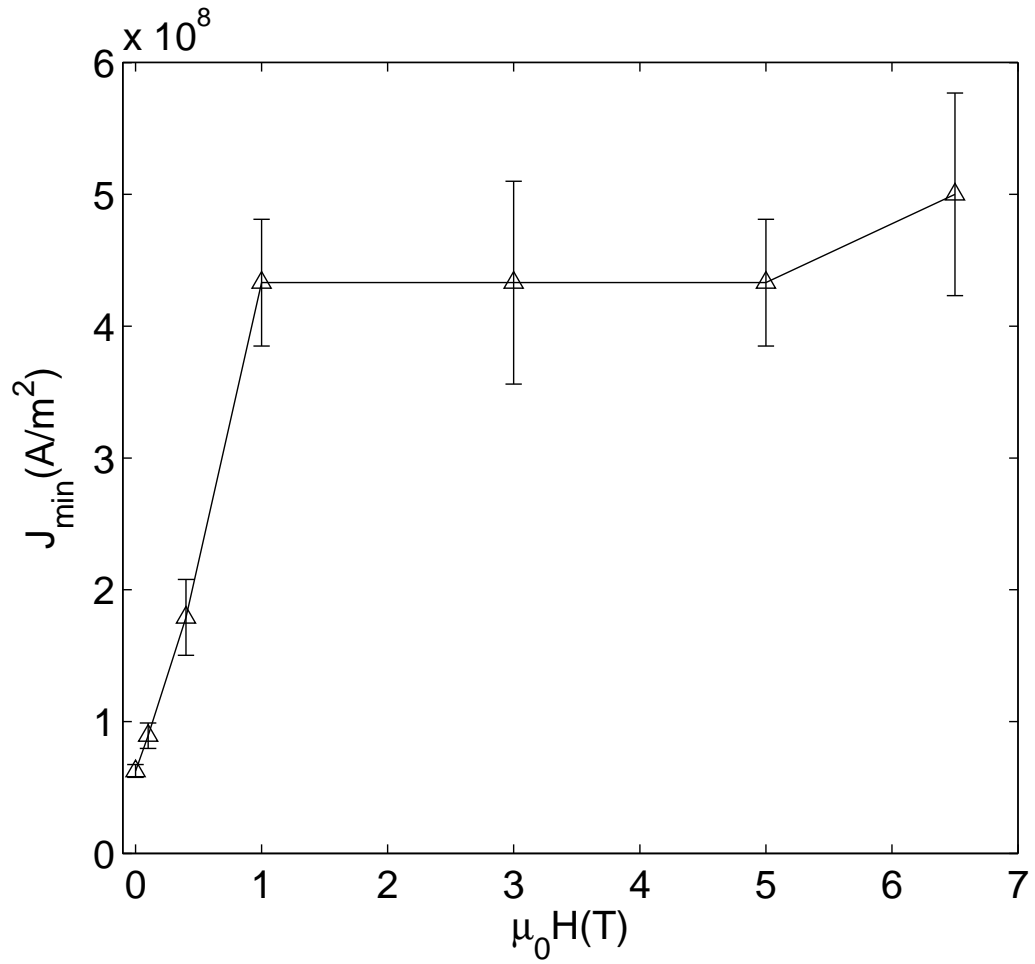


Figure 4.6: Crossover current density J_{min} as a function of magnetic field H of sample su113. J_{min} increases as the magnetic field increases from 0 T to 1 T and stays relatively stable above 1 T. The thickness of the film is 150 nm.

We next try to find out what causes the difference between the results at high field and zero field. At high magnetic field, the scaling of the vortex loop excitation is not isotropic. From Eq. 4.10, the displacement long z direction L_z grows at a faster rate than the displacement L_\perp along the ab plane. In the Meissner phase, the critical size of a vortex loop L in a typical thermal fluctuation scales with J as $L \propto J^{-\frac{1}{2}}$. Thus, if L_{zc} scales with J with an exponent less than $-\frac{1}{2}$, it is possible for the films to experience a higher crossover current density in the field than in zero field.

Setting the energy of a fluctuation, Eq. 4.11, equal to $k_B T$ gives

$$\varepsilon \frac{L_\perp^2}{L_z} = \gamma L_z^{2\zeta-1} = k_B T. \quad (4.21)$$

By solving Eq. 4.21, we arrive the typical size of a vortex loop in vortex-glass transition

$$L_{z_thermal} = \left(\frac{k_B T}{\gamma} \right)^{\frac{1}{2\zeta-1}}. \quad (4.22)$$

The current probing length scale in the vortex-glass phase transition can be found by

$$L_{z_thermal} = L_{zc} \equiv L_J. \quad (4.23)$$

Combining Eqs. 4.15, 4.22 and 4.23 gives

$$L_J \approx \left(\frac{k_B T}{a J \Phi_0} \right)^{\frac{1}{1+\zeta}}. \quad (4.24)$$

The crossover current density J_{min} in the vortex-glass transition is thus

$$J_{min} \approx \frac{(2\zeta - 1)k_B T}{(1 + \zeta)a\Phi_0 d^{1+\zeta}}. \quad (4.25)$$

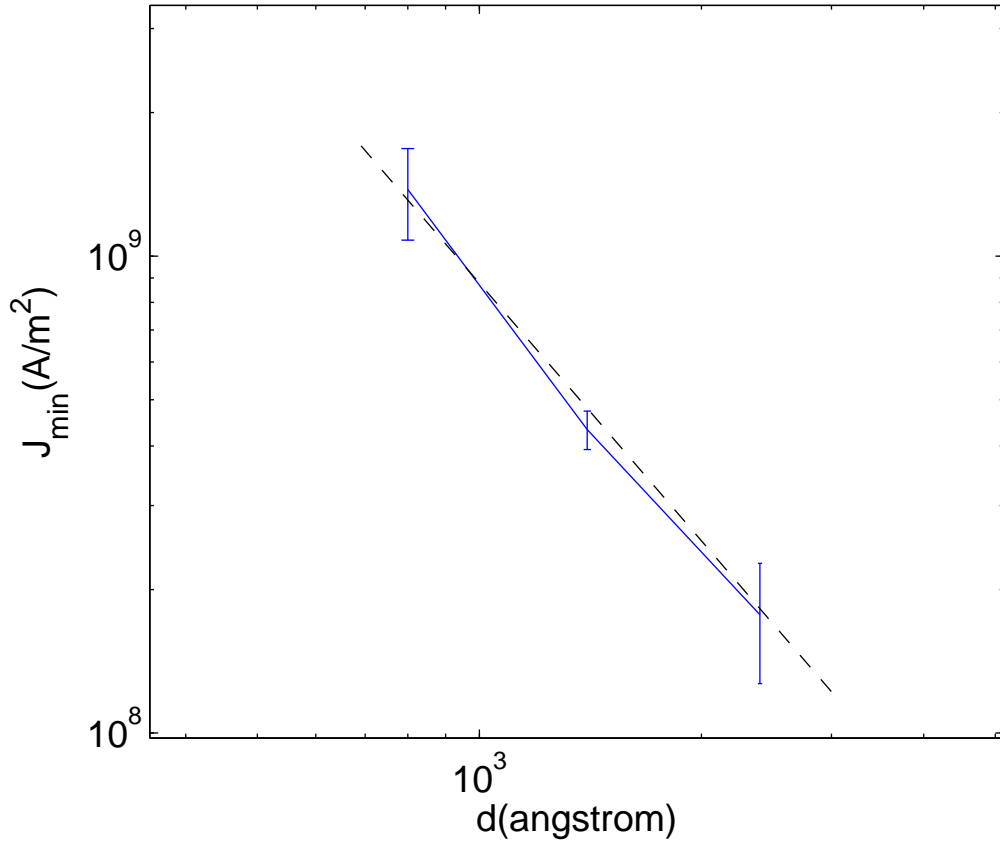


Figure 4.7: J_{min} as a function of thickness d for three different films. The dashed line is a power law fit to the data, with a slope of -1.6 ± 0.2 . The slope of the line gives $1 + \zeta = 1.6 \pm 0.2$, as expected.

where d is the thickness of the film. From Eq. 4.25, we expect the crossover current density J_{min} to have a power law relation with film thickness d with an exponent of $-(1 + \zeta)$. We test this power law behavior by plotting J_{min} at high fields *vs.* thickness in a double-log scale as shown in Fig. 4.7. The dashed line is a power law fit to the data, which gives $J_{min} \sim d^{-1.6 \pm 0.2}$. Combining with Eq. 4.25 gives

$$\zeta = 0.6 \pm 0.2 \tag{4.26}$$

which agrees with the simulation result [70].

4.3.2 Dynamical Critical Exponent z in Field

The dynamic exponent z determined in the high-current regime by derivative plot for sample su113 at $H = 5$ T is 2.2 ± 0.2 where as the result at zero magnetic field is 1.54 ± 0.1 for the same film. Clearly, our results do not agree with the prediction by FFH [12], $z \simeq 4$ to 7 and some experimental results [48] [62] and [64]. From [19], we know that the dynamic exponent z from model-A dynamics is 2 which makes us believe that the dynamical universality class of the transition at high fields corresponds to Model A dynamics.

A question naturally rises: does the exponent z jump from 1.5 to around 2 when an external field is turned on or smoothly crossover to 2 with the increasing of the external field? To answer this question, we make a plot of z vs. H of three YBCO films with different thickness as shown in Fig. 4.8. Similar to J_{min} in Fig. 4.6, the dynamic exponent z increases from around 1.5 to around 2.0 as the external magnetic field increases from 0 T to 1 T for all three samples. Above 1 T, z stays relatively constant in a range 1.9 to 2.4. Instead of a sharp jump, there is a crossover from model-E dynamics to the model-A dynamics in the intermediate fields ($0 \text{ T} < H < 1 \text{ T}$).

Given that J_{min} and z both have similar behavior in intermediate fields, we conjecture that thermal fluctuations create both vortex-loops as in the Meissner state with isotropic scaling (Fig. 3.2) and vortex-loops which are attached to vortex lines

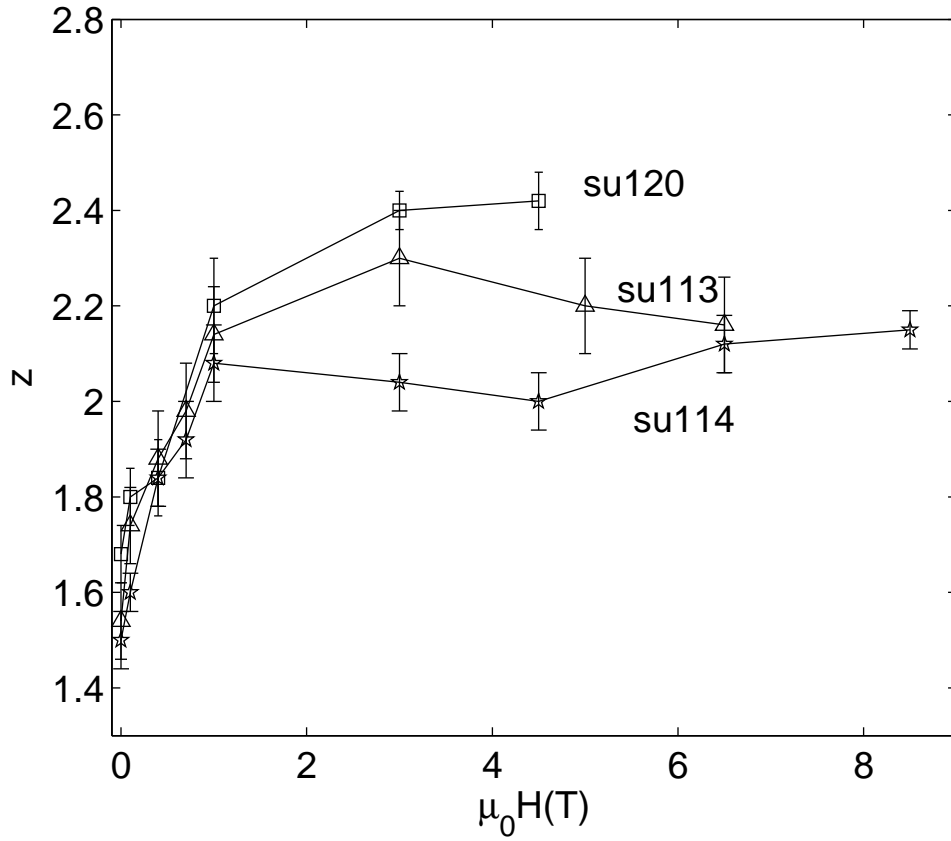


Figure 4.8: z vs. H of sample su113, su114 and su120. At zero field, the dynamic exponent z for all three films falls into the range of 1.5 to 1.7. At magnetic fields above 1 T, z has a range of 1.9 to 2.4. In intermediate fields, all three films crossover from model-E dynamics to model-A dynamics.

with anisotropic scaling (Fig. 4.5). The former vortex-loops corresponds to model-E dynamics whereas the later vortex-loops corresponds to model-A dynamics. z extracted from the data in the intermediate fields falls into (1.5, 2.0), depending the relative populations of the two kinds of loops. When the field increases, the spacing between the vortex lines decreases and fewer excitations take the form of the loop with isotropic scaling. We expect that above high enough field, z is constant since nearly all the excitations take the form of the loops with anisotropic scaling. This qualitative argument explains the crossover from model-E dynamics to model-A dynamics between zero field and high fields. Using the same argument, we also can explain the behavior of J_{min} shown in Fig. 4.6.

4.4 Experimental Results of YBCO Crystals

If we were able to find the dynamic exponent z from optimally-doped YBCO crystals in the mixed state, we could compare with the results we found for the films as discussed above in section 4.2. Unfortunately, the YBCO single crystals we have are untwinned. According to Tinkham [6], clean samples of high temperature superconductors, because of their weak disorder, experience a first-order melting transition from a vortex-solid phase to a vortex-liquid phase instead of a second-order vortex-glass transition.

There are experiments that support the existence of the first-order melting transition. DC transport measurements by Safar *et al.* [71, 72, 73] revealed hysteresis in resistance *vs.* temperature curves which is evidence for a first-order transition in

fields up to 7 T. Magnetization measurements by Welp *et al.* [74] and Rykov *et al.* [75] demonstrated jumps of the magnetization of the untwinned YBCO crystals, again indicating a first-order phase transition. There is also a specific heat measurement by Schilling *et al.* [76] that observed a latent heat. The first-order melting transition can change its nature to a continuous transition when above a critical point H_{cp} [77] or when the doping level is changed [75].

In disordered crystals, such as crystals with twin boundaries [64] or irradiated crystals [65], the transition is predicted to be continuous from the vortex-fluid phase to the vortex-glass phase. However, as we discussed in the beginning of this chapter, there is no consensus on the values of the dynamic exponent z and static exponent ν .

We have measured the resistivity and current-voltage characteristics of an untwinned YBCO single crystal (sample C1) using the four-probe method in the magnet as described in the second chapter. Current was applied to the a axis of the crystal. The magnetic field can go up only to 9 T, so the transition of the crystal in field is first-order. The resistivity ρ as a function of temperature T of the crystal at various magnetic fields H is shown in Fig. 4.9. In zero field, the crystal experiences a continuous phase transition with a transition temperature of $T_{c0} = 93.836$ K and the width ΔT_{c0} less than 100 mK. In non-zero magnetic fields, the resistivity drops to zero in the form of a sharp “kink” at low temperatures. Looking at $H = 5$ T in Fig. 4.9 for example, the resistivity ρ drops continuously above 84.011 K and it drops sharply from $\rho_{kink} = 6.92 \mu\Omega\text{cm}$ to 0 just below 84.011 K. The width is less than 30 mK.

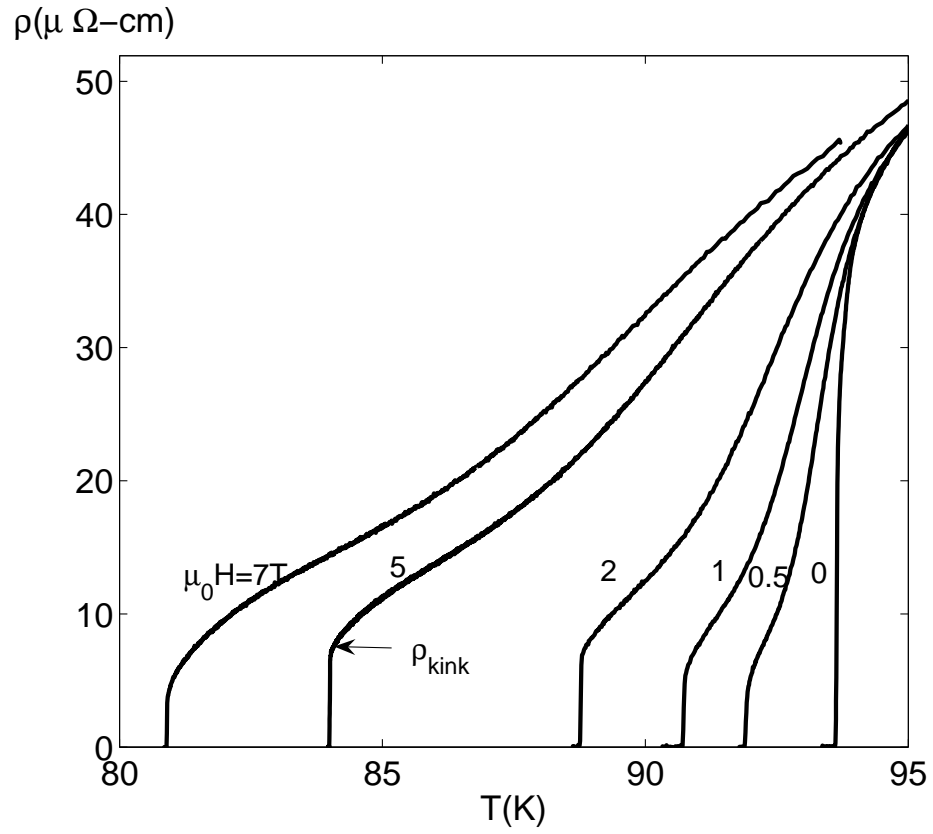


Figure 4.9: Resistivity as a function of temperature of an untwinned YBCO single crystal at various values of magnetic field. The magnetic field is applied along the c axis.

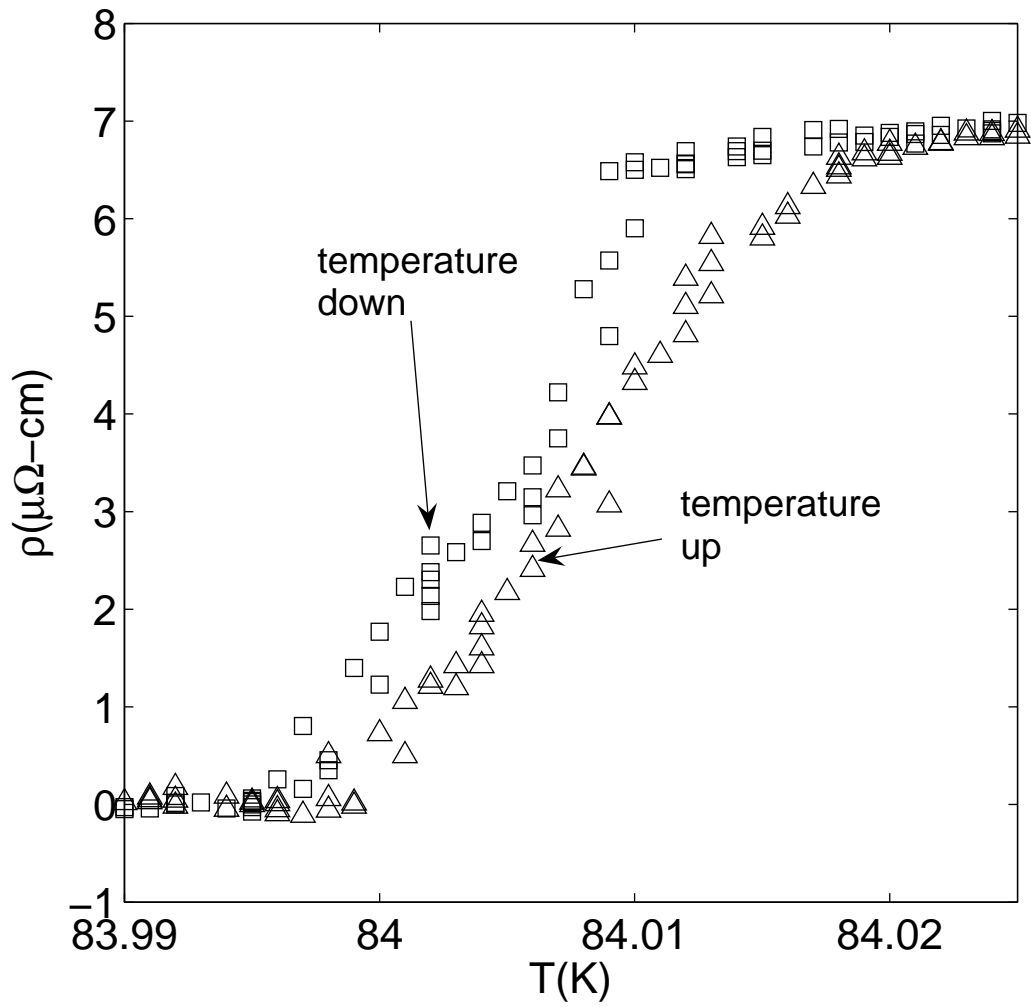


Figure 4.10: Hysteresis of the resistivity of an untwinned YBCO single crystal (sample C1) at 5 T.

Fig. 4.10 shows the hysteresis of the resistivity measured while ramping temperature in opposite directions at fixed field $H = 5$ T. The squares represent the data ramping the temperature up and the triangles represent the data ramping the temperature down. We observe a 5 mK width of the hysteresis loop which is strong evidence of a first-order transition. The hysteresis loop is not due to the thermal lag of the system since we can not observe any hysteresis in the resistivity at zero field and small fields such as $H = 0.05$ T. The width of a noticeable hysteresis loop at $H = 1$ T is around 1 mK whereas at $H = 8$ T, the width of the loop is 4 mK.

In Fig. 4.11, we plot ρ_{kink} as a function of magnetic field. ρ_{kink} is the resistivity of the crystal just before the sharp drop which is seen in Fig. 4.9. It can be viewed as a measure of the strength of the first-order transition. At zero field, the resistivity is continuous and of course there is no ρ_{kink} . ρ_{kink} is around $5 \mu\Omega\text{cm}$ at small field $H = 0.5$ T and $7 \mu\Omega\text{cm}$ at $H = 5$ T. It then rapidly decreases to $2.6 \mu\Omega\text{cm}$ at $H = 8$ T. A critical point $H_{cp} \simeq 9$ T where $\rho_{kink} = 0$ can be extrapolated from the data shown in Fig. 4.11. It is expected that above this critical point $H > H_{cp}$, the transition is second order again. The value for the critical point we found is very close to values reported in the literature: $H_{cp} \simeq 9.75$ T [72] and $H_{cp} \simeq 10$ T [77].

Since the magnetic field of our magnet can not exceed 9 T, we cannot measure the $E - J$ curves to extract the critical exponents in the regime where the transition is unambiguously second-order. But we still are able to study the nonlinear $E - J$ curves of the first-order transition. Fig. 4.12 shows the $E - J$ curves of the crystal at $H = 4$ T. The isotherms are from 85.573 K to 85.546 K and the spacing of the isotherms is 3 mK. Fig. 4.12 does not show the behavior expected of a continuous

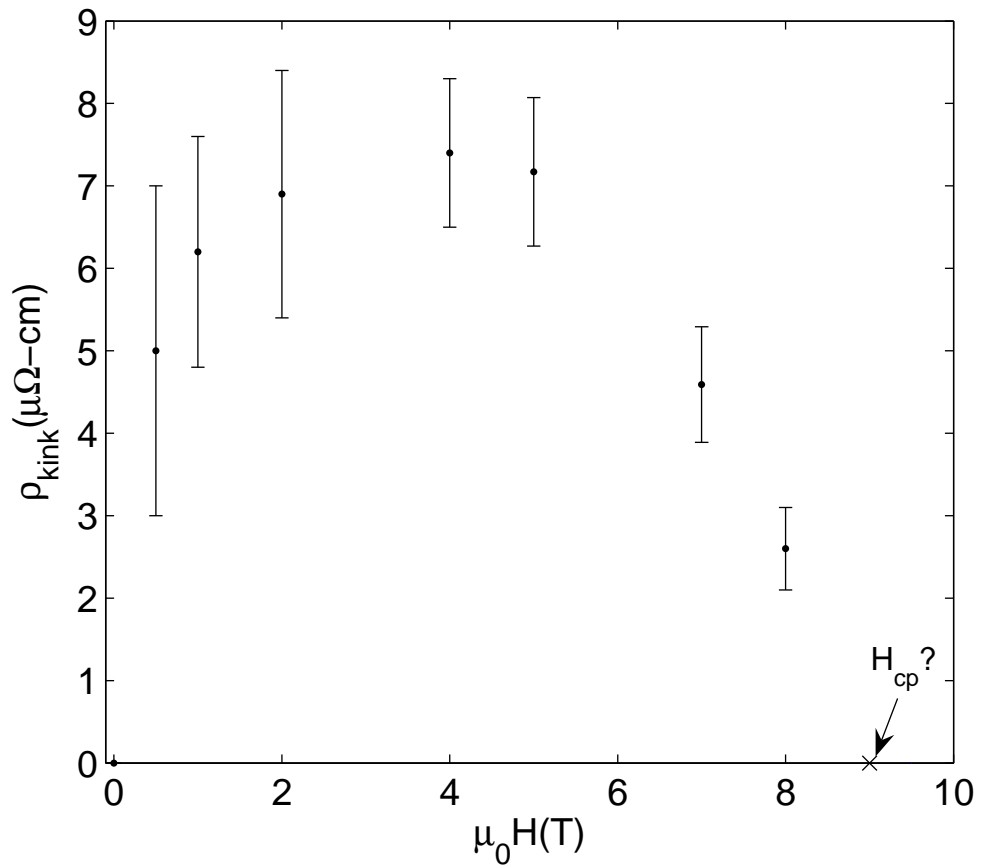


Figure 4.11: ρ_{kink} as a function of magnetic field H . A critical point at $H \simeq 9$ T can be extrapolated from the data.

transition as seen in Fig. 3.3. There is no isotherm with a power law behavior that separates two groups of isotherms with opposite curvatures. The isotherm of 85.561 K first displays downward curvature (vanishing linear resistance) at high currents but then crosses over to ohmic at low currents. This looks like the finite-size effects that we saw in YBCO films.

We showed in Chapter 3 that YBCO crystals do not have finite-size effects in the zero-field transition. These crystals are untwinned so that finite-size effects cannot come from the twin boundaries as proposed by Yeh *et al.* [43]. Before finding whether the effects are due to finite-size effects or other possible reasons such as flux creep, we have to extract the crossover current density from our data.

In Fig. 4.13, we show the derivative plots corresponding to the $E - J$ curves in Fig. 4.12. For $85.561 \text{ K} \leq T < 85.570 \text{ K}$ and $J > 1.2 \times 10^4 \text{ A/m}^2$, the curves are monotonically decreasing but crossover to 1 (ohmic behavior) when $J < 1.2 \times 10^4 \text{ A/m}^2$. We can define $J_{min} = 1.2 \times 10^4 \text{ A/m}^2$ to be the crossover current density for this $103 \mu\text{m}$ thick crystal. Note that when $T < 85.561 \text{ K}$, the curves do not crossover to ohmic only because when $J < 1.2 \times 10^4 \text{ A/m}^2$, the voltage across the crystal is less than the resolution of our nano-voltmeter and the possible existence of ohmic behavior due to finite-size effects below J_{min} cannot be observed by our setup.

To understand how the crossover current density J_{min} of crystals in field relates with the ones of the films in nonzero field and zero field we discussed earlier, we show J_{min} as a function of sample thickness d for films in Fig. 4.14. If we extrapolate the data of films to $d = 103 \mu\text{m}$ (the thickness of the crystal), we get an estimated

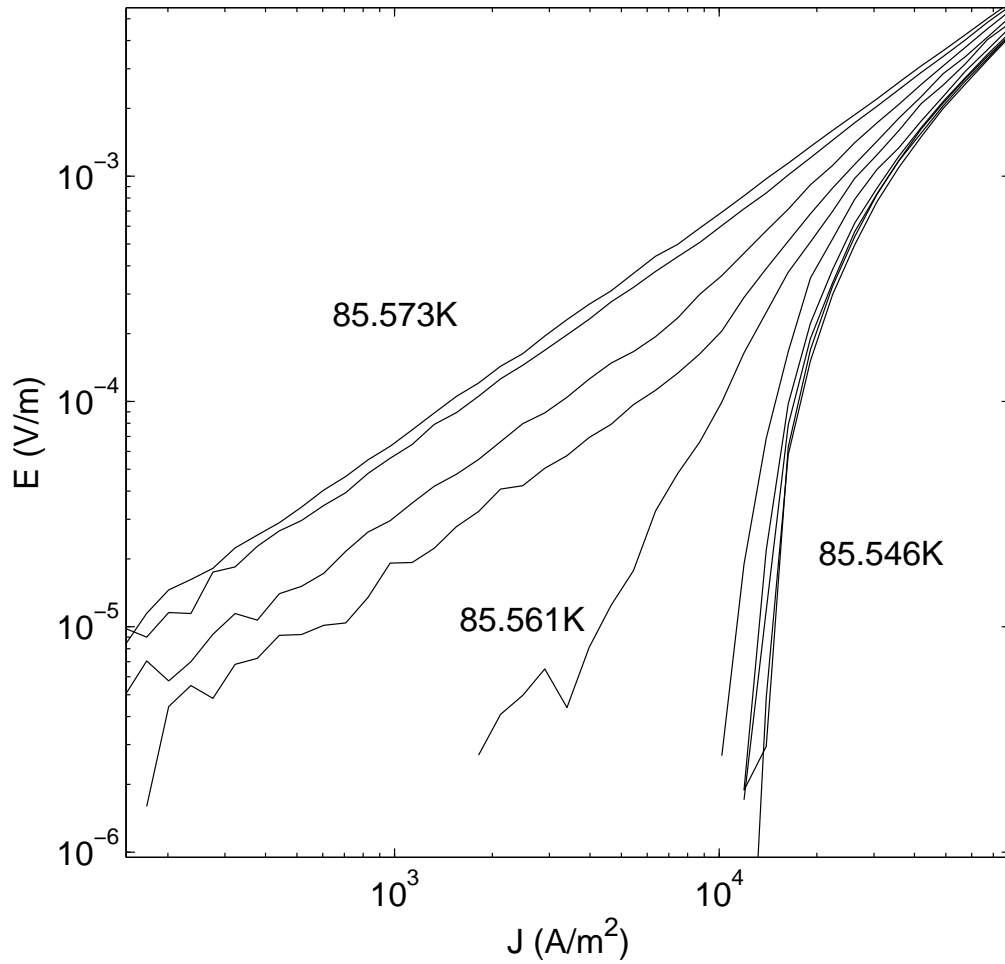


Figure 4.12: $E - J$ curves of an untwinned YBCO single crystal (sample C1) at $H = 4$ T. The spacing of the isotherms is 3 mK.

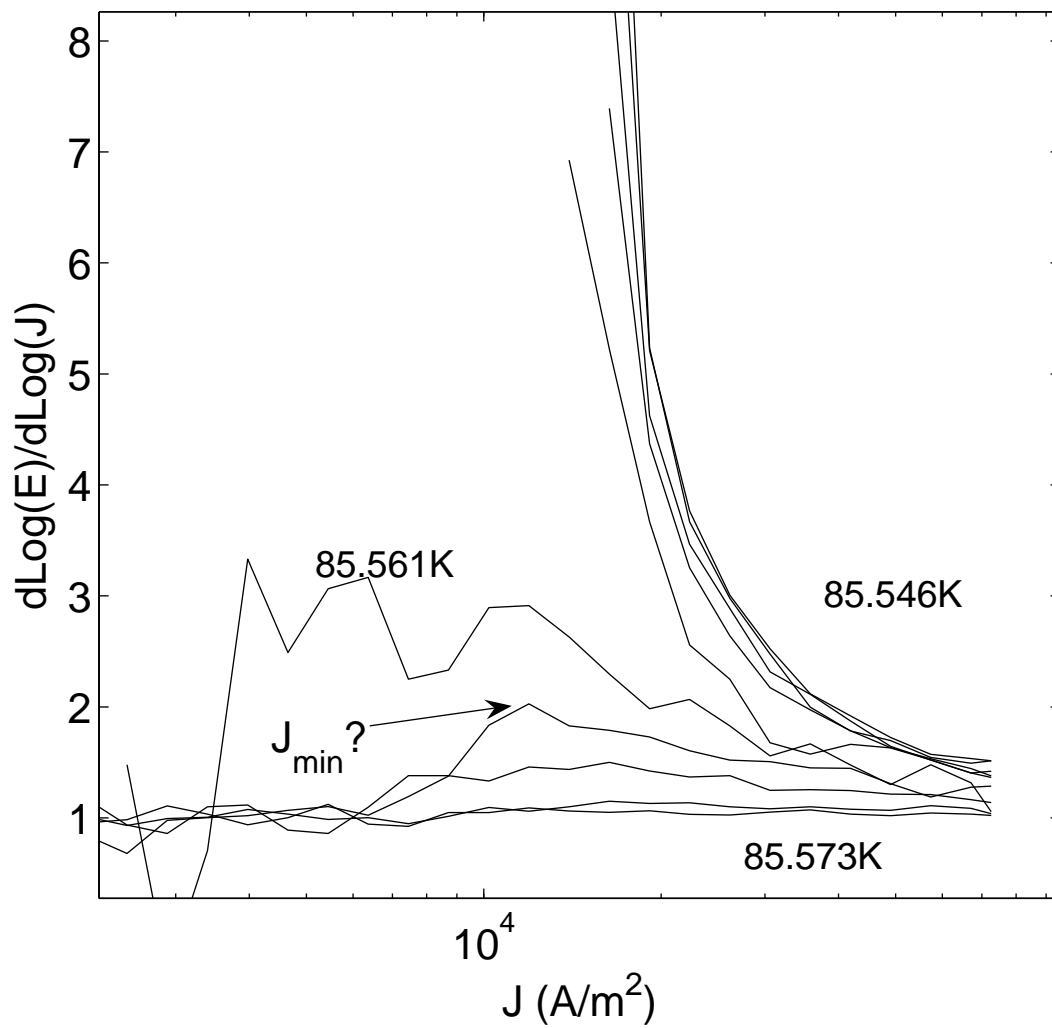


Figure 4.13: Derivative plot of the same curves from Fig. 4.12. The spacing of the isotherms is 3 mK.

$J_{min} \simeq 6 \times 10^3 \text{ A/m}^2$ as seen from the upper dashed line. The expected value is not far from our actual experimental result ($1.02 \times 10^4 \text{ A/m}^2$) which means that even though the transition of the crystal in field is first-order, it still has a process similar to the anisotropic vortex-loop in the superconducting state. The typical loop due to thermal fluctuation cannot exceed the thickness of the crystal at low currents, leading to a crossover to ohmic behavior as seen from Figs. 4.12 and 4.13.

Why can't we observe finite-size effects in zero field? If we extrapolate the zero field film's data, the estimated crossover current density at $d = 103 \text{ }\mu\text{m}$ is around $5 \times 10^2 \text{ A/m}^2$, which is much smaller than the current shown in Fig. 3.5. This means that the crystal data that we used to determine the critical exponents is not affected by finite-size effects.

The discussion helps explain the controversial results regarding critical exponents in zero and nonzero field. The YBCO crystals used in Gammel *et al.*[64] and Yeh *et. al* [42] [43] are of the same order of thickness of our crystals and their current range is 10^2 A/m^2 to 10^5 A/m^2 . It is thus possible that finite-size effects are present in their data in the form of ohmic tails below T_g or T_c . Overlooking the finite-size effects may cause one to choose the wrong transition temperature and may account for the disagreement of the critical exponents z and ν .

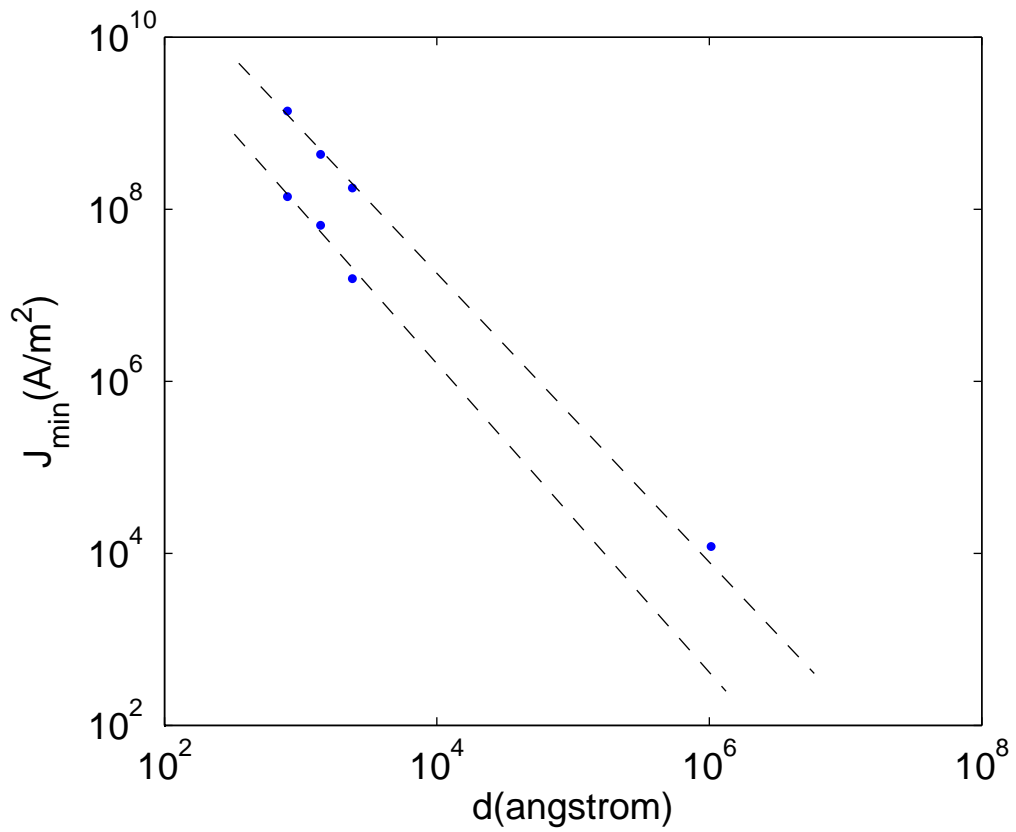


Figure 4.14: Crossover current density J_{min} as a function of sample thickness d in zero magnetic field and high magnetic field.

Chapter 5

Summary and future works

5.1 Summary

In this work, we investigated the normal to superconducting phase transitions in zero and non-zero magnetic field by DC transport measurements.

The samples we used are $\text{YBa}_2\text{Cu}_3\text{O}_{7-\delta}$ (YBCO) films and crystals. High quality YBCO films were made by pulsed laser deposition and properties of the films were tested by AC susceptibility, X-ray diffraction and atomic force microscopy. The transition temperatures of the films are usually above 91.0 K and the widths are usually 0.2 K to 0.3 K (full width of half maximum of the peak in AC susceptibility data). The films then were patterned into four-probe bridges by photolithography. High quality untwinned YBCO single crystals [29, 30] were provided by Dr. Kouji Segawa and Dr. Yoichi Ando from Central Research Institute of Electric Power Industry, Tokyo, Japan.

In the zero-field DC measurements, the cryostat is covered by μ -metal shield and the sample probe is equipped with low-pass filters so that the ohmic tails caused by residual field and current noise can be greatly reduced [31, 49]. Finite-size effects are observed at low currents in the films' data and they create ohmic tails in the $E-J$ curves for isotherms below the transition temperature T_c . Thus, the conventional data analysis method will give misleading results for T_c and critical exponents z and

ν . Instead, we use the derivative plot at high currents to determine T_c and z from the films' data and found that $z = 1.5 \pm 0.2$. We also found $\nu = 0.62 \pm 0.1$ by fitting the melting line in the mixed state which agrees with the 3D-XY result: $\nu = 0.67$ [21, 22].

The $E - J$ curves of the crystals' data are not affected by finite-size effects. We got consistent $z \simeq 1.5$ from both the conventional method and the derivative plot method. We also found the static critical exponent $\nu = 0.68 \pm 0.1$ which is consistent with the result from 3D-XY model. The z and ν values determined from the films' data and crystals' data implies that the zero-field transition of high-temperature superconductors belongs to 3D-XY universality class with model-E dynamics [19].

In our study of the non-zero field transition, the sample probe is placed inside the "Blue Magnet" which can go up to 9 T. Because of the strong disorder, the YBCO films experience a second-order phase transition proposed by FFH [12]. The crossover current density J_{min} at which $E - J$ curves deviated from 3D scaling because of finite-size effects differs with the case in zero field. We attribute this to anisotropic scaling of the vortex-loop in the mixed state. The scaling of the vortex-loop in zero field is isotropic. This explanation may also account for the z dependence on the magnetic field H . In the presence of high magnetic field ($H > 1$ T), we found that $z \simeq 2$ which means that the system crosses over from model-E dynamics to model-A dynamics [19].

Because of the very weak disorder in the untwinned YBCO single crystals, the phase transition in the mixed state is a first-order melting transition from vortex-solid phase to vortex-liquid phase for $H < 9$ T. We observed hysteresis in the

resistivity *vs.* temperature measurements and found a critical point $H_{cp} \simeq 9$ T which agrees with previous results [71, 77]. We also observed finite-size effects in the crystal's data in fields, the J_{min} of which agrees with the extrapolation of the J_{min} of films at high fields.

5.2 Future Work

It is believed that the untwinned YBCO single crystals experience a continuous phase transition at $H > 10$ T. If DC transport measurements are performed at such high field, it will be interesting to see whether the $E - J$ characteristics of such phase transition follows a scaling behavior as seen in Eq. 4.3 and whether the critical exponents extracted from the data agree with the results from films' data ($z \simeq 2$). This will help us determine whether the phase transition at high field (> 10 T) is the vortex-glass phase transition.

DC transport measurements on YBCO single crystals with twin boundaries might be another good approach since it is believed [12, 6] the disorder from the twin boundaries is strong enough to make the transition in non-zero field continuous. Although there has been work [64, 43] on this subject, there is still no consensus on the exponents. Previous work may have overlooked the finite-size effects of the crystals in field. As we have seen from the films' data, magnetic field can enhance finite-size effects. Although it does not affect the zero-field transition, finite-size effects may exist in the transition in the mixed state. We don't have direct evidence for this, but the extrapolation from films' data and the finite-size effects we saw in

the melting transition of the untwinned crystals may suggest its existence.

$\text{Pr}_{2-x}\text{Ce}_x\text{CuO}_4$ (PCCO) is an electron-doped high-temperature superconductors whose crystal structure is more anisotropic than YBCO and has a transition temperature T_c of around 20 K, much less than the T_c of YBCO. Calculation from Eq. 1.21 shows a critical regime in the order of 1 mK for PCCO. Preliminary results on the DC transport in zero field suggest that the nonlinear $E - J$ curves observed may be due to the sample inhomogeneity and that we cannot observe the scaling since the critical regime is experimental inaccessible. However, we still observed the finite-size effects in low currents. More samples with different thickness d should be studied to determine the J_{min} as a function of d in order to compare to the results on YBCO [50].

Chapter A

Currents and Lengths in Superconductors (Lobb's note)

A.1 Initial considerations

Consider a simple model for fluctuations in superconductors, where I assume that the only fluctuations are circular vortex loops of radius r . The energy of such a loop can be written as

$$U_{loop} = 2\pi r \varepsilon(r) \quad (\text{A.1})$$

where $\varepsilon(r)$ is the energy per unit length of the vortex loop. For a straight vortex, Tinkham [6] Eq. 5.17 shows that, in Gaussian units,

$$\varepsilon(r = \infty) = \left(\frac{\Phi_0}{4\pi\lambda} \right)^2 \ln \left(\frac{\lambda}{\xi} \right). \quad (\text{A.2})$$

In general, curvature will increase the energy per unit length.

In an infinite superconductor with no applied current, vortex loops of different sizes occur with different probabilities as thermal fluctuations. Formally, the probability of finding a loop of size r in a range dr is given by

$$P(r)dr = \frac{e^{-\frac{2\pi\varepsilon(r)}{k_B T} r} r}{\int_{\xi}^{\infty} e^{-\frac{2\pi\varepsilon(r)}{k_B T} r} dr}. \quad (\text{A.3})$$

Note that vortex loops of all sizes occur.

Suppose we wanted to find the size of a typical vortex loop. One way to do this is to integrate Eq. A.3 from this typical size, which I'll call $r_{thermal}$, to infinity,

and require that the fraction of loops F with $r > r_{thermal}$ be equal to $1/2$,

$$F = \frac{\int_{r_{thermal}}^{\infty} e^{-\frac{2\pi\varepsilon(r)}{k_B T} r} dr}{\int_{\xi}^{\infty} e^{-\frac{2\pi\varepsilon(r)}{k_B T} r} dr} \equiv \frac{1}{2}. \quad (\text{A.4})$$

In Eq. A.4, I used the approximation that $\varepsilon(r)$ is independent of r . Eq. A.4 leads to

$$r_{thermal} = \xi + \frac{k_B T}{2\pi\varepsilon} \ln 2. \quad (\text{A.5})$$

If the second term on the right hand side of Eq. A.5 dominates, this gives

$$r_{thermal} = \frac{k_B T}{2\pi\varepsilon} \ln 2 \rightarrow \varepsilon = \frac{k_B T}{2\pi r_{thermal}} \ln 2. \quad (\text{A.6})$$

Eq. A.6 states that, within a factor of $\ln 2$, the total energy of a vortex loop of size $r_{thermal}$ is equal to $k_B T$, which is a plausible result.

To check whether the second term on the right side of Eq. A.5 is the dominant one, combine Eqs. A.2 and A.5. Using $\kappa \equiv \frac{\lambda}{\xi}$, this leads to

$$r_{thermal} = \xi \left[1 + \frac{\xi}{\left(\frac{16\pi^2 k_B T}{\Phi_0^2} \right) 2\pi \ln \kappa} \right] = \xi \left[1 + \frac{\xi}{\Lambda_T} \frac{\kappa^2 \ln 2}{2\pi \ln \kappa} \right] \quad (\text{A.7})$$

where Λ_T is defined in Eq. (1.1) of Fisher, Fisher, and Huse [12]. The second terms in Eqs. A.5 and A.7 dominate in the critical regime because ξ diverges while Λ_T is fixed. (It's nice to see Λ_T come up naturally in an expression, by the way.) For simplicity, I'll drop the $\ln 2$ in Eq. A.5, and use

$$r_{thermal} = \frac{k_B T}{2\pi\varepsilon}. \quad (\text{A.8})$$

Next consider that a current per unit area J is applied to a plane perpendicular to the area of the loop. The total Lorentz force on the loop is

$$F_{ext} = 2\pi r J \Phi_0. \quad (\text{A.9})$$

Taking the minus one times the derivative of Eq. A.1 gives the force that the loop exerts on itself. Summing the forces and finding the point where the force is equal to zero leads to a critical loop size

$$r_{blowout} = \frac{\varepsilon}{\Phi_0 J}, \quad (\text{A.10})$$

where, for simplicity, $\varepsilon(r)$ is again assumed to not depend on r . Note that Eq. A.4 is *not* the equation that we generally use for the current-dependent length scale L_J .

Physically, if a vortex loop has $r > r_{blowout}$, the external current “blow out” the loop to infinite size; this process leads to dissipation. If $r < r_{blowout}$, the vortex loop shrinks and annihilates.

I can interpret Eq. A.5 in a different, but equivalent, way. The presence of a current density J significantly alters the population of vortex loops with $r > r_{blowout}$, and has less effect on the vortex loops with $r < r_{blowout}$. In this sense, *a current J probes the physics length scales of order $r_{blowout}$ and larger*. This is the type of language that is sometimes used to describe L_J . As I’ll show below, it is probably not correct to describe L_J in this manner.

What is the physical significance of comparing the various lengths, $r_{blowout}$ and $r_{thermal}$, Eqs. A.8 and A.10, to each other? If $r_{thermal} \ll r_{blowout}$, the current is probing a length scale where there are very few vortices. The current thus acts as a very small perturbation on the system. If $r_{thermal} \gg r_{blowout}$, the current is probing a very short length scale, and a large portion of the intrinsic vortex population is being disrupted by the current. The point where $r_{thermal} = r_{blowout}$ thus marks a crossover in the behavior from current acting as a small perturbation to current

acting as a large perturbation.

What is the physical significance of comparing the various lengths, $r_{blowout}$ and $r_{thermal}$, Eqs. A.8 and A.10, to the film thickness d ? It is plausible to say $r_{thermal} \ll d$ is the three-dimensional limit, while $r_{thermal} \gg d$ is the two-dimensional limit, since in the second case most of the vortex loops are interrupted by the film thickness, while in the first case they are not. This is true as far as it goes, but it misses the key point that an applied current probes physics at the scale of $r_{blowout}$ and larger, as discussed above. Thus, even in the limit $r_{thermal} \gg d$, if $r_{blowout}$ is small enough, *it will probe physics on length scales smaller than d , and thus the measurement will not be affected by the finite thickness of the film.*

What is required is that the current probes a significant fraction of the loop population and also probes lengths on the scale of the film thickness. For this to be true, it is reasonable to require that

$$r_{blowout} = r_{thermal} \equiv L_J. \quad (\text{A.11})$$

Combining Eqs. A.8 and A.10, and A.11 gives

$$L_J = \left(\frac{k_B T}{2\pi\Phi_0 J} \right)^{\frac{1}{2}}. \quad (\text{A.12})$$

This suggests the following physical description for L_J : For any J there is a length scale L_J , given by Eq. A.12, such that *roughly half the equilibrium (zero current) vortex population is blown out by J , and the other half are not.* This is the length that one should compare to the film thickness for seeing whether or not the measurements are in the two or three dimensional limit. *The requirements are that there be a*

significant fraction of the loops that feel the film thickness, and, in addition, that the current is probing on the same length scale.

A.2 More realistic model for $\varepsilon(r)$

In this section, I'll use the analogy between a vortex loop and wire loop to calculate $\varepsilon(r)$. I'll use SI units because they are easier for this problem, at least for me. I start with an analogy between a long straight wire carrying a current I_1 . This current creates a magnetic field B_1 given by

$$B_1 = \frac{\mu_0 I_1}{2\pi r}. \quad (\text{A.13})$$

A parallel wire carrying a current I_2 feels a force per unit length given by

$$f = B_1 I_2 \quad (\text{A.14})$$

and the energy per unit volume associated with a field B is given by

$$\frac{E}{V} = \frac{B^2}{2\mu_0} \quad (\text{A.15})$$

Next, consider a straight vortex. Outside the core but inside the penetration depth, for $\xi \ll r \ll \lambda$, there is a circumferential velocity given by

$$v_1 = \frac{n_1 \hbar}{2\pi m^* r} \quad (\text{A.16})$$

Where n_1 is an integer, \hbar is Planck's constant, and m^* is the Cooper pair mass. (n_1 is included to make comparisons clearer, the usual case is $n_1 = 1$). If there is a second parallel vortex with vorticity n_2 , the force exerted by the first vortex on the second is given by

$$f = j_1 n_2 \Phi_0 \quad (\text{A.17})$$

Currents	Vortices
μ_0	$\frac{1}{m^*n^*}$
I	hnn^*
B	v

Table A.1: Translation table for the physical quantities between Circuits and Vortices.

Where j_1 is the current/area created by the first vortex, so that $j = n^*q^*v$, where n^* is the Cooper pair density, $q^* = 2e$, and v is the superfluid velocity.

Finally, the energy per unit volume associated with a superfluid velocity is just the kinetic energy,

$$\frac{E}{V} = n^* \frac{1}{2} m^* v^2. \quad (\text{A.18})$$

Eqs. A.13-A.15 are analogous to Eqs. A.16-A.18, and the physics is the same. In both cases, there is a $1/r$ field (B or v) with an energy that is quadratic in the field. You can use the analogy to map well-understood problems involving currents and inductances onto problems involving vortices. To do this, we need a translation table. I used the following one: By substituting quantities in the first column of table. A.1 into results from circuit theory, you get analogous results for vortices. For example, substituting the appropriate second-column quantities into Eq. A.13 leads to Eq. A.16.

This is particularly valuable to calculate energies of systems. This is done

using the inductive energy formula

$$E = \frac{1}{2}LI^2 \quad (\text{A.19})$$

Ramo, Whinnery, and Van Duzer's book *Fields and Waves in Communication Electronics*, second edition, p. 190, gives the formula for the inductance of a wire loop.

The wire has a radius a , and is bent into a loop of radius r , r is the distance from the center of the loop to the center of the wire. The formula is

$$L = \mu_0(2r - a) \left[\left(1 - \frac{k^2}{2}\right)K(k) - E(k) \right] \quad (\text{A.20})$$

Where $E(k)$ and $K(k)$ are complete elliptic integrals of the first and second kind,

$$E(k) = \int_0^{\pi/2} \sqrt{1 - k^2 \sin^2 \phi} d\phi, \quad (\text{A.21})$$

$$K(k) = \int_0^{\pi/2} \frac{1}{\sqrt{1 - k^2 \sin^2 \phi}} d\phi \quad (\text{A.22})$$

and

$$k^2 = \frac{4r(r - a)}{(2r - a)^2}. \quad (\text{A.23})$$

Using the translation table, Eqs. A.19, as well as Eqs. A.20-A.24, we can get the energy of a vortex loop of radius r and thus the energy per unit length $\varepsilon(r)$. Note that the analogy requires that the superfluid velocity varies as $1/r$, so that $\xi \ll r \ll \lambda$.

As an example, I'll look at Eq. A.21 in the limit $a \ll r$, ie, the loop is much larger than the coherence length. In this limit (see Abraomwitz and Stegun, *Handbook of Mathematical Functions*, published by NIST)

$$E(k) \approx 1 \quad K(k) \approx \ln \frac{4}{\sqrt{1 - k^2}} \quad (\text{A.24})$$

which leads to

$$L = \mu_0 r \left[\ln \left(\frac{8r}{a} - 2 \right) \right] \quad (\text{A.25})$$

Using Eqs. A.19 and A.20, and replacing a by ξ this leads to an energy per unit length of a vortex loop with radius r of

$$\varepsilon = \pi \frac{\hbar^2}{m^*} n^* \left[\ln \frac{r}{\xi} + \ln(8) - 2 \right] \approx \pi \frac{\hbar^2}{m^*} n^* \left[\ln \frac{r}{\xi} \right] \quad (\text{A.26})$$

It is interesting to note that the last form matches Eq. A.2 at $r = \lambda$, even though it was derived assuming that $r \ll \lambda$. Thus, it is probably a good approximation to use

$$\varepsilon(r) \approx \left(\frac{\Phi_0}{4\pi\lambda} \right)^2 \left[\ln \frac{r}{\xi} \right] \quad \text{for } \xi \ll r \leq \lambda \qquad \varepsilon(r) \approx \left(\frac{\Phi_0}{4\pi\lambda} \right)^2 \left[\ln \frac{\xi}{r} \right] \quad \text{for } r \geq \lambda. \quad (\text{A.27})$$

Chapter B

Literature Review

Table B.1 is a review of experimental and theoretical results for the critical exponents in zero field; Table B.2 is a review of experimental and theoretical results for the critical exponents in non-zero field.

	ν	z	Reference
Theoretical predictions:	$\nu \approx 0.669$ (3D-XY)	$z = 2.0$	[12]
		$z = 1.5$	[38]
Numerical simulations:	$\nu \approx 0.66$	$z = 1.5$	[39]
		$z=2.0$	[78]
	$\nu \approx 1.33$		[79]
Specific heat:			
YBCO crystal (twinned)	Gaussian fluctuation		[36, 37]
	$\nu \approx 0.67$		[32, 33]
DC transport:			
YBCO crystal (Au doped)	$\nu \approx 0.67$	$z \approx 2$	[42]
YBCO crystal (twinned)	$\nu \approx 0.67$	$z \approx 3$	[43]
YBCO thin film	$\nu \approx 1.2$	$z \approx 2$	[17]
	$\nu \approx 1.1$	$z \approx 8.3$	[52]
	$\nu \approx 0.63$ (low fields)	$z \approx 1.25$	[46]
AC conductivity:			
YBCO thin film	$\nu \approx 1.2$	$z = 2.3 - 3.0$	[44]
BSCCO thin film		$z \approx 2.0$	[80]
LSCO thin film	$\nu \approx 0.67$	$z \approx 2.0$	[81]

Table B.1: Zero-field critical exponents from theoretical predictions, numerical simulations and experimental results.

	ν	z	Reference
Theoretical predictions:	$\nu > 1$	$z = 4.0 - 7.0$	[12]
		$z = 1.5$	[38]
Numerical simulations:	$\nu \approx 0.7$	$z = 1.5$	[82]
	$\nu \approx 1.3$		[41]
DC transport:			
YBCO crystal (Au doped)	$\nu \approx 0.67$	$z \approx 2$	[42]
YBCO crystal (twinned)	$\nu \approx 0.67$	$z \approx 3$	[43]
	$\nu \approx 2$	$z \approx 4.3$	[64]
YBCO crystal (irradiated)	$\nu(z - 1) \approx 5.3$		[65]
YBCO thin film	$\nu \approx 1.8$	$z \approx 4.8$	[62]
	$\nu \approx 1.4$	$z \approx 4.3$	[48]
	$\nu \approx 1.0 - 1.9$	$z \approx 3.8 - 7$	[83]
	$\nu \approx 1.9$	$z \approx 4.0$	[45]
AC conductivity:			
YBCO crystal (twinned)	$\nu \approx 0.67$	$z = 2.8 - 3.4$	[84]

Table B.2: Vortex-glass critical exponents from theoretical predictions, numerical simulations and experimental results.

Bibliography

- [1] J. G. Bednorz and K. A. Müller, *Zeit. Phys. B* **64**, 189 (1996)
- [2] H. Kamerlingh Onnes, *Leiden Comm.* **120b**, **122b**, **124c**(1911)
- [3] Linda E. Reichl, “*A Modern Course in Statistical Physics*” (J. Wiley and Sons, New York 2nd ed. 1998)
- [4] H. Eugene Stanley, “*Introduction to phase transitions and critical phenomena*” (Oxford University Press, New York, 1971)
- [5] F. and H. London, *Proc. Roy. Soc.(London)* **A149**, 71 (1935)
- [6] Michael Tinkham, “*Introduction to Superconductivity*”, 2nd ed. (McGraw-Hill, New York, 1996)
- [7] J. Bardeen, L. N. Cooper, and J. R. Schrieffer, *Phys. Rev.* **108**, 1175 (1957)
- [8] V. L. Ginzburg and L. D. Landau, *Zh. Eksperim. i Teor. Fiz.* **20**, 1064 (1950)
- [9] A. A. Abrikosov, *Sov. Physics.-JETP* **5**, 1174 (1957)
- [10] J. Bardeen and J. J. Stephen, *Phys. Rev.* **140**, A1197 (1965)
- [11] P. W. Anderson and Y. B. Kim, *Rev. Mod. Phys.* **36**, 39 (1964)
- [12] D. S. Fisher, M. P. A Fisher, and D. A. Huse, *Phys. Rev. B* **43**, 130 (1990)
- [13] M. K. Wu, J. R. Ashburn, C. J. Torng, P. H. Hor, R. L. Meng, L. Gao, Z. J. Huang, Y. Q. Wang, and C. W. Chu, *Phys. Rev. Lett.* **58**, 908 (1987)
- [14] S. K. Ma, “*Modern Theory of Critical Phenomena*”, (Benjamin, Reading MA, 1976)
- [15] V. L. Ginzburg, *Phys. Rev. B* **36**, 3930 (1987)
- [16] C. J. Lobb, *Phys. Rev. B* **36**, 3930-3932 (1987)
- [17] M. C. Sullivan, “*The normal-superconducting phase transition of YBCO in zero magnetic field*” (Ph.D. Dissertation, University of Maryland, 2004)

- [18] D. R. Strachan, “*The superconducting transition of YBCO*” (Ph.D. Dissertation, University of Maryland, 2002)
- [19] P. C. Hohenberg and B. I. Halperin, *Rev. Mod. Phys.* **49**, 435 (1977)
- [20] J. J. Binney, N. J. Dowrick, A. J. Fisher, and M. E. J. Newman, *The Theory of Critical Phenomena: An Introduction to the Renormalization Group* (Oxford University Press, New York, 1995)
- [21] J. C. Leguillou and J. Zinn-Justin, *Phys. Rev. B* **21**, 3976 (1980)
- [22] D. Z. Albert, *Phys. Rev. B* **25**, 4810 (1982)
- [23] M. A. Herman and H. Sitter, “*Molecular Beam Epitaxy: Fundamentals and Current Status*”, (Springer, New York, 1996)
- [24] S. Sivaram, “*Chemical Vapor Deposition: Thermal and Plasma Deposition of Electronic Materials*”, (Van Nostrand Reinhold, New York, 1995)
- [25] R. Parsons, “*Sputter Deposition Processes, Thin Film Processes II*”, edited by J. L. Vossen and W. Kern, (Academic Press, Boston, MA, 1991)
- [26] T. Venkatesan, “*Pulsed Laser Deposition: Future Trends, Pulsed Laser Deposition of Thin Films*”, edited by D. B. Chrisey and G. K. Hubler, (John Wiley and Sons, New York, 1994)
- [27] D. Dijkkamp, T. Venkatesan, *et al.*, *Appl. Phys. Lett.* **51**, 619 (1987)
- [28] J. Nam *et al.*, *Appl. Phys. Lett.* **82**, 3728 (2003)
- [29] K. Segawa and Y. Ando, *Phys. Rev. Lett.* **86**, 4907, (2003)
- [30] K. Segawa and Y. Ando, *Phys. Rev. B*, **69** 104521 (2004)
- [31] M. C. Sullivan *et al.*, *Phys. Rev. B* **72**, 092507 (2005)
- [32] M. B. Salamon, J. Shi, N. Overend, and M. A. Howson, *Phys. Rev. B* **47**, 5520 (1993); M. B. Salamon, W. Lee, K. Ghiron, J. Shi, N. Overend, and M. A. Howson, *Physica A* **200**, 365 (1993)
- [33] N. Overend, M. A. Howson, and I. D. Lawrie, *Phys. Rev. Lett.* **72**, 3238 (1994)
- [34] V. Pasler *et al.*, *Phys. Rev. Lett.* **81**, 1094 (1998)

- [35] O. Jeandupeux, A. Schilling, and H. R. Ott, Phys. Rev. B **53**, 12475 (1996)
- [36] S. E. Inderhees, M. B. Salamon, Nigel Goldenfeld, J. P. Rice, B. G. Pazol, and D. M. Ginsberg, Phys. Rev. Lett. **60**, 1178, (1988)
- [37] M. B. Salamon *et al.*, Phys. Rev. B **38**, 885 (1998)
- [38] Flavio S. Nogueira and Dirk Manske, Phys. Rev. B **72**, 014541 (2005)
- [39] J. Lidmar, M. Wallin, C. Wengel, S. M. Girvin, and A. P. Young, Phys. Rev. B **58**, 2827 (1998)
- [40] H. Weber and H. J. Jensen, Phys. Rev. Lett. **78**, 2620 (1991)
- [41] J. Lidmar, Phys. Rev. Lett. **91**, 097001,(2003)
- [42] N.-C. Yeh et al, Phys. Rev. B. **45**, 5654 (1992)
- [43] N.-C. Yeh et al, Phys. Rev. B. **47**, 6146 (1993)
- [44] J. C. Booth, D. H. Wu, S. B. Qadri, E. F. Skelton, M. S. Osofsky, A. Piqu, and S. M. Anlage, Phys. Rev. Lett. **77**, 4438 (1996)
- [45] Katerina Moloni, Mark Friesen, Shi Li, Victor Souw, P. Metcalf, and M. McElfresh, Phys. Rev. B **56**, 14784 (1997)
- [46] Katerina Moloni, Mark Friesen, Shi Li, Victor Souw, P. Metcalf, Lifang Hou and M. McElfresh, Phys. Rev. Lett. **78**, 3173 (1997)
- [47] C. Dekker, R. Koch, B. Oh, and A. Gupta, Physica C **185-189**, 1799 (1991)
- [48] P. J. M. Woltgens, C. Dekker, R. H. Koch, B. W. Hussey, and A. Gupta, Phys. Rev. B **52**, 4536 (1995)
- [49] M. C. Sullivan *et al.*, Phys. Rev. B **70**, 140503 (2004)
- [50] M. C. Sullivan et al. Phys. Rev. B **69**, 2145254 (2004)
- [51] J. M. Repcaci, “*The Superconducting Phase Transition of Thin YBCO Films*” (Ph.D. Dissertation, University of Maryland, 1997)
- [52] J. M. Roberts, Brandon Brown, B. A. Hermann, and J. Tate, Phys. Rev. B **49**, 6890 (1994)

- [53] D. R. Strachan et al., Phys. Rev. Lett. **87**, 067007 (2001)
- [54] H. Kitano *et al.* Phys. Rev. B **73**, 092504 (2006)
- [55] T. T. M. Palstra, B. Batlogg, L. F. Schneemeyer, and J. V. Waszczak, Phys. Rev. Lett. **61**, 1662 (1989)
- [56] E. Zeldov *et al.*, Phys. Rev. Lett. **62**, 3093 (1989)
- [57] A. I. Larkin and Yu. N. Ovchinnikov, J. Low Temp. Phys. **34**, 409 (1979)
- [58] K. Binder and A. P. Young, Rev. Mod. Phys. **58**, 801 (1986)
- [59] T. Olson and A. P. Young, Phys. Rev. B **61**, 12467 (2000)
- [60] Anders Vestergren, Jack Lidmar, and Mats Wallin, Phys. Rev. Lett. **88**, 117004 (2002)
- [61] Jack Lidmar, Phys. Rev. Lett. **91**, 097001, (2003)
- [62] R. H. Koch, V. Foglietti, W. J. Gallagher, G. Koren, A. Gupta, and M. P. A. Fisher, Phys. Rev. Lett. **63**, 1511 (1989)
- [63] Akihito Sawa *et al.*, Phys. Rev. B **58**, 2868 (1998)
- [64] P. L. Gammel, L. F. Schneemeyer, and D. J. Bishop, Phys. Rev. Lett. **66**, 953 (1991)
- [65] A. M. Petrean and L. M. Paulius, Phys. Rev. Lett. **84**, 5852, (2000)
- [66] S. N. Coppersmith, M. Inui, and P. B. Littlewood, Phys. Rev. Lett. **64**, 2585 (1990)
- [67] Jin-Tae Kim, Nigel Goldenfeld, J. Giapintzakis, and D. M. Ginsberg, Phys. Rev. B **56**, 118 (1997)
- [68] K. Yamafuji and T. Kiss, Physica C **258**, 197 (1996)
- [69] B. Brown, Phys. Rev. B **61**, 3267 (2000)
- [70] M. Kardar and Y.-C. Zhang, Phys. Rev. Lett. **58**, 2087 (1987)

- [71] H. Safar *et al.*, Phys. Rev. Lett. **69**, 824 (1992)
- [72] H. Safar *et al.*, Phys. Rev. Lett. **70**, 3800 (1992)
- [73] W. K. Kwok *et al.*, Phys. Rev. Lett. **69**, 3370 (1992)
- [74] U. Welp *et al.*, Phys. Rev. Lett. **76**, 4809 (1996)
- [75] A. I. Rykov *et al.*, Phys. Rev. B **60**, 7601 (1999)
- [76] A. Schilling *et al.*, Nature **382**, 791 (1996)
- [77] F. Bouquet *et al.*, Nature **411**, 448 (2001)
- [78] V. Aji and N. Goldenfeld, Phys. Rev. Lett. **87**, 197003 (2001)
- [79] R. Seto, R. Botet, and H. Kuratsuji, Phys. Rev. B **73**, 012508 (2006)
- [80] K. D. Osborn *et al.*, Phys. Rev. B **68**, 144516 (2003)
- [81] H. Kitano *et al.*, Phys. Rev. B **73**, 092504 (2006)
- [82] Anders Vestergren *et al.*, Phys. Rev. Lett. **88**, 117004, (2002)
- [83] Z. Sefrioui *et al.*, Phys. Rev. B **60**, 15423 (1999)
- [84] D. S. Reed *et al.*, Phys. Rev. B **47**, 6150 (1993)